EXPERIMENTS WITH STARK-DECELERATED AND TRAPPED MOLECULES

JOOP JELTE GILIJAMSE

Experiments with Stark-decelerated and trapped molecules

Proefschrift

Contents

Chapter 1

Introduction

1.1   Control over molecular beams

The use of inhomogeneous electric and magnetic fields to influence the trajectories of atoms and molecules in free flight has played an important role in the development of the field of atomic and molecular beams and has contributed enormously to its success [1]. In the famous deflection experiment from 1922, Stern and Gerlach manipulated the trajectories of silver atoms to demonstrate space quantization [2]. Later, hexapole field geometries were used to state-selectively focus atoms and molecules [3, 4, 5]. The packets of molecules created in such experiments, where control is gained over internal and external degrees of freedom of molecular beams, are an ideal starting point for further studies on molecular properties and have led to many fascinating discoveries. A prime example are crossed-beam molecular collision studies [6, 7]. Parameters like the velocity, orientation and state distribution of the molecules before and after the collision can reveal a lot of information about their internal structure and mutual interactions.

The manipulation of beams of molecules with external magnetic and electric fields as used in the past almost exclusively involved the transverse motion of the molecules. The reason for this is obvious: the field gradients that can be realized in the laboratory are sufficient to influence the transverse velocity components of the molecules in the beam, as these are centered around zero velocity. However, the forward velocity of molecules in conventional beams is centered around a large value. Therefore, to be able to significantly influence the longitudinal motion of the molecules, non-static fields are needed. In the *Stark deceleration* technique, the fast switching of strong electric fields is used to reduce the kinetic energy of the molecules. This method combines molecular beam technology with concepts from charged particle accelerator physics. In essence, a part of a molecular beam pulse of polar neutral molecules can be

accelerated or decelerated to a range of velocities, exploiting the interaction of polar molecules with inhomogeneous electric fields. The Stark deceleration technique allows for two types of experiments. The first is a class of experiments where the velocity (distribution) of the molecular beam is an important parameter and information on the properties of cold molecules can be revealed by slowing them down. For the second type of experiments, packets of molecules are decelerated all the way to standstill and confined in a trap, enabling studies that require a long observation time and low translational temperatures.

Examples of the first class of experiments are high-resolution spectroscopy and crossed-beam collision studies. The collision energy is one of the most important parameters in a collision event, its value determines the outcome and often even the nature of the collision itself [8]. For instance, it has been observed that if the available collision energy matches a certain transition in a molecule, resonances in the collisional cross-section can occur [9]. The implementation of a Stark decelerator allows one to vary the energy available for the collision [10, 11]. In chapter 4, the first collision experiment with a Stark decelerated beam is presented. It is shown that the collision energy can be tuned over several rotational thresholds in the OH radical, and the possible future applications of this technique for collision studies are discussed.

The resolution achievable in any spectroscopic experiment is limited by the interaction time of the atom or molecule under investigation with the laser field. Slow molecules are therefore also advantageous for high-resolution spectroscopy. By measuring the inversion tunnelling spectrum of $^{15}ND_3$ using a Stark-decelerated molecular beam it was shown in reference [12] that the resolution of a spectroscopic experiment can be improved using samples of slow molecules. In reference [13] the same principles were exploited to perform precision measurements on Λ-doublet microwave transitions in OH. If slow molecules are directed upwards, their longitudinal velocity is affected by gravity and a molecular fountain can be created. As molecules can be made to pass the detection point twice, the interrogation time in this type of experiment can be on the order of a second, allowing precise spectroscopic measurements. Such high-resolution measurements on molecules can be of importance for studies on fundamental physical quantities as, for instance, the ratio of the proton mass to the electron mass [14]. Furthermore a search for a permanent electric dipole moment of the electron, which would result in the violation of time reversal symmetry, is being done using polar molecules [15] because an external electric field applied to a polar molecule leads to a hugely magnified internal field.

Cold molecules in traps

If the packet of molecules is slowed down to a near standstill, the molecules can be loaded and confined in various types of traps. The ability to confine cold gas-phase (polar) molecules in traps has increased interest in gas-phase molecular physics in recent years. This interest stems from the exotic and

intriguing phenomena that are predicted for these molecular gases at ultralow temperatures, where the probability of chemical reactions and collisional energy transfer can be very large [16]. The first experiment where large samples of cold molecules were trapped was performed in a magnetic trap loaded with buffer-gas-cooled CaH molecules in 1998 [17]. Later, molecules that are colder by several orders of magnitude were created in experiments where ultracold atoms are combined via photo-association or Feshbach-association to form ultracold molecules [18, 19].

The density of the molecular packets that are produced via the Stark-deceleration technique has already proven to be sufficient for the above-mentioned spectroscopy and collision studies. However, it is still a formidable challenge to reach high enough densities in the trap for collisions to occur between the trapped molecules on the trapping time scale. This is a requirement for the experimental study of the interactions between the trapped molecules. Therefore, effort in the research on cold molecules is currently aimed at increasing the phase-space density of the trapped molecules [20]. A natural approach to try to reach this goal is to adapt cooling techniques used for atoms such as evaporative cooling [21] and sympathetic cooling [22], but they usually require trapping times of 10 s or more. Therefore, an investigation of the density currently available in the trap (presented in section 2.5) and the limiting factors for the trapping time of polar molecules is of importance. Also, for future studies of collisions between trapped molecules a quantitative knowledge of the available densities and an understanding of all trap loss mechanisms are essential. A detailed study of the trap loss mechanisms for electrostatically trapped OH and OD molecules is presented in chapter 5.

In the rapidly growing research field of cold molecules, polar molecules are of special interest. Samples of polar molecules are predicted to be much different from atomic Bose-Einstein condensates or degenerate Fermi gases due to the dipole-dipole interaction [23, 24]. Furthermore, these samples of ultracold gases allow for the engineering of macroscopic collective quantum states [25]. Trapped polar molecules also hold promise for use in quantum information systems [26]. Recently, the first ultracold dense gas of ground state polar molecules was created. Starting from a near quantum degenerate gas mixture of ^{40}K atoms and ^{87}Rb atoms, that is nowadays routinely produced in optical dipole traps by means of laser cooling [27] and evaporative cooling [21], polar ^{40}K^{87}Rb molecules were created using magnetic Feshbach resonances [28]. The thus created Feshbach molecules were transferred to the rovibrational ground state using a single-step STIRAP (Stimulated Raman Adiabatic Passage) process [29].

Long observation times

Since trapped packets of molecules are not only cold, but can be confined for times up to seconds as well, long observation times can be achieved and pro-

cesses that take place at long timescales, like spontaneous decay of electronically or vibrationally excited states, can be accurately studied. When all trap loss processes take place at timescales on the order of seconds, excited states with lifetimes in the millisecond range can often be measured without taking into account any correction factor and thus yield accurate values for the studied lifetimes. In the past, such lifetimes were often measured in molecular beams and, although ingenious schemes have been developed to measure the lifetime of several excited states [30, 31, 32], the accuracy of such a measurement is limited by the relatively short interaction time in a molecular beam. The long interaction time that can be achieved in traps has been exploited to study the radiative lifetime of the vibrationally excited states of OH ($X^2\Pi_{3/2}, v = 1, J = 3/2$) [33] and NH ($X^3\Sigma^-, v = 1, N = 0$) [34] radicals. The level of detail that is reached in this type of experiments challenges existing theory, as is shown in chapter 6 for the electronically excited metastable $a^3\Pi_{1,2}, v = 0$ state of CO.

1.2 Slowing and trapping molecules

Stark deceleration and electrostatic trapping

The history of the Stark decelerator goes back to the 1960s. In 1967 King and Golub proposed a design for a decelerator for the ammonia molecule [35], while Wharton and Bromberg presented a similar design for an accelerator for LiH molecules [36]. Due to the technical challenges associated with the design, the successful implementation of this idea was only realized 32 years later by Bethlem, Berden, and Meijer. Using a differently designed Stark decelerator, conisting of an array of 63 crossed electrode pairs, they achieved the deceleration of metastable CO ($a^3\Pi_{1,2}, v = 0$) molecules from 225 m/s to 98 m/s [37]. Since then, many more Stark decelerators have been built and several molecules were successfully decelerated. In the order of appearance in the literature these were ND_3 in 2000 [38], OH in 2003 [39], formaldehyde (H_2CO) [40], SO_2 [41], and metastable NH ($a^1\Delta$) [42] in 2006, and OD in 2007 [43]. In the reviews about Stark deceleration [44, 45] and about the manipulation of molecular beams in general [46] more details on the history of molecular beam deceleration can be found.

Once molecules are slowed down and only possess a fraction of their initial kinetic energy, they can be captured in various types of electrostatic or magnetic traps. The combination of a Stark decelerator and an electrostatic trap works for a large class of polar molecules, and has resulted in the trapping of ND_3 molecules [38] in 2000 and OH radicals [47] in 2005. A combination of electric and magnetic fields has been used to study OH molecules in a magnetoelectrostatic trap [48]. The confinement in a magnetic trap, leaving large adjustable electric fields for control, gives the possibility to polarize the molecules and, in principle, to study the effect of the orientation of the molecules on their

interactions. In this thesis, the first electrostatic trapping of ground state OD, metastable NH and metastable CO is presented (see chapter 2, figure 2.12).

Other slowing and trapping methods

The Stark deceleration technique is an excellent tool for slowing molecules in low-field-seeking states. However, many molecular states are actually high-field seeking. In general, the absolute ground state of any molecule is high-field seeking. For molecules in such a quantum state the Stark deceleration principle discussed so far still applies if the alternating-gradient (AG) focusing principle is employed. The AG principle is based on alternating focusing and defocusing in the two transversal directions. Deceleration according to this principle is shown in references [49, 50], and has been implemented for metastable CO [51], YbF [50], and benzonitrile (C_7H_5N) [52] molecules. The AG principle can also be applied to confine high-field seeking molecules in an AC electric trap [53].

The miniaturization of the usually around a meter long Stark decelerator by scaling the electrodes down to nanowires on a chip has been proposed and shown in references [54] and [55]. In reference [55] it is experimentally demonstrated that metastable CO molecules can be captured in travelling potential wells and that their velocity can be manipulated in this way.

Beside Stark deceleration and its variations, other methods exist that are suited to decelerate and eventually trap molecules. One of them is Zeeman deceleration, a technique where the Zeeman interaction with inhomogeneous magnetic fields is used to slow the molecules analogously to the Stark interaction for electric fields. This technique has the advantage that it can be applied to a large class of molecules that can not be slowed with a Stark decelerator due to the lack of a strong electric dipole moment. Zeeman deceleration of hydrogen atoms [56, 57], metastable Ne [58], and oxygen molecules [59] has been demonstrated up to date. In a recent paper magnetic trapping of H atoms after Zeeman deceleration has also been shown experimentally [60].

Even more general is a deceleration technique where molecules are decelerated via electric dipole interaction in a Rydberg state. Since every molecule possesses such states and Rydberg states generally have a large dipole moment, molecules can in principle be decelerated using only a few electric field stages, operated at relatively small electric field strengths. Successful reduction of kinetic energy via this technique has been shown for instance for H_2 molecules [61]. A disadvantage of using Rydberg states is the short lifetime of such states (typically in the micro- to millisecond range), which limits the time available for further experiments with the decelerated and eventually trapped [62] molecules.

Another method to slow molecules with a decelerating force is the so-called optical Stark deceleration [63]. A controlled manipulation of molecules is possible using deep periodic optical lattice potentials created by intense optical fields (10^{11} Wcm^{-2}). Using these potentials, rapid deceleration or acceleration

in a molecular beam to well-defined velocities was demonstrated for NO [64] and benzene (C_6H_6) [65].

Mechanical means to produce beams of slow molecules have also been demonstrated, e.g. the back-spinning nozzle [66]. Closely related to this are methods that utilize reactive [67] or rotationally inelastic [68] collisions in counter-propagating or crossed beams to produce slow molecules.

Instead of slowing molecules with a direct deceleration force, it has been shown that slow polar molecules can be produced by velocity selection from a thermal distribution in a room-temperature reservoir. This conceptually simple idea appears appealing, since only a linear electrostatic quadrupole with a curved section is needed to guide the molecules into an ultrahigh vacuum chamber [69]. A disadvantage of this technique is its poor quantum-selectivity, since molecules in many low-field-seeking levels will follow the curve of the quadrupole field. A way to circumvent this problem is to combine the quadrupole guide with a cryogenic cell where their external and internal degrees of freedom are cooled by collisions with a helium buffer gas [70].

1.3   This thesis

This thesis describes a variety of experiments that exploit the possibilities of Stark decelerated packets of molecules. A detailed description of the operation principles and experimental setup of the Stark decelerator and electrostatic trap is presented in chapter 2, including the implementation of an evolutionary algorithm to verify and optimize the sequence of timings that is involved in a Stark deceleration and trapping experiment. In chapters 3 to 6 contributions to the two types of experiments as discussed in the first introductional section are presented. The possibility to create packets of molecules with a tunable velocity enabled the first crossed-beam scattering experiment using a Stark decelerator. This experiment is presented in chapter 4. In the second type of experiments molecules are decelerated to a standstill and confined in a trap enabling the study of new, unexplored physical properties of the molecules. In the research presented in this thesis, three species (OD, NH and CO) were trapped for the first time in an electrostatic trap. The trapping of these molecules is described in chapter 2. Chapters 5 and 6 give examples of experiments with trapped cold molecules where the long observation time allowed by the trapping is essential. In chapter 5 the interaction of blackbody radiation with trapped polar molecules is investigated experimentally and theoretically. Furthermore, knowledge is gathered about the various loss processes that play a role once molecules are trapped in a single quantum state at low temperatures. In chapter 6 the long observation time of trapped metastable CO is exploited to measure the radiative lifetime of two electronically excited rotational states.

To produce molecular packets that are even colder, further cooling schemes have been proposed for OH molecules [71, 72] and NH molecules [73]. How-

ever, the implementation of cooling schemes like evaporative cooling requires a higher number density. An important step toward higher densities in the trap is the suppression of loss processes due to the spreading out of slow packets of molecules during the trap loading process. In chapter 7 criteria for the optimal loading of molecules in traps in order to get an as high as possible phase-space density are defined. In addition, several trap designs are presented that allow for a more efficient trap loading. Another obvious route towards higher densities in the trap is the accumulation of several packets of molecules that are produced in distinct cycles of the experiment [74]. The implementation of this scheme requires a combination of Stark deceleration and magnetic trapping. A magnetic trap for metastable NH molecules, where a magnetic field gradient of 600 Gauss/cm is created by sending $\sim$1000 A through copper coils, is discussed in chapter 7. The relatively large effort required to create strong trapping potentials using large currents can be circumvented by the implementation of strong permanent magnets. Cheap rare-earth magnets that can possess a remanence higher than 1 T are commercially available, allowing for the construction of compact, deep magnetic traps [75]. A design for such a trap including three-dimensional trajectory calculations is presented in chapter 7 as well. The interaction of Stark-decelerated OH molecules with these permanent magnets has been studied in the proof-of-principle experiment presented in chapter 3, in which mirrors constructed from permanent magnets were used to reflect OH molecules.

Chapter 2

Deceleration and trapping of polar molecules

In this chapter, a general overview is given over the interaction of molecules with electric and magnetic fields. The experimental setup and general procedures that are used are described and the electrostatic trapping of the molecules OH, OD, CO and NH is presented. Different methods that are implemented to characterize the trapped packets of molecules are discussed.

2.1 The interaction of molecules with electric and magnetic fields

The trapping experiments described in this thesis are performed with several types of traps. The molecules OH, OD, CO and NH were trapped in a new type of electrostatic trap, developed to improve the loading of packets of slowed molecules into the trap. The general principles of Stark deceleration and electrostatic trapping of polar molecules are discussed in this chapter; a full detailed description of the trapping procedure can be found later in chapter 7. The NH molecule was also trapped in a magnetic trap in both the ground state and the electronically excited metastable state. For the description of these various trapping experiments and Stark deceleration, the understanding of interactions of molecules with inhomogeneous electric and magnetic fields plays a crucial role. The molecules studied, were ground state OH and OD ($X\,^2\Pi_{3/2}, v = 0, J = 3/2$), metastable CO ($a\,^3\Pi_{1,2}, v = 0, J = 1, 2$) and metastable NH ($a\,^1\Delta, v = 0, J = 2$). They are all polar - they have an asymmetric internal charge distribution - and interact via their dipole moment with electric fields in analogy with the classical dipole interaction $W = -\vec{\mu}\cdot\vec{E}$. Given a inhomogeneous electric field, this interaction results in a force $\vec{F} = -\vec{\nabla}W$ in the direction of high or low electric field, depending on the quantum state of the molecule. The following section briefly describes the molecular Stark effect as it occurs in those molecules. In addition the Zeeman effect in the OH and NH molecule is discussed, that allows for the magnetic reflection and trapping experiments as presented in the chapters 3 and 7, respectively.

2.1.1 Stark effect of OH, CO and NH

The interaction of polar molecules with externally applied electric fields gives rise to an extra term in their Hamiltonian. In addition to the electronic, vibrational and rotational part, this adds a Stark term $\hat{H}_{\mathrm{Stark}} = -\vec{\mu} \cdot \vec{E}$, where $\vec{\mu}$ is the body-fixed electric dipole moment of the molecule and $\vec{E}$ is the electric field vector. The full Hamiltonian then reads

$$\hat{H} = \hat{H}_{el} + \hat{H}_{vib} + \hat{H}_{rot} + \hat{H}_{Stark} \ . \tag{2.1}$$

An extensive description of all parts of this Hamiltonian and the Stark effect can be read in text books [76] or in other sources [77, 78]. For diatomic molecules the dipole moment points along the molecular axis and the Stark interaction can be expressed as

$$\hat{H}_{\mathrm{Stark}} = -|\vec{E}|\mu \cos(\Theta) \ , \tag{2.2}$$

where Θ is the angle between the external electric field vector and the molecular axis. To solve the Schrödinger equation using this Hamiltonian for a specific state, one has to evaluate the eigenvalues of the energy matrix that are

calculated using rotational wavefunctions that take fine structure effects like Λ-doubling into account. For the ground state of OH ($X^2\Pi_{3/2}, v = 0, J = 3/2$) and electric fields up to around 200 kV/cm, the coupling between rotational states with $\Delta J \neq 0$ can be neglected, and the electric field dependance of the energy levels can be expressed as

$$W_{Stark}(|E|) = \frac{E_\Lambda}{2} \pm \sqrt{\left(\frac{E_\Lambda}{2}\right)^2 + Q^2} \ , \qquad (2.3)$$

where Q is given by

$$Q = -\mu|E|\frac{M_J\Omega_{eff}}{J(J+1)} \ . \qquad (2.4)$$

In equations 2.3 and 2.4, E_Λ is the zero-field Λ-doubling energy splitting, and Ω_{eff} is the effective value of Ω, representing the projection of J on the molecular axis. For OH in the $^2\Pi_{3/2}, J = 3/2$ rotational ground state Ω_{eff} has a value of 1.46 [78]. The plus and the minus in the expression give the Stark shift for the low-field-seeking (lfs) and high-field-seeking (hfs) components, respectively. Two cases can be distinguished. For high electric field strengths, the condition $Q/E_\Lambda >> 1$ is fulfilled, expression 2.3 simplifies to $W_{Stark} = E_\Lambda/2 \pm Q$, and the Stark effect becomes linear in electric field strength. In much lower fields, for $Q/E_\Lambda << 1$, the Stark effect is quadratic in electric field strength. The Stark effect of OH is plotted in figure 2.1.
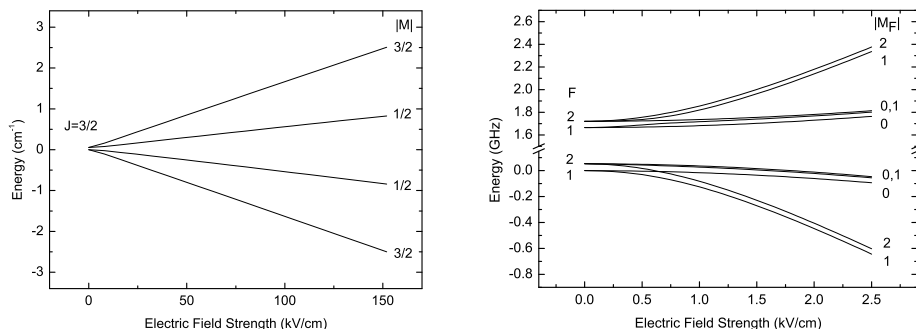
Figure 2.1: The Stark shift of the $^2\Pi_{3/2}, J = 3/2$ state of OH as a function of electric field strength, shown on different scales without (left panel) and with (right panel) taking the hyperfine structure into account.

The left side of figure 2.1 shows the splitting of the rotational ground state $J = 3/2$ of OH into the four different $|M_J|$-components, that represent the different projections of the total angular momentum J onto the electric field

axis. If in addition the hyperfine structure of the molecule is taken into account, the nuclear spin (I_H of the H atom) and the rotational angular momentum (J) couple to yield the quantum number F ($\vec{F} = \vec{J} + \vec{I}$) and its projection M_F (M_F=F, F-1, ..., F). Therefore, the different M_J-levels in figure 2.1 (left) split in multiple M_F components, depicted in the right side of figure 2.1.

The description of the Stark effect of NH in the metastable $a^1\Delta$-state can be simplified to a pure linear case, as E_Λ is only 115 kHz and can be neglected. Formula 2.3 therefore simplifies to

$$W_{Stark} = \pm\, Q = \pm\mu|E|\frac{M_J\Omega_{eff}}{J(J+1)} \quad . \tag{2.5}$$

For NH in the $a^1\Delta$-state $\Omega_{eff} = 2$ and $\mu = 1.49$ D. The Stark effect of the $J = 2$ rotational ground state is shown in figure 2.2. The right side of that figure depicts the Stark effect of the state when hyperfine structure is taken into account. In this case F is the sum of the rotational angular momentum and the spin of both the nitrogen atom ($I_N = 1$) and the spin of the hydrogen atom ($I_H = 1/2$). Therefore F can have all half-integer values ranging from 1/2 to 7/2. As the Λ-doubling is considerably smaller than the hyperfine splitting for NH ($a^1\Delta$), many hyperfine components cross in an electric field, as is seen in figure 2.2.
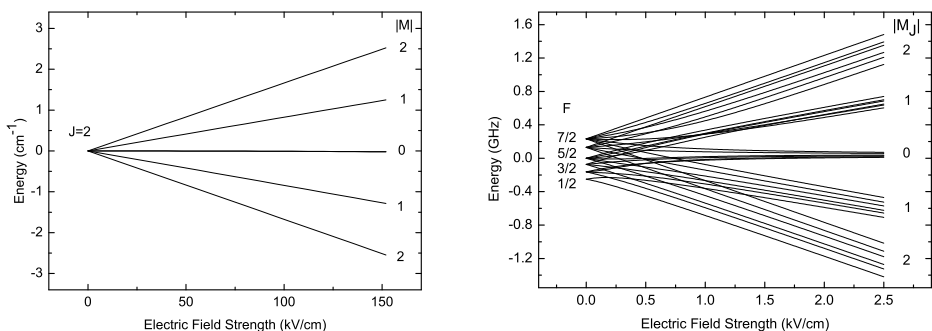
Figure 2.2: The Stark shift of NH in the $a^1\Delta$-state, shown on different scales without (left panel) and with (right panel) taking the hyperfine structure into account.

The $X^1\Sigma^+$ ground state of CO lacks a significant Stark effect and molecules in this state are therefore not suited for Stark deceleration experiments. In the electronically excited metastable $a^3\Pi_{\Omega=1}$ or $a^3\Pi_{\Omega=2}$ states, CO molecules experience a significant Stark effect and CO molecules in these states are excellent candidates for deceleration and trapping experiments [37]. The rotational constant of these states is considerably smaller than that of OH and metastable

NH, and equation 2.3 breaks down already for relatively small fields. In order to calculate the Stark shift, one has to diagonalize the Stark-matrix including couplings between rotational states with $\Delta J \neq 0$. This is done for instance in reference [79], and the resulting Stark shift is plotted in figure 2.3.
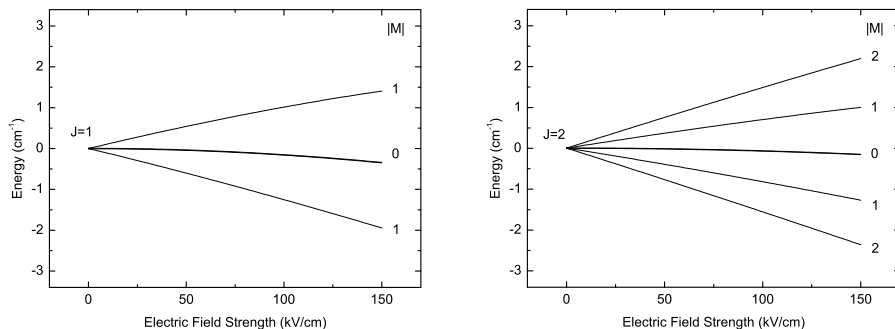
Figure 2.3: The Stark shift of metastable CO in the $a^3\Pi_1$ state (left panel) and in the $a^3\Pi_2$ state (right panel).

2.1.2 Zeeman effect in NH and OH

Analogous to the Stark effect for interaction of molecules with electric fields, the Zeeman effect describes the interaction of molecules with magnetic fields. In general the Zeeman term in the Hamiltonian reads $\hat{H}_{\text{Zeeman}} = -\vec{\mu} \cdot \vec{B}$, given a magnetic moment vector $\vec{\mu}$. The magnetic moment in a molecule consists of a magnetic moment associated with the spin $(\vec{S})$ and the orbital angular momentum $(\vec{L})$ of the electrons, leading to

$$\hat{H}_{\text{Zeeman}} = \mu_B(\vec{L} + g_S\vec{S}) \cdot \vec{B}, \qquad (2.6)$$

where μ_B is the Bohr magneton, and the gyromagnetic constant g_S has a value of approximately 2. For the calculation of the Zeeman effect the projections of $\vec{L}$ and $\vec{S}$ on the internuclear axis, Λ and Σ, are of relevance. As for the Stark effect, the strength of the interaction for a specific state can be determined by evaluating the eigenvalues of the energy matrix that is calculated using rotational wavefunctions. The symmetry of the Zeeman operator, however, enables a rotational wavefunction to couple with itself and give rise to a Zeeman splitting.

For ground state NH ($X\,^3\Sigma^-$,v=0,N=0,J=1), $S = 1$ and Λ=0, and the Zeeman splitting has a strength of $2M\mu_BB$, as is shown in figure 2.4 (top). Metastable NH in the $a^1\Delta$,v=0,J=2 state possesses no net spin ($S = 0$) and

15
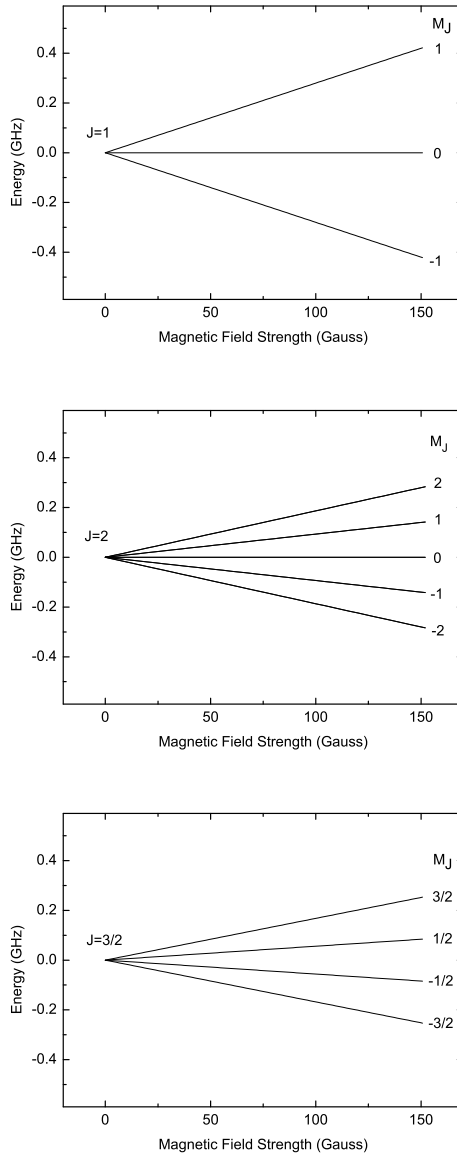
Figure 2.4: The Zeeman splitting in the ground rotational level of NH ($X\,^3\Sigma^-$)(top panel), metastable NH ($a^1\Delta$)(middle panel), and ground state OH ($^2\Pi_{3/2}$)(lower panel) shown on identical scales.

has a Λ of 2. For this Hund's case (a) state, however, orientational effects of the rotational wavefunction in first order lead to the introduction of an effective magnetic moment μ_{eff}:

$$W_{Zeeman} = \mu_{eff}B = \mu_B(\Lambda + g_S\Sigma)\frac{M\Omega_{eff}}{J(J+1)}B. \qquad (2.7)$$

From this equation it follows that NH in the a$^1\Delta$ state has a somewhat weaker Zeeman splitting of $2/3M\mu_BB$, as depicted in figure 2.4. The strength of the Zeeman splitting of the $^2\Pi_{3/2}, J = 3/2$ state of OH is given by this equation as well. In figure 2.4 it is shown that the strength of the Zeeman splitting in OH in this state is $4/5M\mu_BB$.

2.2 Molecular beams

The success of a Stark deceleration experiment strongly depends on the initial conditions of the molecular packet that is sent into the decelerator. Important parameters are the distribution over the quantum states in the molecule, the initial velocity, and the velocity spread. The influence of these parameters on the efficiency of the decelerator is discussed in section 2.3, the present section describes the production of such an internally cold packet of molecules.

A cold beam of molecules can be produced by expanding a gas of the molecules of interest from a container with a relatively high pressure (1-3 bar) through a nozzle into a vacuum alongside a carrier gas of usually rare-gas atoms [1, 80]. Near the nozzle opening, gas particles experience many collisions with other particles coming from the gas container and feel a net force towards a region with lower pressure, into the vacuum. In this process, the original thermal velocity and velocity distribution change drastically. Due to the many collisions, the particles speed up to several hundreds of meters per second, depending on the mass of the particles. Particles that are faster than the main velocity of the gas pulse, will collide with other particles that fly ahead. This implies that relatively fast molecules slow down and slower molecules are speeded up even more, in other words this leads to a narrowing down of the velocity distribution. Depending on which gases are used and the parameters of the free expansion, the velocity distribution can narrow down to 1 % of the beam velocity. A more typical velocity distribution for pulsed molecular beams, as used for the research presented in this thesis, is ~ 15 %. For molecular beams seeded in Xe this velocity distribution corresponds to a translational temperature of around 1 Kelvin.

If such a supersonic beam of rare gas atoms is seeded with molecules at typically a concentration of a few percent, the collisions within the gas pulse during the expansion lead to a internal rotational and vibrational cooling of the molecules. The originally thermal state distribution is changed and finally ro-

tational temperatures of a few Kelvin, and vibrational temperatures of around 50 Kelvin can be achieved.

2.2.1 Molecular beams of OH, OD, NH (a$^1\Delta$) and CO (a$^3\Pi$)

For all experiments described in this thesis a pulsed solenoid valve (General Valve, series 9) is used. The original valve was modified in our laboratory to be able to adjust the velocity of the beam by cooling the valve body. The cooling of the valve is achieved by a nitrogen flow of which the exact temperature is controlled by a PID (proportional integral derivative) loop consisting of a liquid nitrogen bath and an adjustable heater. This system is used to vary the temperature of the valve body in the range from 200 to 300 K.

Intense beams of OH radicals are produced via photo-dissociation of nitric acid (HNO$_3$), that is co-expanded with a rare-gas (usually Xe, also Ar and Kr have been used) in a ratio of about 1.5:100. This mixture is achieved by flowing the seed gas at a pressure of 2-3 bar through liquid nitric acid ($> 90\%$) at room temperature. The acid has a room-temperature vapor pressure of 48 mbar. At the exit of the valve, on the nozzle plate, a 6 mm long quartz capillary with an inner diameter of 1 mm and outer diameter of 3 mm is mounted. The photo-dissociation with a focussed 193 nm UV laser pulse ($\sim$3 mJ in 5 ns) from an excimer laser (Neweks, PSX-501) partially takes place in the capillary, partially just after the molecules have left the capillary into the vacuum. This is experimentally found to give the optimal balance between recombination of the radicals and an efficient cooling into the lowest quantum state. Using Xe as a seed gas, the mean velocity of the resulting OH beam is around 360 m/s with a velocity spread (FWHM) of 15 %. Because of their different masses, beams seeded in Kr and Ar have higher velocities of 450 and 600 m/s, respectively. Finally, beams are skimmed with a 2 mm diameter skimmer placed 21 mm from the exit of the valve. After the supersonic expansion, most of the OH radicals in the beam reside in the lowest rotational ($J = 3/2$) level in the vibrational and electronic ground state $X\,^2\Pi, v = 0$. A molecular beam of OD radicals (chapter 5) was produced in the same way as the OH beam, and with identical intensity. The deuterated nitric acid used for photodissociation was produced in a temperature-controlled reaction between potassium-nitrate and sulfuric-acid.

Beams of metastable NH molecules are produced by photo-dissociation of about 1 vol % hydrazoic azide (HN$_3$) seeded in Krypton. Gaseous HN$_3$ is prepared by the reaction of sodium azide (NaN$_3$) with an excess of lauric acid under vacuum. The reaction starts at approximately 348 K and proceeds smoothly at 353-363 K. The use of Xenon as a carrier gas is not possible since it is known to efficiently quench the metastable NH molecules [81]. Two alternative photo-dissociation wavelengths were used. In the first, HN$_3$ molecules are photo-dissociated by focusing the 6 mJ output of an ArF excimer laser (193 nm) onto the quartz capillary. The absorption cross-section of HN$_3$ at

this wavelength is large [82] and the dissociation transition is easily saturated with the table-top excimer laser that is available. However, NH radicals are produced both in the $X\,^3\Sigma^-$ ground state and in the metastable $a\,^1\Delta$ electronically excited state; the quantum yield for production of NH ($a\,^1\Delta$) is only 0.4 [83].

In the second photo-dissociation scheme, the 266 nm radiation of a Nd:YAG laser ($\sim$60 mJ per pulse) is used. The quartz capillary was not used, as the Nd:YAG laser would damage the capillary. In this scheme the dissociation channel that produces NH in the $X\,^3\Sigma^-$ ground state is spin-forbidden and NH molecules in the $a\,^1\Delta$ state are produced with a unity quantum yield. The absorption cross-section at this wavelength is about two orders of magnitude lower than at 193 nm [82], reducing the efficiency of the dissociation. With the laser systems that are available in our laboratory, the efficiency of the production method using the 266 nm Nd:YAG laser is found to be a factor 1.5 higher compared to the production method using the excimer laser [84].

Highly intense beams of ground state CO can be produced without the use of a precursor by directly expanding mixtures with CO concentrations up to 20% in Xe from the pulsed valve. For the experiments in chapter 6 the valve was cooled to 203 K, resulting in a mean velocity of 320 m/s. A packet of CO molecules in the upper (low-field seeking) Λ-doublet component of the J=1,Ω=1 or J=2,Ω=2 level in the metastable $a^3\Pi$ state is prepared by direct laser excitation at 206 nm from the $X^1\Sigma^+, v = 0$ ground state. The laser radiation is generated by a narrow-band pulsed laser system. In this laser the output of a frequency stabilized single mode ring dye laser is amplified in a three stage pulsed dye amplifier pumped by a frequency-doubled injection seeded Nd:Yag pump laser. The frequency of this radiation is tripled using optical conversion crystals.

2.3   Deceleration of molecules

2.3.1   The principles of Stark deceleration

The operation principle of a Stark decelerator for molecules in low-fields-seeking states is sketched in figure 2.5. As described in section 2.1.1, molecules in such quantum states experience a force in the direction where the electric field is the lowest and are therefore always forced towards the beam axis. In addition to this transversal force, a longitudinal force slows the molecules down if they are flying into the decelerator in configuration I from position A to B. If molecules continue in this voltage configuration they will reach the top of the potential at position B and regain their kinetic energy on the downwards slope of the potential from position B to C. To prevent the latter, the Stark decelerator is switched to configuration II just before the molecules reach the top of the potential. Electrodes that were on ground and on high-voltage interchange

their roles and the molecules find themselves on the bottom of the potential in front of a new potential hill, losing more and more of their kinetic energy as this process is repeated. Since the amount of kinetic energy that can be taken out per stage is small, for OH molecules around 0.9 cm^{-1} or 1 % of the initial kinetic energy, the decelerator consists of many stages to be able to reach final velocities close to zero meter per second. The exact velocity that can be reached depends on characteristics of the Stark decelerator as the length and the applied voltage, and on molecular parameters, in particular the mass of the molecule, the strength of the Stark interaction and the initial velocity of the molecular beam. For a given set of parameters, the final velocity can be tuned by changing the *phase angle*, the moment of switching between configuration I and II.
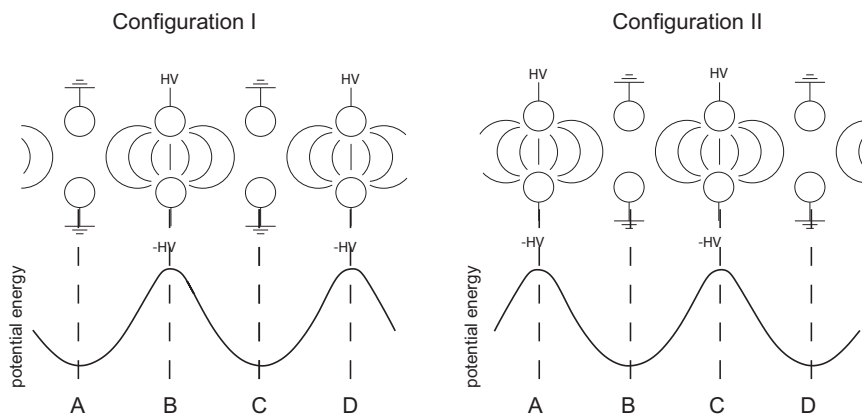
Figure 2.5: The operation principle of a Stark decelerator; molecules lose kinetic energy upon repeated switching between two high-voltage configurations I and II.

The phase angle ϕ defines the moment that the decelerator is switched between configuration I and II and can be described in terms of the trajectory of the molecule that always is exactly at that position when the fields are switched, the *synchronous molecule*. Positions A and B in figure 2.5 are now defined as position $\phi = -90^o$ and position $\phi = 90^o$, respectively. Position $\phi = 0^o$ is located exactly in between these two points. When operating 'at $\phi = 90^o$', the decelerator is switched when the synchronous molecule is exactly at the top of the potential hill. The maximal extent of the potential is used for deceleration and the molecule loses a maximal amount of kinetic energy per stage. In the $\phi = 0^o$ operation on the other hand, the synchronous molecule experiences no net decelerating force, the molecule is *guided* at a constant velocity. The operation of the decelerator at phase angles between 0 and 90 degrees can be used to decelerate the synchronous molecule to velocities at will,

whereas the operation at negative phase angles allows for acceleration.
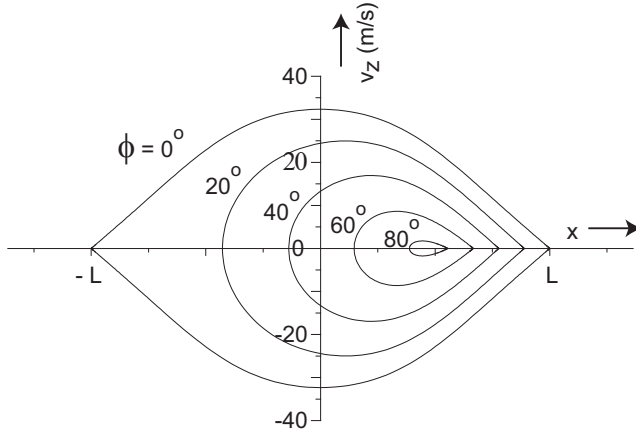
Figure 2.6: Phase-stable areas for operation of the Stark decelerator at 5 different phase angles, calculated for OH ($J = 3/2, |M| = 3/2$).

The phase angle that is used in the decelerator defines the velocity of the molecules, but has also important implications for the efficiency of the Stark decelerator. Molecules that are not synchronous but have a slightly different velocity or position, for instance, will lose more kinetic energy when the decelerator is switched from configuration I to II. The same flow of arguments can be formulated for molecules that have a slightly lower phase, or a velocity that slightly differs from the mean velocity. The group of molecules that undergoes this kind of oscillations around the synchronous molecule is said to be *phase-stable*. Trajectories can be well understood looking at the *phase-space* diagram in figure 2.6. The lines in this figure are calculated for electrode pairs at a voltage difference of 40 kV that are placed a distance 2L apart. During the deceleration process each molecule follows the contour that it started on and for each phase-angle molecules within a certain area are phase-stable. The larger the phase-angle, the smaller the phase-stable area and fewer molecules take part in the deceleration process.

The effect of the phase-angle on the deceleration of a given molecular beam pulse is illustrated in figure 2.7. The figure shows time-of-flight measurements of OH molecules measured using eight different phase-angles. Here, OH molecules were produced in an expansion with a Kr carrier gas resulting in a mean velocity of 450 m/s. The original molecular beam distribution has a mean arrival time of 2.9 ms, as indicated by the vertical dashed line in the figure. The arrival time of molecules guided by the decelerator at operation mode $\phi=0^o$ is not affected. The accelerated and decelerated molecules, however, arrive earlier and later in the detection region, respectively. The phase angles

used in this series of measurements ranges from ϕ=-40° (acceleration) up to ϕ=85° (deceleration), where in the last experiment the phase angle of the second part of the decelerator, that operates at a lower voltage, was set at ϕ=75°. The mean velocity of the packets of molecules that exit the decelerator ranges from 548 m/s to 112 m/s. It is seen that the number of decelerated molecules depends on the used phase angle, as follows from the phase-stable areas from figure 2.6. The structure that appears in all curves in the 2.2-3.5 ms region results from non-phase-stable molecules that arrive in the detection zone and is completely reproduced by 3-dimensional trajectory calculations (not shown).
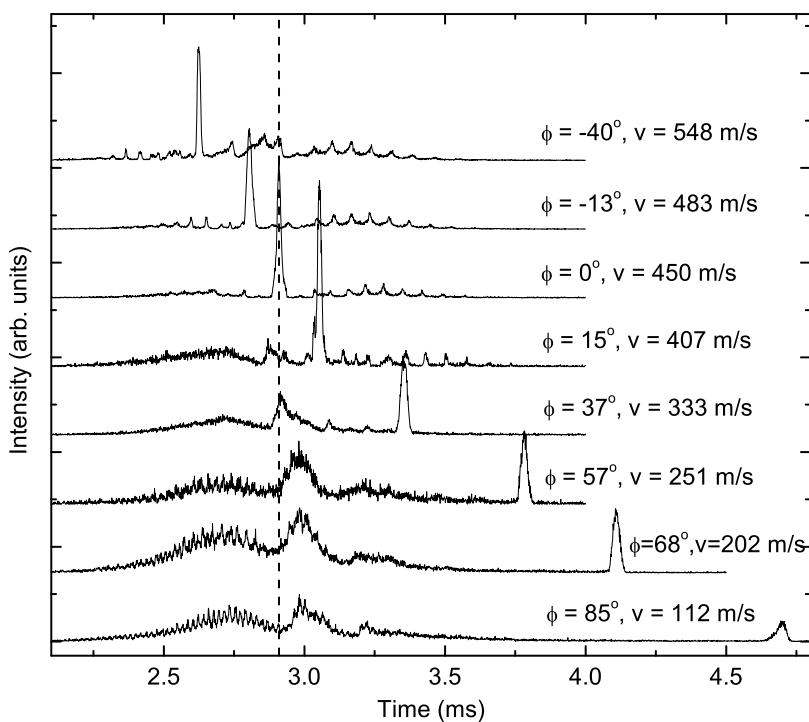

Figure 2.7: Time-of-flight profiles for accelerated and decelerated OH molecules. The operation of the decelerator at a range of different phase angles resulted in a range of final velocities of the molecular packet, indicated in the figure. The molecules were detected via off-resonant laser induced fluorescence with a cw laser. (see section 2.3.3)

2.3.2 Longitudinal and transversal motion

In recent years detailed knowledge has been gathered about the exact operation principle of the decelerator. The trajectories of the molecules in the decelerator are now well understood. The simple model of phase-space stability as described in section 2.3.1 breaks down for deceleration to the low velocities that are required for the loading of traps, as is discussed in chapter 7. Consequently, the packet of molecules may spread out leading to excessive losses. Also at higher velocities, couplings between longitudinal and transverse motions can lead to unstable regions within the phase-space areas as plotted in figure 2.6 [78, 85]. Recently Scharfenberg *et al.* [86] showed that these instabilities can be circumvented using a much longer Stark decelerator and higher-order operation modes.

In such a higher-order operation mode [87], characterized by the parameter s, the decelerator is not switched after the synchronous molecule has travelled the distance of one stage-length as in the section above, but only after it has passed a number of s stages. In the s=3 mode, for instance, the synchronous molecule travels over a distance of three stages before the decelerator is switched to a different voltage configuration. The molecules experience transverse focusing forces for a longer time, and the mentioned couplings are absent. The disadvantage of this approach is that a 3 times longer decelerator is needed to reach the same velocity compared to conventional s=1 operation. Figure 2.8 compares the guiding of OH molecules using s=1 and s=3 operation for the 108 stages long decelerator described in section 2.3.3. The two curves in the figure where measured for s=3 and s=1 guiding at slightly different velocities (450 vs. 440 m/s, respectively), as confirmed by the difference in arrival time observed in the figure. Since the signal of the OH molecules is a factor of $\sim$2 higher when the decelerator is operated in the s=3 mode compared to the s=1 mode, the former is often used when optimizing or calibrating other experimental parameters as molecular beam intensity and detection methods.

2.3.3 Experimental setup

The Stark decelerator used for the experiments throughout this thesis has been designed and built at the FOM-institute Rijnhuizen in the Netherlands in the years 2000-2003 and was extensively described in the PhD Thesis of Bas van de Meerakker [78] and in reference [88]. The experimental setup is shown in figure 2.9 and is briefly discussed below.

Before entering the decelerator the molecules pass a 37 mm long hexapole that is located 23.5 mm from the skimmer. The hexapole is used to focus the molecules into the decelerator and consists of 3 mm diameter rods that are placed on a circle of 6 mm diameter. Three of the rods are switched to a voltage of 8 kV when the molecular packet is inside the hexapole, whereas the others remain grounded. The Stark decelerator consists of two parts that are
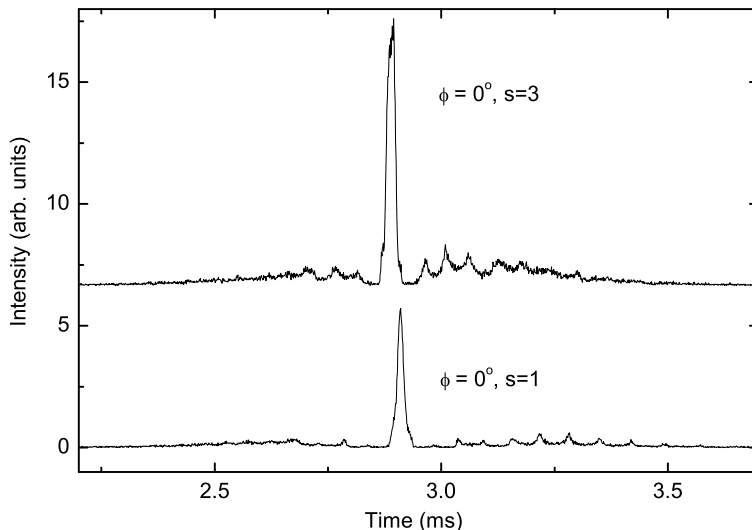
Figure 2.8: Time-of-flight profiles for OH molecules guided at ∼450 m/s for two operation modes of the decelerator, s=1 and s=3.

electronically and mechanically separated. The first part consists of 101 electric field stages and is operated at +20 kV and -20 kV. Parallel 6 mm diameter electrodes 10 mm apart (center to center) form pairs that are placed 11 mm apart, forming a 4x4 mm opening for the molecules. All even and all odd numbered electrode pairs are mounted on four stainless steel rods, and are always switched simultaneously. As schematically shown in figure 2.9 the second decelerator is built up differently to be able to combine the design with an electrostatic trap (section 2.4) and possesses 7 electric field stages that are operated at +15 kV and -15 kV. The fields in the second part of the decelerator are identical to the fields in the first part, except for a overall scaling factor of 0.75. The two parts of the decelerator are switched by a total of 8 fast high-voltage switches (Behlke Elektronik, HTS 651-03-GSM and 301-03-GSM).

The master trigger of each experimental cycle, which usually runs at 10 Hz, is the opening of the pulsed valve. The time delay of all other events, like the start of the switching of the decelerator and the firing of the lasers are synchronized by several delay generators (Stanford Research DG535). The sequence of high-voltage pulses applied to the decelerator and trapping electrodes is timed by a programmable pulse generator. A schematic representation of a time se-

quence of these high-voltage pulses is shown at the bottom of the figure 2.9. The construction and optimizing of such time sequences is extensively discussed in section 2.4.2.
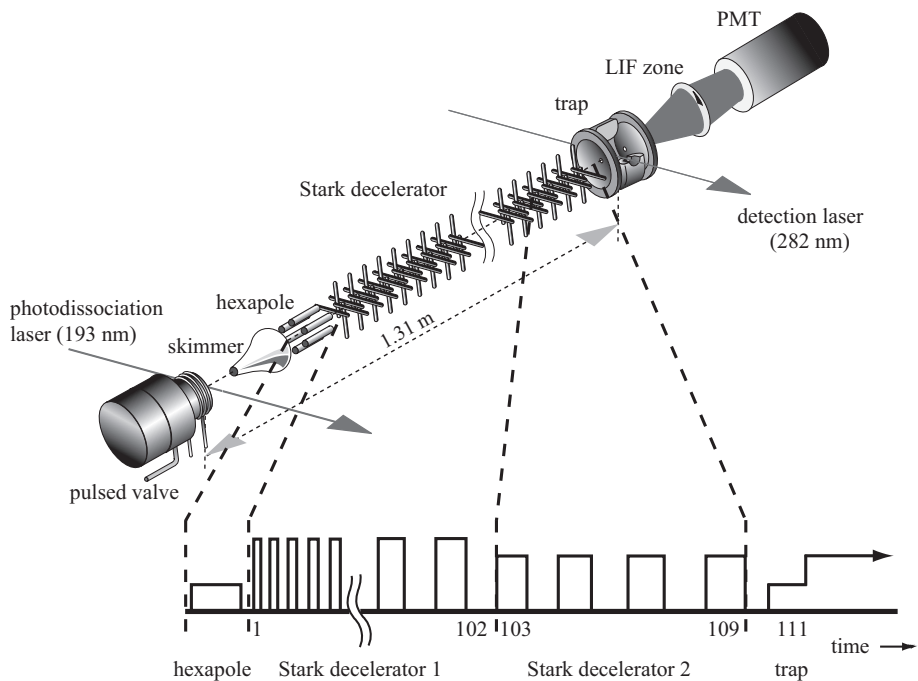
Figure 2.9: Scheme of the experimental set-up. Pulsed beams of OH, OD, NH, or CO molecules are produced in a supersonic expansion. The molecules pass through a skimmer, a hexapole, and a Stark decelerator and can subsequently be confined in an electrostatic trap. A schematic representation of the time sequence of high-voltage pulses is shown at the bottom of the figure, including selected indices of the switching times; see section 2.4.2 for details.

Good vacuum conditions are secured by four vacuum pumps (one Pfeiffer Vacuum TMU 1600M ($1400 \ \mathrm{ls^{-1}}$) and three TMU 400M ($400 \ \mathrm{ls^{-1}}$)) that pump three differentially pumped vacuum chambers. Under normal operating conditions the pressure in the source chamber is typically around $1 \cdot 10^{-5}$ mbar, and in the decelerator chamber around $3 \cdot 10^{-7}$ mbar. In the trapping chamber, where good vacuum conditions are essential to achieve long trapping times, the pressure is around $5 \cdot 10^{-9}$ mbar.

2.3.4 Detection

The OH radicals are state-selectively detected using a laser induced fluorescence (LIF) detection scheme. The 282 nm UV radiation of a pulsed dye laser excites the $A\,^2\Sigma^+, v = 1 \longleftarrow X\,^2\Pi_{3/2}, v = 0$ transition. The laser light is produced by a pulsed dye laser system pumped by a Nd:YAG laser. A photomultiplier tube (PMT) is used to measure the resulting off-resonant fluorescence, resonant light is effectively filtered out using narrow band mirrors. The data acquisition is performed via a digital oscilloscope (aquiris) and the data-acquisition program KouDA [89].
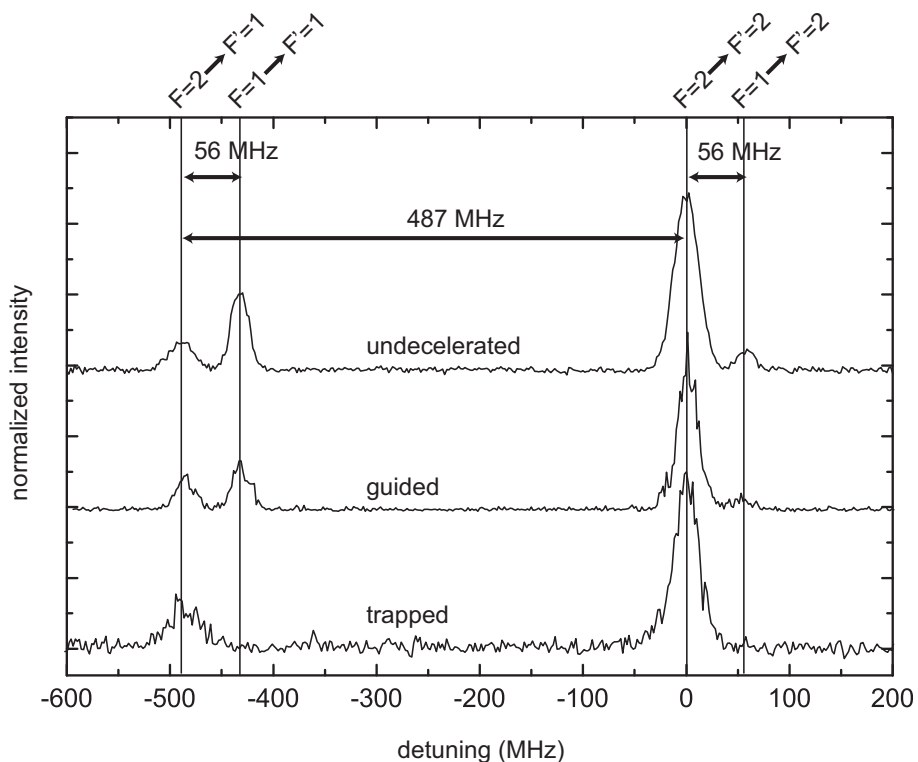
Figure 2.10: Spectrum of the $A\,^2\Sigma^+, v = 1 \longleftarrow X\,^2\Pi_{3/2}, v = 0$ transition in OH detected with a cw laser system. The spectrum is measured in three types of experiments, each with a different distribution of the molecules over the hyperfine levels F=1 and F=2.

Alternatively OH molecules were detected via the same electronic transition using a cw laser. For these experiments a cw ring dye laser pumped by an Argon-Ion laser with a bandwidth of $\sim$ 4 MHz in the UV (282 nm) was

used. Exploiting the narrow bandwidth of this laser, the hyperfine structure mentioned in section 2.1.1 can be resolved. Figure 2.10 shows the field-free hyperfine spectrum for three cases. The top profile shows a spectrum for un-decelerated, non-phase stable molecules, corresponding to the structure that appears in the 2.2-3.5 ms region in the time-of-flight profile of figure 2.7. In this case, both the low-field seeking F=1 and F=2 levels (see figure 2.1) are populated, since those levels all experience transverse focussing forces in the decelerator. The four lines that are observed result from the hyperfine split-ting in the $X\,{}^2\Pi$ ground state (56 MHz) and from the hyperfine splitting in the $A\,{}^2\Sigma^+$ excited state (487 MHz). The exact ratio of the intensities of the four lines in the spectrum is given by the transition intensities, together with the multiplicity factors of the corresponding levels. In the second profile, detected for molecules that were guided operating the decelerator at $\phi = 0^o$, a different ratio between the population of the F=1 and F=2 levels is observed; in this spectrum the F=2 lines are favored relative to the F=1 lines. The reason for this is that the guiding process has a larger phase-space acceptance for the F=2 hyperfine levels than for the F=1 levels because of the difference in Stark effect. If the decelerator is operated in a deceleration mode ($\phi > 0^o$) for the F=2 hyperfine level, the phase-space acceptance for the F=1 vanishes. This effect is observed in the lower spectrum of figure 2.10, where only molecules in the F=2 level are detected.

Detection of metastable NH molecules was performed in a similar way via a far off-resonant LIF scheme, using the spin-forbidden $A\,{}^3\Pi \leftarrow a\,{}^1\Delta$ transition around 584 nm [90], and the subsequent fluorescence to the $X\,{}^3\Sigma^-$ ground state around 336 nm. Although the use of a spin-forbidden transition for LIF detection of molecules is unconventional, this scheme is advantageous as it allows almost background-free detection by blocking the stray-light from the excitation laser with optical filters. The 584 nm light is generated by a narrow-band pulsed laser system. In this laser the output of a frequency stabilized single mode ring dye laser is amplified in a three stage pulsed dye amplifier pumped by a frequency-doubled injection seeded Nd:Yag pump laser. For the excitation, a 3 mm diameter laser beam with a pulse energy of up to 25 mJ in a 5 ns duration pulse, with a bandwidth of approximately 90 MHz, is used. This intensity is sufficient to saturate this weak spin-forbidden transition [90].

For the detection of metastable CO molecules in the trap no laser is needed. Where in other experiments metastable CO was very efficiently detected by counting emitted electrons from a gold surface hit by the CO molecules [80], we chose the straight-forward method to just measure the resulting photons when a CO molecule spontaneously decays back to the ground state. This method is usually less efficient for the detection of molecular beams of CO molecules, as molecules leave the detection zone within the relatively long lifetime of this excited state (2.63 ms for the ${}^3\Pi_1$ state and 143 ms for the ${}^3\Pi_2$ state, see chapter 6). As trapped molecules do not suffer from this effect, this detection scheme is efficient even for the long lifetimes involved.

2.4 Trapping

In the experiments with trapped molecules that are described in this thesis, a number of traps with different designs have been used. This section focusses on the general principles of electrostatic trapping, using OD ($X^2\Pi$), NH ($a\,^1\Delta$), and CO ($a^3\Pi$) molecules as an example. A full description including experimental details of the new electrostatic trap and a detailed comparison of the different traps can be found later in chapter 7.

2.4.1 Trapping principles

Slow molecules that emerge from the Stark decelerator can be loaded into an electrostatic trap following a two-step loading scheme that is schematically shown in figure 2.11. In the *loading* geometry, the trap electrodes are configured such that they create a potential slope for the molecules that enter the trapping region at position A. At the moment that the molecules have lost their last bit of kinetic energy on this slope and have reached the center of the trap (position B), the trapping electrodes are switched to the *trapping* configuration where they form a quadrupole potential geometry and molecules remain trapped. The number of trapped OH molecules, as well as the temperature of the trapped gas critically depends on the details of the trap-loading sequence, and in particular on the velocity with which the molecules enter the trap [47]. If this velocity is chosen such that the molecules come to a standstill exactly at the center of the trap, a distribution corresponding to a temperature of 20 mK can be reached. The required velocity of the packet is so low, however, that the packet spreads out before entering the trap, and a significant fraction of the packet can not be confined. Loading the trap with a faster beam reduces this spreading out and a higher number of trapped molecules can be obtained. In this approach, however, the molecules come to a standstill past the center of the trap, and the final temperature is higher. Trap designs that allow for both a low temperature and a high number of trapped molecules are presented in chapter 7.

In figure 2.12 the time-of-flight profiles of the trapping of OD (panel a), metastable NH (panel b), and metastable CO ($a^3\Pi_1$) (panel c), the three new species that were trapped during the course of the research presented in this thesis, are shown. These profiles are typical for the trapping of OH as well. The arrival of undecelerated molecules that were not accepted by the decelerator in the trap center is followed by the steady signal of trapped molecules. The trap is switched on about 8 ms after the molecular beam is produced in the measurements on OD and CO, whereas in the measurement on NH the trap is switched on after about 6 ms. The oscillatory structure that is seen in the first few milliseconds after the trap is switched on is caused by phase-space dynamics that are discussed extensively in chapter 7 of this thesis. For CO molecules, an additional overall 1/e temporal decay of the signal intensity in the time-of-flight profile is observed, that is caused by the radiative lifetime of the metastable
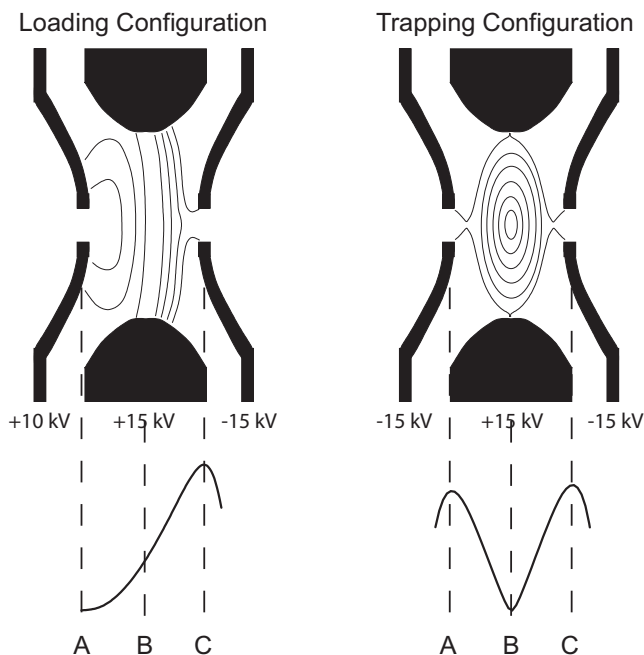
Figure 2.11: Schematic representation of the trap loading procedure. Molecules enter the trapping region at position A in the loading configuration, are brought to standstill on a potential hill, and subsequently confined around position B in the trapping configuration. The full details of the trap loading procedure can be found in chapter 7.

state. In the insets of the figure, the signal of the trapped OD and NH molecules is shown on a longer timescale. It is seen that the $1/e$ trap lifetime for OD, NH, and CO is 3.6 ± 0.1 s, 1.4 ± 0.1 s, and 2.63 ± 0.03 ms, respectively. The different mechanisms that lead to trap loss are quantitatively studied in the experiments that are presented in chapter 5. For CO, the $1/e$ trap lifetime directly reflects the radiative lifetime of the metastable state, as is presented in detail in chapter 6.

2.4.2 Optimizing the beamline[*]

The efficiency of the deceleration and trap-loading process can be improved in different ways. One way is to optimize the design of the high-voltage electrodes,
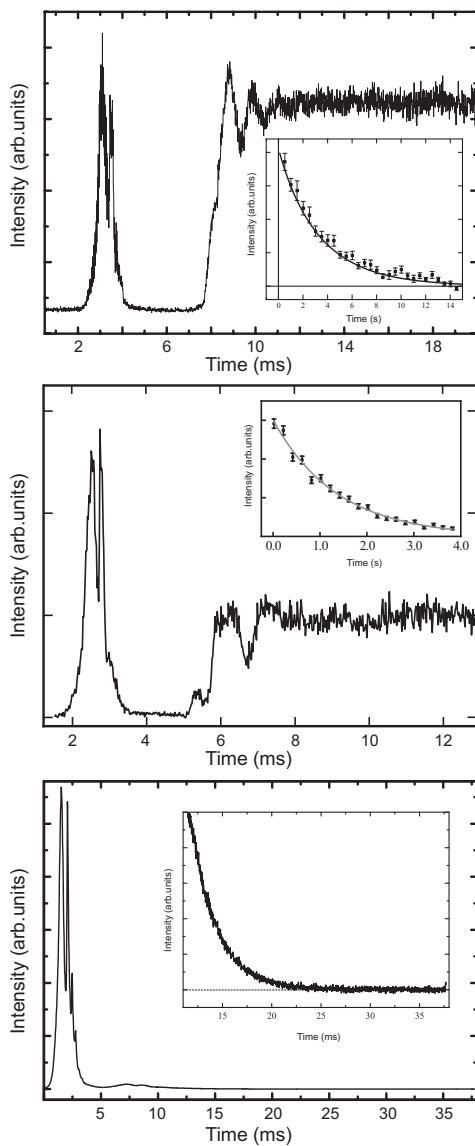
Figure 2.12: Time-of-flight profiles of electrostatic trapping experiments shown for ground state OD molecules (top panel), metastable NH ($a^1\Delta$) molecules (middle panel), and metastable CO ($a^3\Pi_1$) molecules (lower panel). The insets of the panels show the signal in the trap for longer time scales (top, middle) or on an expanded vertical scale (lower).

as extensively discussed in chapter 7. For a given design, the efficiency of the deceleration and trap-loading process critically depends on the exact timings of the high-voltage pulses. In typical deceleration and trapping experiments described in this thesis, a sequence of more than one hundred high-voltage pulses is applied to the various elements in the beamline. The time sequence that is used is inferred from a detailed knowledge of the electric fields in the decelerator and trap region, and the Stark effect of the molecule of interest. This, however, does not account for possible deviations from an idealized description of the experiment, like, for instance, misalignments of the electrode arrays and instabilities of the applied high-voltage pulses. Furthermore, these calculations are based on a one-dimensional model to describe the longitudinal motion, while the transverse motion of the molecule effects the efficiency of the decelerator as mentioned in section 2.3.2. A manual optimization of the time sequence is practically impossible for this complicated and large parameter space. In this section the successful implementation of an evolutionary algorithm for the automated optimization of a Stark-decelerator beamline is demonstrated.

Evolutionary algorithms (EA), mimicking the biological principles of evolution, have been frequently used for automatic optimization of experimental problems with a large parameter space and noisy feedback signals. As early as the 1960's three independent developments started with the introduction of evolutionary strategies (ES) by Rechenberg and Schwefel [91, 92], evolutionary programming (EP) by Fogel, Owens and Walsh [93], and genetic algorithms (GA) by Holland [94]. A nice introduction to the field of evolutionary computing and its different dialects is given by Eiben and Smith [95].

Feedback control optimization

In the optimization procedure, initial time sequences are calculated based on a theoretical model of the experiment and will be referred to as *calculated* time sequences. For the feedback control optimization the LIF intensity of trapped OH molecules, as described in section 2.3.3, is recorded. To avoid effects from the oscillations of the molecular packet inside the trap that appear during the first milliseconds after switching on the trap (see figure 2.12), the LIF intensity is measured after 20 ms trapping-time. For every datapoint 64 successive measurements are averaged. The signal-to-noise ratio of the trapping experiment under these conditions is about twenty. This measurement of the OH density in the trap is used as objective function (fitness) in the feedback control algorithm. Since the lifetime of the OH radicals confined in the trap is as long as 1.6 s (chapter 5), the number of detected OH molecules after 20 ms is still > 98 % of the maximum value. Because the LIF signal at that detection time is practically constant over periods much longer than the timing changes due to the feedback control algorithm ($\ll$ 1 ms), pulsed laser excitation at a fixed time can be applied for the molecule detection. Note that in the feedback

control loop implemented here, we use the result from previous experimental runs as feedback for following ones.

This given problem requires the optimization in a large parameter space, which at the same time can only be sampled by a slow and noisy evaluation. For such problems evolutionary algorithms are generally a good choice and have been applied successfully in many fields. The individual parameters to be adjusted are the timings, t_i, that determine the exact switching of the high-voltages energizing the deceleration and trapping electrodes. For the given experiment this results in 111 parameters to be optimized. For a detailed depiction of the timing numbering see figure 2.9. To reduce the high dimensionality of the parameter space, we refrained from optimizing all parameters individually, and encoded them in three reduced sets of parameters instead: The timings of decelerator 1 and the first 4 timings of decelerator 2 are not optimized independently, but described by two sets of polynomial expansion coefficients. We found that an accurate encoding of the time sequence itself requires a polynomial of high order, i.e. orders larger than twenty for a 5 μs accuracy. To allow for smaller polynomial orders o_1 and o_2 for the two parts of the decelerator, we have only encoded the differences to the calculated time sequence $t_i - t_{i,0}$ in the polynomial, allowing for considerably smaller expansions, since they only need to describe deviations from the theoretical timings. For decelerator 1, one obtains timings for $i = 1$–102

$$t_i = t_{i,0} + \sum_{j=0}^{o_1} p_{j+1} \cdot (i-1)^j \tag{2.8}$$

and for decelerator 2 timings for $i = 103$–106

$$t_i = t_{i,0} + \sum_{j=0}^{o_2} p_{j+o_1+2} \cdot (i-103)^j \tag{2.9}$$

The remaining 5 timings for the last deceleration stages and the trap-loading and trapping configurations, which are the most critical timings, are optimized individually and independently. To decouple them from the changes of earlier timings, they are encoded as time difference to their respective preceding timing, i.e. we use

$$\Delta t_i = t_i - t_{i-1} = p_{i+o_1+o_2-104} \tag{2.10}$$

for $i = 107$–111. The complete parameter vector used in the optimization is then encoded as

$$\vec{P} = (p_1, p_2, \ldots p_{o_1+o_2+7})^T \in \left(\mathbb{R}^+\right)^{o_1+o_2+7} \tag{2.11}$$

Typically we have used polynomials of order $o_1 = 2$ for decelerator 1 and order $o_2 = 1$ for decelerator 2, resulting in a parameter vector of length ten. In this way the dimension of the parameter space is reduced by one order of magnitude

compared to the initial one, while control over the whole beamline with the feedback loop is maintained.

With the intuitive representation of the individuals of the optimization problem as a vector of real numbers over a continuous parameter space, the choice of evolutionary strategies is a natural one. ES is a EA dialect that uses a representation of real-valued vectors and generally uses self-adaptivity [95]. In the experiments described here we used the Evolving Object (EO) framework [96] implementation of the ES. As a trade-off between problem size in the ES and theoretical convergence, the *eoEsStdev* ES strategy, applying uncorrelated mutations with individual step sizes, was used [95]. In this self-adaptive strategy the genotype is a vector of real numbers containing the actual optimization parameters as well as individual mutation widths σ_i for every parameter p_i.

The initial optimization parameters used were based on the suggestions by Eiben and Smith [95] and successively adopted according to their success in the experiments. In the most successful optimization runs the following parameters were used: typically a population size of five or ten individuals was used, with population sizes up to forty in some runs. Typically thirty offsprings were generated every generation, with values ranging from the actual population size to six times the population size over different runs. Generally, an offspring-to-population ratio of seven is assumed to work best, but the theoretical advantage is apparently outweighed by the slowness of the evaluation and the corresponding experimental difficulties in this experiment. The most successful mutation and crossover rates were 75 % and 50 %, respectively, but this seems not to be critical and was not tested extensively. Parent selection was done using the ordered sequential selector. We have used discrete global recombination for the experimental parameters and intermediate global recombination for the mutation widths σ. For survivor selection the (λ, μ) approach worked best, as it seems to handle noise and drifts in the experimental conditions well, as is generally assumed [95, section 4.7]. Elitism was not applied.

This machine learning is implemented in our data-acquisition system KouDA [89] using ES within an automatic feedback control loop.

Experimental results

The experimental setup and experimental parameters as described in section 2.4.1 were also used for the experiments presented in this section. In figure 2.13 the normalized average fitness — the LIF signal from OH radicals in the trap — per generation is plotted against the generation number for three different optimization runs, referred to as runs A, B, and C. The measured fitness-values are normalized with respect to the fitness obtained for the calculated time sequence under the same experimental conditions. In each run, different strategy parameters for the algorithm or different initial populations are used, as detailed below. Typically, a complete optimization run corresponds to the eval-
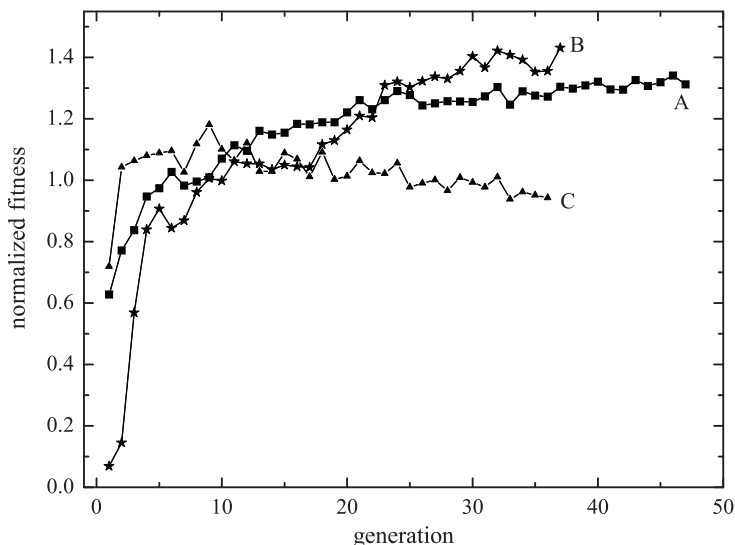
Figure 2.13: For three different optimization runs, each with different initial parameters, the average fitness per generation is plotted. Curve A (squares) and B (stars) show an increase of 30 and 40 % respectively. During the measurement represented by curve C (triangles) drifts in the experimental conditions, namely the backing pressure of the supersonic expansion, occurred and lead to reduced signal intensities, as was confirmed after the optimization run.

uation of many hundred generated time sequences and takes about 1–2 hours of measuring time.

In run A (squares), the calculated time sequence is used as a starting point for the optimization. From this sequence, an initial population is created with parameters that are randomly picked out of a Gaussian distribution around the calculated values. The last parameter, Δt_{111}, has been decreased by 27 μs based on the outcome of earlier runs (not presented). As a result of these small changes, the first generation has a slightly lower fitness. After 9 generations the average fitness of the generation has increased to the value of the calculated time sequence. For later generation numbers the fitness increases further and reaches a maximum of 1.3 after 46 generations. In the measurement represented by curve B (asterisks) an initial population was created from the same calculated time sequence, but 9 out of 10 parameters were set off by 3 to 20 %. Hence, the first generation time sequences lead to a normalized fitness of less than 0.1. After 11 generations this number already reaches 1 and is further optimized to 1.4 in generation 37. The optimization runs A and B result in a number of trapped OH radicals that is 30 to 40 % higher than the number that is obtained with the calculated time sequence. Other experiments where different initial

34

populations were chosen led to a similar increase in the number of trapped molecules.

The initial population and strategy parameters, that are used in the optimization run shown in curve C (triangles), are very similar to the parameters that were used in curve A. Curve C initially shows (as expected) an optimization similar to that of run A and reaches a maximum of 1.2 after around 9 generations. From then on, however, the fitness starts decreasing. This is due to a drift in the production of OH radicals during this experimental run, that was confirmed by an independent measurement after the optimization run. In spite of this drift the algorithm still converged and the time sequences obtained for the last generation are comparable with time sequences obtained in runs A and B (*vide infra*).

Other experiments using different strategy parameters for the ES, for example, different population sizes or different settings for mutation and crossover rates, did lead to a similar increase in the number of trapped molecules of 35–40 %. Furthermore, the values of corresponding parameters from the optimized time sequences are generally comparable. These results show not only that the algorithm is able to optimize the number of trapped molecules, but also that it finds a reproducible maximum in the parameter-space, even if the initial parameters deviate significantly or external factors disturb the experiment.

The evolutions of three of the most important parameters, recorded during optimization run A, are shown in figure 2.14. Figure 2.14 a and 2.14 b show Δt_{108} and Δt_{109}, respectively. These parameters define the switching times of the last two stages of decelerator 2 and thus determine the exact velocity with which the molecules leave the decelerator. Figure 2.14 c depicts the evolution of Δt_{111}, the time interval during which the loading configuration of the trap is used. At the end of this time interval the trapping configuration is switched on. For reference, the horizontal lines in the plots denote the mean value of the respective parameter in the first generation, which are equivalent to the parameters in the calculated time sequence. Although the fitness depends very critically on these specific timings, the evolution of the parameters shown in figure 2.14 is typical for the evolution of less critical parameters as well.

For all three parameters, the mutation widths σ, represented by the vertical bars, are initially large and the parameters scatter over a relatively large range. As the generation number increases, this mutation width decreases and the parameters converge. Parameter Δt_{111}, however, converges initially to two values, one centered around 1662 μs, the other around 1674 μs. This shows that the parameter-space contains multiple local maxima, and that multiple pathways in the parameter-space can be followed. Only after 27 generations, exclusively individuals with a value for Δt_{111} of about 1674 μs survive the selection. As most runs converge to similar values this seems to be the global optimum, at least for the parameter space searched.

From each feedback control experiment a set of optimized time sequences is obtained. It is clear from the optimized time sequences, that no different
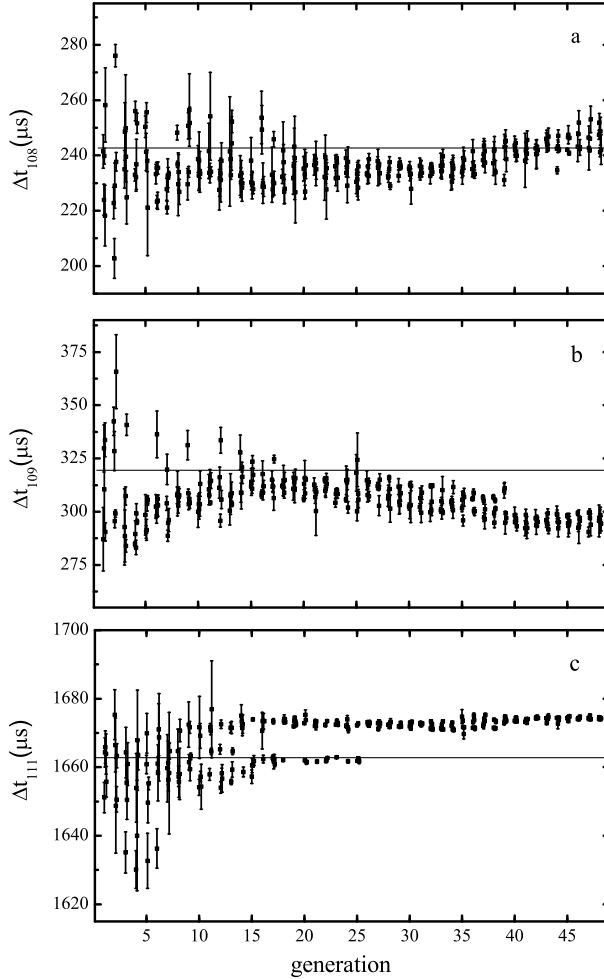
Figure 2.14: The evolution of three of the parameters during optimization run A (see figure 2.13): a) Δt_{108}, b) Δt_{109}, c) Δt_{111}. The squares mark the value of individual parameters and the error bars represent the corresponding mutation widths σ. Only the five parameters selected for a new population are shown and they are grouped by generation. Individual parameters within a population are slightly offset horizontally to allow the observation of individual values and their error bars. At the beginning a large range of the parameter space is searched, whereas later in the optimization the σs are reduced by the algorithm and convergence is reached. The horizontal lines denote the mean value of each parameter in the first generation.

36
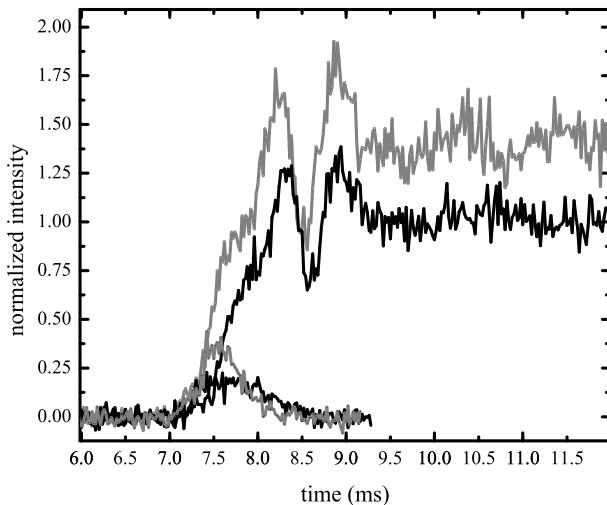
Figure 2.15: Density of OH radicals at the center of the trap as a function of time after the opening of the nozzle. The lower two traces are the intensities of molecules passing through the center of the trap without any voltages applied to the trap electrodes. The upper traces are measurements for trapping experiments. The black traces are measured with the calculated time sequence applied to the machine, whereas the gray traces are measured with one of the generated, optimized time sequences obtained from automated optimization using evolutionary strategies.

mode of operation for the Stark decelerator is obtained and that the previous theoretical understanding [97] is confirmed by these experiments. Moreover, comparing the time-of-flight (TOF) profiles of OH radicals at the center of the trap, that are measured using the calculated and optimized time sequences, a physical interpretation of the differences can be deduced.

The typical result of such a measurement is shown in figure 2.15. The black and gray curves are measured using the calculated and optimized time sequences, respectively. The lower two curves show the TOF profiles of the OH molecules as they arrive in the trap when no voltages are applied to the trap electrodes. The positions and widths of the arrival-time distributions are a measure of the longitudinal velocity distributions of the decelerated OH beams that exit the decelerator. Compared to the calculated time sequence, the optimized sequence results in an arrival-time distribution that is shifted 180 μs

to the left, indicating that the molecular packet arrives with a higher mean velocity of 25 m/s, instead of 21 m/s, in the trap. Assuming the transverse and longitudinal velocity spreads are unaltered for the optimized time sequence, the beam spreads out less in all directions while travelling the distance from the end of the decelerator to the trap, and the corresponding arrival-time distribution is narrower. The integral of the peak of the arriving packet (lower curves) is already enhanced by about 40 %, reflecting the reduced transverse spreading out of the beam and hence the reduced transverse losses while entering the trap.

The upper two curves show the density of OH radicals at the center of the trap when the trap-loading and trapping electric fields are applied. The optimized time sequence (gray curve) leads to a more pronounced oscillation in the TOF profile than the calculated one (black curve). This is readily understood from the higher initial velocity of the molecules. The molecules enter the trap too fast, and come to a standstill past the center of the trap. The molecular packet is poorly matched to the trap acceptance, and the width of the velocity distribution of the trapped molecules will therefore be higher as well. These results confirm, as was already concluded earlier in section 2.4.1, that a large number of molecules in the trap and a low temperature of the trapped packet of molecules are conflicting goals with the present design of the trap: the required low velocity to match the decelerated molecular packet with the acceptance of the trap results in a large transverse spreading out of the packet prior to entering the trap.

In principle, one could also aim a feedback control optimization at determining a time sequence for a trapped molecular packet with a temperature as low as possible, or a weighted combination of the number of trapped molecules and a minimal temperature, by using an appropriate experimental objective function. One could, for example, measure the number of molecules at the center of the trapping region after a predefined time of free expansion of a previously trapped packet. That would result in a combined determination of the peak density of the trapped molecular packet and its temperature, where the time delay between switching off the trap and the detection of the molecular density would weigh the two contributions to the fitness. Alternatively, if the spatial density distribution of the trapped molecular packet would be measured for every generated time sequence, direct information on the number of trapped molecules and their temperature is obtained, allowing to define any objective function based on these two important measures. Furthermore, when using continuous detection to allow for measuring the complete time-of-flight profile from the nozzle to the detection region for every molecular packet, the integrated intensity and the longitudinal temperature can be deduced offline by the optimization algorithm. This allows the optimization of any Stark-decelerator beamline, even without trapping.

Besides the timings of the high-voltage pulses one can also optimize other computer controllable experimental parameters, such as the voltages that are

applied to the experiment, laser frequencies, etc. In general, evolutionary algorithms can be used for the optimization of any fitness function that can be determined experimentally. This includes, for example, the ratio of molecules simultaneously trapped in two different quantum states or the ratio of decelerated and actually trapped molecules. More generally, the method can also be applied to other atomic and molecular beam experiments, such as optimizing the timings or voltages in multipole focusers [98] or the currents in a Zeeman slower [99] or a Zeeman decelerator [56].

2.5 Characterization of trapped molecules

Information on the trapped cloud of molecules can be inferred from different kinds of measurements. The methods of Cavity Ringdown Spectroscopy and Laser-Induced Fluorescence are used to get quantitative information on the number density of the trapped molecules. In the final part of the following section the possibility of determining the temperature is discussed. In chapter 5 this description is extended to the characterization of the several trap loss processes that play a role after molecules are trapped.

2.5.1 Cavity Ringdown Spectroscopy

The most straight-forward method to detect molecules and get accurate information about their number density is direct absorption spectroscopy. The typical number density in molecular beams, however, is too low to observe absorption in a single pass. An alternative technique that allows for quantitative diagnostics of molecular species is Cavity Ringdown Spectroscopy (CRDS) [100]. In a CRDS experiment the molecules of interest are measured inside a cavity, were the laser light can pass the molecular cloud -depending on the reflectivity- many thousands of times, thereby experiencing a effective path-length of many kilometers. In pulsed CRDS, a laser pulse is coupled through the first mirror into the cavity and starts to reflect back and forth between the two mirrors. Each roundtrip a percentage of the light is transmitted through the second mirror. The intensity of this transmitted light, that can be measured for instance with a photomultiplier tube, will decay exponentially over time. The time constant of the decay time τ is given by the relation

$$\tau = \frac{d}{c(1 - R + \sigma n l)}.$$ (2.12)

In this equation σ is the absorbtion cross section of the measured transition and l the interaction length of the laser field with the absorbers. Given the length of the cavity d and the velocity of light c, the time constant of the decay of the empty cavity ($n = 0$) is a direct measure for the reflectivity of the mirrors

R via the relation $(1 - R) = \frac{d}{\tau c}$, if the two mirrors have identical reflectivity. The change of the time constant upon absorption by molecules can be used to determine the absolute number density, n, of the absorbers.

To measure the number density of the OH beam using CRDS, a cavity of a length of 22.4 cm was placed in the detection chamber, where the trap electrodes were taken out to create the necessary space. The OH beam used in the experiments was produced with Kr as a seed gas and was guided by the decelerator in the s=3 operation mode (section 2.3.1) with a mean velocity of 435 m/s. The center of the cavity was located 24 mm behind the last decelerator stage. The mirrors (Laseroptik, R=99.7 %, focal length -1 m) were mounted in conventional (Thorlabs) mirror mounts. To constrain non-centric cavity modes, we mounted a 4 mm slit inside the cavity under a 45° angle with both the laser beam and the molecular beam. The $Q_1(1)$ transition of the $A^2\Sigma^+, v = 0 \leftarrow X^2\Pi, v = 0$ band at 308 nm [101] was used for detection. The required laser radiation is generated by a narrow-band pulsed laser system. In this laser the output of a frequency stabilized single mode ring dye laser is amplified in a three stage pulsed dye amplifier pumped by a frequency-doubled injection seeded Nd:Yag pump laser. The frequency of this radiation is doubled using optical conversion crystals resulting in 308 nm light with a bandwidth of ~120 MHz. The light transmitted through the cavity was collected via a lens placed a few cm behind the last mirror and sent directly into a PMT. For the fitting of the measured exponential decay rates, the so-called three-points-method from reference [102] was implemented in our data-acquisition programm KouDA.

The sensitivity that can be reached with CRDS depends on the accuracy $\Delta\tau/\tau$ with which the decay time can be measured [103]. From equation 2.12 it follows that

$$\sigma n l > (1 - R)\frac{\Delta\tau}{\tau} \qquad (2.13)$$

for the minimal number density n that can be measured. In the present experiment an accuracy of $\Delta\tau/\tau = 1 \cdot 10^{-3}$ was reached. The interaction length is given by the diameter of the molecular beam (0.3 cm). Since after the decelerator the majority of the molecules reside in the F=2 hyperfine component of the rotational ground state and the laser bandwidth is sufficiently small to resolve the hyperfine structure, the value for σ [104] of the $Q_1(1)$ electronic transition has to be corrected taking the branching ratio of the four hyperfine transitions within the $Q_1(1)$ transition into account. Those relative strengths can be calculated from the Hönl-London factors for OH [105] and lead to a σ of $5.7 \cdot 10^{-14}$ cm^2 for the $F = 2 \rightarrow F' = 2$ hyperfine transition as used in the present experiment.

A change in the decay time of the detected transmitted light due to absorption of OH molecules could not be measured within the present accuracy, and equation 2.13 gives an upper limit for the density of OH molecules in the guided beam, $n_{guided} < 2 \cdot 10^8$ cm^{-3}. From LIF measurements (not shown) we

know that the ratio between the number of detected trapped and the number of detected guided (s=3 operation mode) molecules is about $\frac{N_{trapped}}{N_{guided}} = \frac{1}{25}$. Using this ratio, we find the upper limit for the density of the trapped packet $n_{trapped} < 8 \pm 4 \cdot 10^6 \ cm^{-3}$. To convert this upper limit for the density into an upper limit for the absolute number of trapped OH molecules, we need to take the detection volume into account. Based on simulations, we assume that this volume is not limited by the detection laser, but by the size (3x3x3 mm) of the trapped packet itself, giving a volume of $V_{det,trapped} = 0.027 \ cm^3$. This gives an upper limit for the absolute number of trapped molecules of $N_{trapped} < 2.3 \cdot 10^5$.

2.5.2 Laser Induced Fluorescence

The method of Laser Induced Fluorescence (LIF) itself, as described in section 2.3.3 and used for most experiments throughout this thesis, does not directly provide an absolute value for the number density of the detected molecules. If, however, experimental factors like the solid angle (SA) of the detection and the cross-section area between laser and molecular beam are characterized well, an accurate LIF experiment can be used to get an estimate of the absolute number and density of a trapped packet of OH molecules.

To perform such an experiment, the setup as described in section 2.3.3 was extended with a second detection zone at a distance of 25.4 cm after the trap center. The molecules with a velocity of 434 m/s arrive here 585 μs later than in the trap center and are excited via the $Q_1(1)$ transition of the $v = 0 \rightarrow v = 1$ band at 282 nm [101] by a laser pulse with a 3.5 mm diameter and a power of ~1.5 mJ, sufficient to saturate the transition. The resulting fluorescence was collected by a PMT, the front surface of which is at 10.4 cm from the center of the laser beam. In the PMT 10 photons per shot were measured. To convert this signal into a number of molecules several factors have to be taken into account, illustrated by the following equation:

$$N_{guided} = 2 \frac{1}{SA \cdot T \cdot Q} N_{detected \ photons}. \tag{2.14}$$

The effective opening of the PMT is limited to a 12 mm diameter, such that the solid angle is given by $SA = \frac{1}{4}(\frac{6}{104})^2 = 8.3 \cdot 10^{-4}$. The total number of guided molecules that is excited by the laser in the second detection zone is inferred from the transmission efficiency $T = 0.6$ for the fluorescence of the total filter set and the quantum efficiency of the PMT (Q=0.3). Since the excitation transition is saturated, an additional multiplication factor 2 gives the absolute number of guided molecules. This number can be converted to the total number of guided molecules in the first detection area, taking the distance, velocity, and transverse velocity spread into account. Using the conversion factor of 25 between guiding and trapping and the detection volume, we get an estimate for the number density in the trap of $n_{trapped} = 3.0 \pm 2.0 \cdot 10^6 \ cm^{-3}$, consistent with the upper limit of $8 \pm 4 \cdot 10^6 \ cm^{-3}$ that resulted from the CRD measurements.

2.5.3 Temperature measurements using a cw laser[*]

An important property of the trapped gas is the temperature. Measuring the temperature, however, is notoriously difficult. The temperature can in principle be determined by measuring the spatial distribution of the molecular cloud, as the spatial and velocity distribution of the molecules in the trap are coupled. In trapping experiments with ND_3 molecules, that are detected using a Resonance Enhanced Multi Photon Ionization (REMPI) scheme with a focussed laser, the spatial distribution can be measured by mechanically scanning the laser focus along a symmetry axis of the trap [97]. This strategy can only be implemented if the detection laser beam is (much) smaller than the size of the molecular cloud. When LIF is used as a detection scheme, the laser beam can usually not be made small enough to measure the spatial distribution this way. When the laser beam is comparable in size to the molecular cloud, however, the temperature can be deduced from the spectral profile of the molecules in the presence of the trapping potential, a method that has, for instance, been applied to magnetically trapped CaH molecules [106]. Unfortunately, if the excitation wavelength is in the ultraviolet part of the spectrum, scattered photons can release electrons from the trap electrode material. This can cause electrical breakdown in electrostatic traps, and has thus far hampered the application of this method to electrostatically trapped molecules.

The detection scheme that is used in the NH trapping experiment, as described in section 2.4.1, does not suffer from these limitations, as the 584 nm radiation can safely be used to excite the molecules while the trap electrodes are still on high voltage. In the main part of figure 2.16 three different spectral profiles of the $P_2(2)$ line are shown, all recorded after 16 ms of trapping. The origin of the horizontal axis is set at the center of the field-free line profile, indicated as profile (I). This line profile is measured 10 μs after the trap electrodes are switched off and grounded. This time interval is sufficiently short that the molecules do not move significantly, while being long enough to ensure field-free conditions. A near-Gaussian lineshape with a FWHM of $\sim$ 130 MHz, mainly determined by the bandwidth of the laser, is observed. Weak shoulders due to partly resolved hyperfine structure and the intrinsic spectral structure in the laser pulse can be recognized in this profile.

Also shown are two broadened line profiles, (II) and (III), observed when the molecules are excited in the presence of the trapping potential. In the electric field of the trap, the trapped molecules in the $a\,^1\Delta, v = 0, J = 2$ level and the $A\,^3\Pi_1, v' = 0, J' = 1$ level both experience a positive Stark shift. Since the Stark shift for molecules trapped in the $a^1\Delta$ state is considerably larger than the Stark shift in the excited $A^3\Pi_1$ state, a broadened profile of the $P_2(2)$ line results that is shifted to lower frequencies. The difference between profile (II)
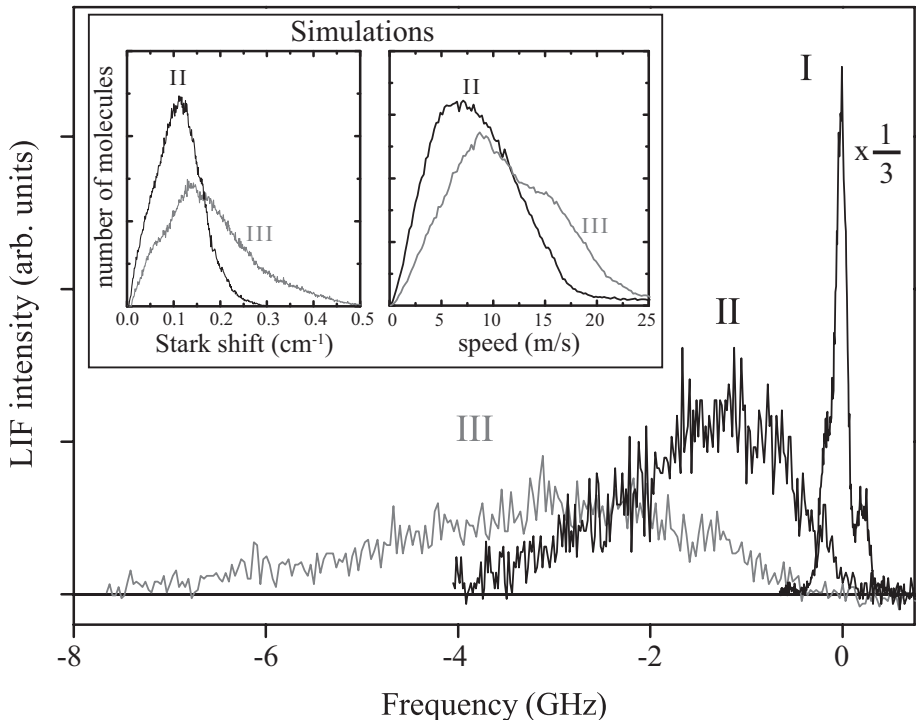
Figure 2.16: Spectral profiles obtained by scanning the detection laser frequency over the highest frequency component of the $P_2(2)$ transition in NH, which excites the trapped molecules from the $a^1\Delta$ to the $A^3\Pi$ state. The field-free profile (I) is shown, scaled down by a factor 3, together with the profiles obtained while the shallow (II) or deep (III) trapping field is on. In the inset the result of numerical simulations is given, showing the number of trapped molecules as a function of their Stark shift and speed.

and (III) reflects the difference in the depth and slope of the trapping potentials that are being used; the deceleration and trap loading process is identical in both cases. Profile (II) is recorded when the ring electrode of the trap is grounded, whereas a voltage of +15 kV is applied to this electrode to record profile (III). The endcaps of the electrostatic trap are at a potential of -15 kV in both cases. The resulting trap potentials therefore differ in slope and depth by a factor of two, and are referred to hereafter as 'shallow' (II) and 'deep' (III).

The laser excitation and fluorescence detection in the experiment is done through holes in the trap electrodes, inevitably restraining access to the trapping volume. For a direct determination of the temperature of the trapped

molecules from the measured line profiles a complicated instrument function would have to be taken into account; the laser position, its spatial intensity profile and the spatial sensitivity of the detection system have to be accurately known. Therefore, a detailed analysis of the line profiles intrinsically has many uncertainties. However, information on the energy and the position of the molecules in the trap can also be obtained in a straightforward manner by comparing the experimental line profiles with each other. In such a comparison, complications related to details of the excitation- and detection-processes cancel out.

The integrated signal of the three line profiles is, within experimental accuracy, the same. Moreover, if profile (II) is stretched out in frequency by a factor of two, and reduced in intensity by a factor of two, it is virtually identical to profile (III). This alone indicates that the spatial distribution of the trapped molecules in the shallow and deep potential are the same. This in turn implies that the initial kinetic energy of the molecules, at the moment that the trap is switched on, is small relative to the depth of the trapping potentials. The energy distribution (temperature) is therefore mainly determined by the trapping potential, and is about a factor of two different for the shallow and the deep trap.

This conclusion is supported by numerical simulations of the deceleration and trapping process. The inset in figure 2.16 shows the results of these simulations, indicating the number of trapped molecules as a function of their Stark shift and speed, for both trapping geometries. The molecules in the shallow trap potential (II) have a smaller Stark shift and a narrower speed distribution than the molecules trapped in the deep trap potential (III). The simulated speed distribution can be characterized by a temperature, which is on the order of 60 mK and 100 mK for the molecules trapped in the shallow and deep trap potential, respectively.

Chapter 3

Reflection of OH molecules from magnetic mirrors

We have reflected a Stark-decelerated beam of OH molecules under normal incidence from mirrors consisting of permanent magnets. Two different types of magnetic mirrors have been demonstrated. A long-range flat mirror made from a large disc magnet has been used to spatially focus the reflected beam in the longitudinal direction ("bunching"). A short-range curved mirror composed of an array of small cube magnets allows for transverse focusing of the reflected beam.

In the field of cold atoms, permanent magnets have found many uses, and samples of cold atoms have been reflected, guided and trapped by their potentials [107]. As samples of cold atoms are routinely produced with temperatures in the μK range, the requirements on the magnetic field-strengths are rather relaxed. Periodically magnetized recording media, e.g., video or audio tape, have been used to construct curved mirrors for atoms. In the experiments presented here, we have used beams of ground-state OH molecules, slowed down using a Stark decelerator. These decelerated beams still have a kinetic energy corresponding to a temperature of a few hundred mK, and significantly higher field-strengths are therefore required. We have used rare-earth magnets that can possess a remanence of higher than 1 T. The small size and the low cost of these magnets makes them ideally suited to create different types of magnetic mirrors for molecules.

3.1 Experimental setup

In figure 3.1 a schematic view of the essential part of the experimental setup is shown. A detailed description of the molecular beam machine, and particularly of the deceleration of a beam of OH molecules, is given in chapter 2. In the experiments reported in the present chapter, a pulsed beam of OH molecules is decelerated from 390 m/s to a velocity in the 10-20 m/s range. In figure 3.1 only the last six stages of the Stark decelerator are shown. About 10 mm behind the decelerator, the OH molecules pass through the detection zone. Here, molecules are detected via a laser induced fluorescence (LIF) scheme, using excitation via the $Q_1(1)$ transition as described in section 2.3.4.

A typical time-of-flight measurement for a beam of OH molecules passing through the Stark decelerator beam machine is shown in the upper left corner of figure 3.1. The undecelerated part of the OH beam arrives in the detection region about 3 ms after its production in the source chamber. Only OH $(X^2\Pi_{3/2}, v = 0, J = 3/2)$ molecules in the low-field seeking component with the largest Stark shift, e.g. the $M_J\Omega = -9/4$ component, are decelerated. In this particular measurement, these molecules are decelerated to a final velocity of 15 m/s and they arrive in the detection region after 7 ms. The decelerated packet contains approximately 10^5-10^6 OH molecules, has a spatial extent of about 3 mm along the molecular beam axis and is about 4x4 mm^2 in the transverse direction at the exit of the decelerator. The full width at half maximum (FWHM) of the velocity spread in the forward direction is about 7 m/s, corresponding to a longitudinal temperature of 10 mK. In the transverse direction, the FWHM velocity spread is slightly less, about 5 m/s. Only this decelerated packet of OH molecules is relevant for the magnetic reflection experiments presented here.

Shortly behind the detection region, two different magnet assemblies can be mounted on a vacuum feedthrough translator that allows to change the distance
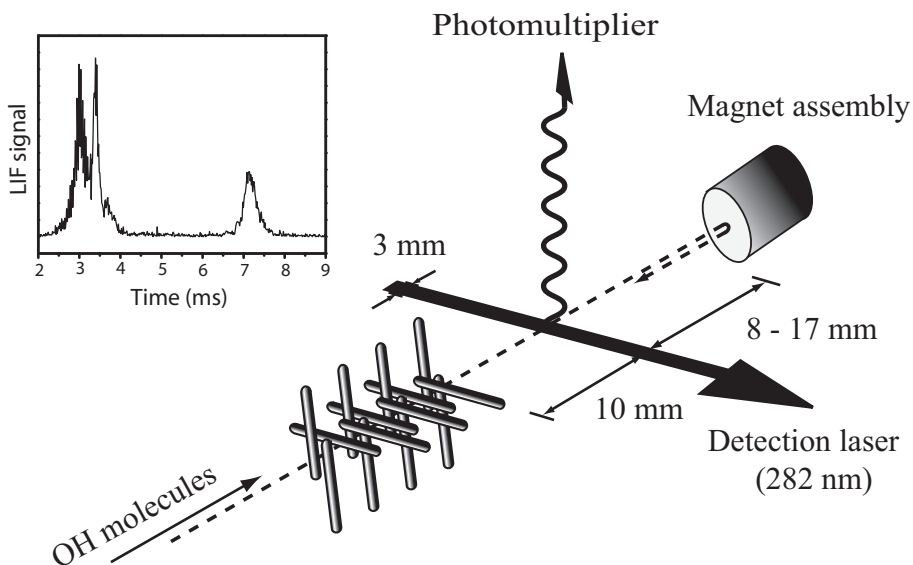
Figure 3.1: A schematic view of the detection zone in the experiment. For clarity, only the last seven electrode pairs of the decelerator are shown. The dashed line indicates the path of the molecular beam. The graph in the upper left corner shows a time-of-flight profile for a beam of ground-state OH molecules decelerated from 390 m/s to 15 m/s. The undecelerated molecules arrive in the detection zone about 3 ms after their production in the source region, whereas the decelerated ones take some 4 ms longer.

of the magnet surface to the detection zone from 0 to 30 mm. Ground state $(X^2\Pi_{3/2}, J = 3/2)$ OH molecules are ideally suited for Stark deceleration and subsequent magnetic reflection because they exhibit both a strong Stark shift and a strong Zeeman shift; Stark deceleration followed by magnetoelectrostatic trapping has first been demonstrated with OH molecules as well [48]. The interaction potential of the ground state OH molecules with both the magnetic field and the electric field is given in chapter 2. Half of the decelerated OH molecules are in the magnetically high-field seeking states and will be attracted to the magnet, i.e., they will crash into the magnet and be lost for the further experiment. The magnetically low-field seeking OH molecules will experience a repulsive force, and after reflection they can pass through the detection region once more. For the $M = +3/2$ state the Zeeman shift is equal to 0.56 cm^{-1}/T. For a magnetic field of 0.5 T this implies that OH molecules with velocities up to a maximum of about 20 m/s can be retro-reflected.

The first magnetic mirror consists of a stack of three disc-shaped nickel
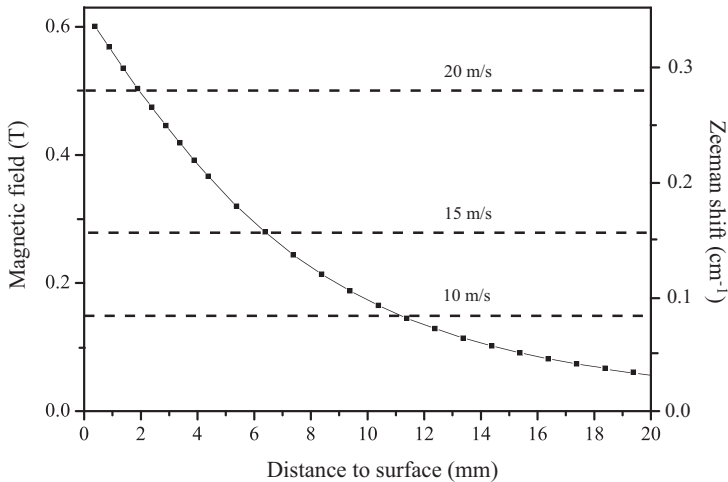
Figure 3.2: The measured magnetic field strength and the corresponding Zeeman shift for decelerated OH ($M = +3/2$) molecules as a function of distance from the surface of the disc magnet. The dashed horizontal lines indicate the field strengths at which OH molecules with velocities of 10, 15 and 20 m/s will be reflected.

coated NdFeB magnets, each with a diameter of 20 mm and a thickness of 6 mm, and is referred to hereafter as the "disc magnet". The remanence of the material used for the magnets is 1.5 T according to the supplier. The measured magnetic field and the corresponding Zeeman shift for the $M = +3/2$ state along the centerline of the disc magnet as a function of distance from the magnet surface is given in figure 3.2. The dependence of the magnet field strength on distance from the surface is rather similar for axes that are parallel to and up to a few mm away from the centerline; the magnetic field strength only starts to drop off significantly near the edges of the magnet. This mirror therefore acts more or less as a flat mirror. It is observed that the magnetic field has a fairly long range, and that even at distances of a few centimeters from the magnet surface there is still an appreciable magnetic field present. The magnetic field at which OH molecules with a velocity of 10, 15 and 20 m/s will be reflected is indicated by the horizontal dashed lines in figure 3.2. It can be seen that OH molecules with a velocity of 20 m/s will penetrate about 9 mm further into the magnetic field than molecules that move with only half that velocity. This leads to bunching, i.e. a longitudinal spatial focusing, of the reflected molecules.

The second magnetic mirror, hereafter referred to as the "magnet array", is a two-dimensional array of 241 nickel coated 1x1x1 mm³ cube NdFeB magnets

48
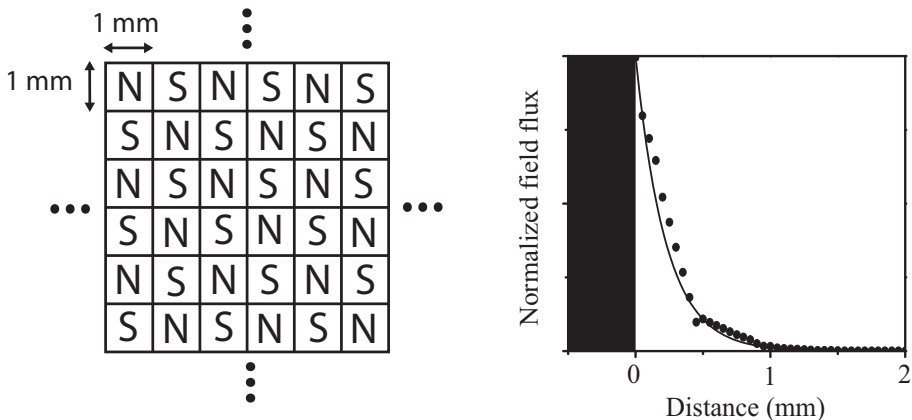
Figure 3.3: Left panel: schematic view of the two-dimensional magnetic array. N and S indicate north and south poles of the individual magnets. Right panel: Magnetic field strength as a function of distance from the surface of the array. The solid curve is the analytical expression (equation 3.1) whereas the dots are the result of a finite element calculation.

arranged on a concave round iron substrate with a diameter of 20 mm and a radius of curvature of 20 mm. The remanence of the material used for the magnets is 1.2 T according to the supplier. The cube magnets are arranged in a checkerboard fashion, with alternating north and south poles in two dimensions, as is schematically depicted in the left panel of figure 3.3.

If the magnetization is varying sinusoidally with a period of a in the x-y plane, then the decay of the magnetic field in z direction can be derived similarly as is done for the one dimensional case [107, 108]. For the two-dimensional case the field strength B will decay as

$$B = B_0 e^{-\sqrt{2}kz} \tag{3.1}$$

where B_0 is the field strength at the surface of the array and $k = 2\pi/a$. For our case of $a = 2$ mm we have a $1/e$ decay distance of slightly more than 0.2 mm. We neglect here the higher harmonics of the alternating magnetization and end effects due to the finite number of magnets [109]. To validate this result we performed a finite element calculation, the result of which is shown in the right panel of figure 3.3 (dots) together with the predicted field strength from equation 3.1 (solid curve). As the magnetic field of this mirror extends only over a short range, the molecules will all be reflected at more or less the same distance from the surface, irrespective of their velocity. It is evident, however, that this magnet array forms a transversely focusing mirror with a focal length of 10 mm; after the addition of the magnet array the curvature of the iron

substrate is not exactly preserved and the focal distance is actually slightly shorter than this.

An analogous electrostatic mirror, constructed with a one-dimensional array of thin electrodes, has been used to retro-reflect a slow beam of ammonia molecules [54]. A one-dimensional array of small permanent magnets has been used for reflection of cold cesium atoms dropped from an optical molasses [109]. By adding a magnetic bias field to the magnet array as we have used it here a two-dimensional array of small traps with large magnetic field gradients can be created [110, 111].

3.2 Results and discussion

The left panel of figure 3.4 shows time-of-flight (TOF) profiles obtained by reflecting OH molecules from the disc magnet. The data shown are an average over 350 measurements. For convenience, we define the time that the electric fields of the decelerator are switched off, e.g. when the decelerated molecules are near the exit of the decelerator, as $t = 0$. The main peak at around 1 ms results from the decelerated packet of OH molecules that passes with a mean velocity of 19 m/s through the detection zone on its way to the magnetic mirror. The reflected packet of molecules returns in the detection zone up to several milliseconds later. The exact arrival time obviously depends on the distance of the magnetic mirror from the detection zone which is varied from 17 via 13 and 10 to 8 mm for curves (a)–(d), respectively. The small peak at around 0.3 ms results from OH molecules that are considerably faster than the decelerated packet, and that will therefore not be reflected. One can see in figure 3.4 that the height of the main peak at around 1 ms is lower when the magnet surface is placed closer to the detection region. This is due to the less efficient detection of the OH molecules as a consequence of the Zeeman broadening of the detection transition, caused by the long-range field of the disc magnet. In addition, the background signal due to laser light scattered from the disc magnet increases when the magnet is brought closer to the detection zone.

Normally, one would expect the peak of the reflected beam in the TOF profile to be considerable broader than that of the incoming beam, given the longer flight time in combination with the relatively large longitudinal velocity spread in the decelerated beam. The TOF profiles clearly show, however, that the reflected peak is even narrower than the incoming one. This is a direct demonstration of longitudinal spatial focusing of the reflected beam, caused by the long-range field of the disc magnet. The faster molecules penetrate deeper into the magnetic field than the slow ones, and therefore have to travel a longer distance. When the distance of the surface of the disc magnet to the detection region is about 10 mm (c), this results in a catching up of the slow and the fast molecules in the detection region, i.e. in a longitudinal spatial focus in the detection region and in the corresponding narrowest peak in the TOF
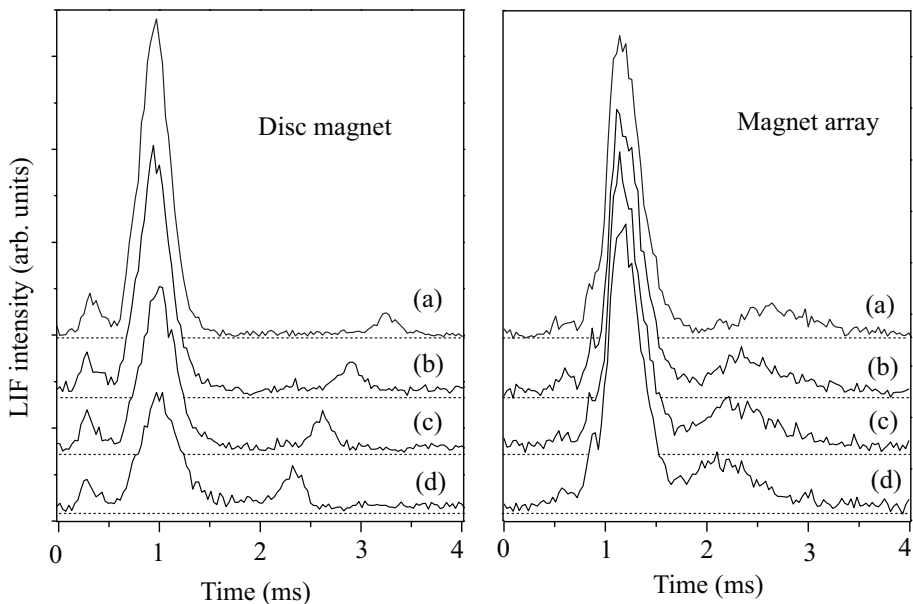
Figure 3.4: Measured time-of-flight profiles for decelerated beams of OH molecules reflected from two different magnetic mirrors. Left panel: OH molecules with a mean velocity of 19 m/s are reflected from the disc magnet. The distance of the surface of the magnet to the detection zone is (a) 17 mm, (b) 13 mm, (c) 10 mm and (d) 8 mm. Right panel: OH molecules with a mean velocity of 15 m/s are reflected from the magnet array. The distance of the surface of the magnet to the detection zone is (a) 13 mm, (b) 11 mm, (c) 10 mm and (d) 8 mm.

distribution. Longitudinal spatial focusing, both in real space (bunching) and in velocity space (longitudinal cooling), of a molecular beam using inhomogeneous electric fields has been discussed and demonstrated before [112].

The right panel of figure 3.4 shows TOF profiles obtained by reflecting OH molecules from the magnet array. The data shown are an average over 660 measurements. Because the strength of the magnetic field is lower than in the case of the disc magnet, the OH molecules are decelerated to a mean velocity of 15 m/s for these experiments. It is seen in figure 3.4 that the signal due to the incoming slow OH beam remains constant even when the surface of the magnet array is rather close to the detection zone; only the stray light level increases due to light scattering from the magnet array. As expected, there is no evidence of longitudinal spatial focusing of the reflected beam, and the peak of the reflected beam in the TOF distribution is considerably broader

than that of the incoming beam. It is interesting to note that for the same distance between the surface of the magnetic mirror and the detection zone, the reflected molecules arrive earlier when reflected from the magnet array than from the disc magnet. This might seem counter-intuitive, as the molecules in this experiment are not only slower to begin with but also approach the surface of the magnet array closer than that of the disc magnet, and therefore have to travel a longer distance. However, with the disc magnet the molecules are gradually decelerated as they approach the magnet and they are accelerated again on their way to the detection region. With the magnet array, on the other hand, the molecules keep a constant speed throughout, with an abrupt change of sign of the velocity vector close to the surface, and are therefore actually earlier back in the detection region. We do see an effect of the transverse spatial focusing of the magnet array. For a distance of the surface of the magnet to the detection region of 8 or 10 mm, the ratio of the area of the reflected peak to the initial peak is about a factor two larger for the magnet array than for the disc magnet. This indicates that the molecules are detected more efficiently when reflected from the magnet array due to the transverse focusing of the packet in the detection region.

To further illustrate the effect of longitudinal spatial focusing for the disc magnet, as well as the lack thereof for the magnet array, we have done three-dimensional trajectory calculations to simulate the reflection experiments. Figure 3.5 shows measured TOF profiles for both magnetic mirrors, together with the corresponding simulated profiles. In the simulation for the disc magnet the measured magnetic field as given in figure 3.2 is taken, whereas for the magnet array the analytical expression of equation 3.1 with $B_0 = 0.3$ T is used. The shape and time of arrival of the reflected peak is reproduced well in the simulated TOF profiles for both magnetic mirrors. On the right hand side of figure 3.5 snap-shots of the longitudinal phase-space distributions of the OH molecules are shown at 0.25 ms time intervals during the reflection process. As the OH molecules approach the surface of the disc magnet, the fast molecules are decelerated more than the slow ones and as a result the velocity distribution narrows down while the position distribution broadens. After turning around the opposite happens and the spatial distribution comes to a focus in the detection region. In the reflection process, the initial phase-space distribution of the decelerated packet is more or less reconstructed at the detection zone, but spatially compressed (and therefore slightly extended in velocity space) and rotated by 180°. The clipping of the phase-space distributions at velocities of about -21 m/s results from the finite height of the magnetic field at the surface; faster molecules have simply not been reflected but have crashed into the surface. The phase-space distributions for the OH molecules that are reflected from the magnet array clearly show that, after an abrupt reversal of the velocity close to the surface, the reflected packet continues to spread out and that no bunching occurs.
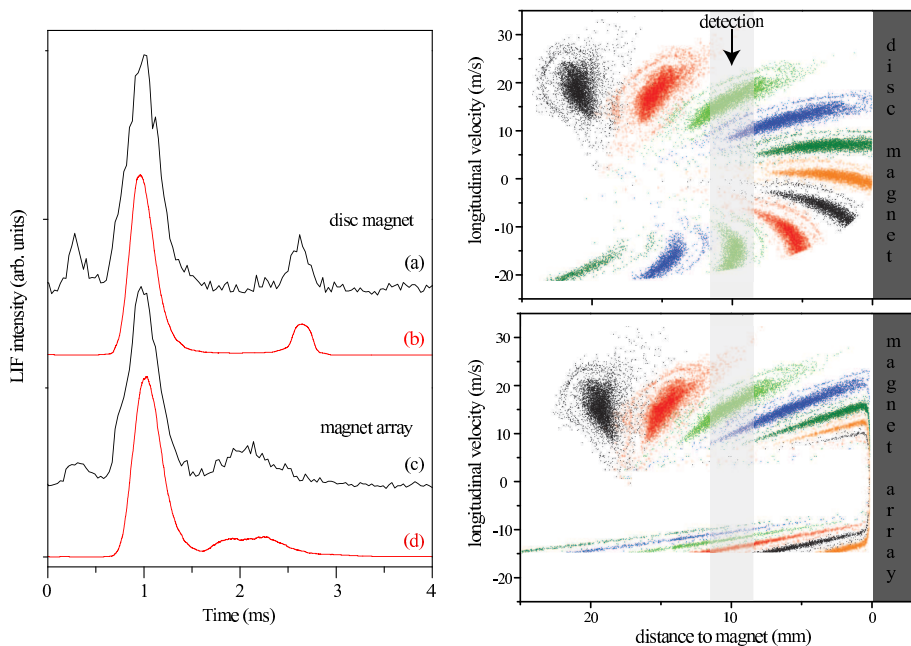
Figure 3.5: Left panel: measured (a,c) and simulated (b,d) TOF profiles for decelerated OH molecules reflected from the two different magnetic mirrors. An OH beam with a mean velocity of 19 m/s (15 m/s) is reflected from the disc magnet (magnet array). The distance of the surface of the magnetic mirror to the detection zone is 10 mm. Right panel: snap-shots of the corresponding simulated longitudinal phase-space distributions at 0.25 ms time intervals. The position of the detection laser is indicated in grey.

3.3 Conclusions

We have demonstrated reflection of slow beams of OH molecules from two different types of magnetic mirrors, composed of permanent magnets. A long-range flat mirror is used for longitudinal spatial focusing of the reflected molecules whereas a short-range curved mirror is used for transverse focusing.

Permanent magnets with typical magnetic field strengths of 1 T can be custom-made in a wide variety of geometries. They are compact and relatively cheap and can be a viable alternative to electromagnets in the manipulation and control of cold molecules. Apart from magnetic mirrors, magnetic guides and magnetic traps can be made from these permanent magnets as well; the group of Jun Ye (JILA, Boulder, CO, USA) has recently demonstrated magnetic trapping of OH molecules using an arrangement of permanent magnets [75] as

is discussed in chapter 7. Even though permanent magnets do not allow for rapid tuning of the magnetic field strength, often the strength of the interaction of molecules with the magnetic field can be tuned by (laser) preparation of the molecules in an appropriate quantum state. For molecules in a $^2\Pi$ electronic state like OH, the magnetic field interaction can even effectively be switched off by transferring the molecules from the $^2\Pi_{3/2}$ to the $^2\Pi_{1/2}$ electronic state. When the transfer of molecules is performed via laser excitation followed by spontaneous fluorescence, this scheme allows for the accumulation of Stark decelerated molecules in an electrostatic trap that is superimposed with the magnetic reflection field, i.e., a more general version of the previously proposed accumulation scheme [74].

Chapter 4

Inelastic collisions using molecular beams with a tunable velocity

Molecular scattering behavior has generally proven difficult to study at low collision energies. We formed a molecular beam of OH radicals with a narrow velocity distribution and a tunable absolute velocity by passing the beam through a Stark decelerator. The transition probabilities for inelastic scattering of the OH radicals with Xe atoms were measured as a function of the collision energy in range of 50 to 400 wavenumber, with an overall energy resolution of about 13 wavenumbers. The behavior of the cross sections for inelastic scattering near the energetic thresholds was accurately measured, and excellent agreement was obtained with cross-sections derived from coupled-channel calculations on *ab initio* computed potential energy surfaces.

4.1 Collisions in crossed beams

The study of collisions between gas-phase atoms and molecules is a well-established method of gathering detailed information about their individual structures and mutual interaction [113]. The level of detail obtained by these studies depends on the quality of preparation of the collision partners before the collision [1, 114] and on how accurately the products are analyzed afterward [115, 116, 117]. In recent years, it has become increasingly possible to control the internal and external degrees of freedom of the scattering partners, allowing the potential energy surfaces that govern the molecular collisions to be probed in ever greater detail. The most detailed information is obtained when crossed molecular beams are used to produce intense jets of molecules with a well-defined velocity, confined to only a few internal quantum states. Further state selection can be achieved by optical preparation of a single quantum state or by purification of the beam with the use of electrostatic or magnetic multipole fields [1]. These methods allow the orientation of the molecules to be controlled before the collision [118, 119] and the orientation of the scattered products can be measured [120].

One of the most important parameters describing a scattering event is the collision energy of the scatterers. However, control over the collision energy has been a difficult experimental task. Since the 1980's, ingenious crossed beam machines have been engineered to vary the crossing angle of the intersecting beams, allowing variation of the collision energy while maintaining particle densities high enough for scattering [121]. It was thereby possible to measure threshold behavior of rotational energy transfer [122, 123], or to tune the collision energy over the reaction barrier for reactive scattering [8, 124]. These methods led to considerable improvement in the control over collision energy at high energies - for example to probe short-range interactions. However, a similar level of control over collisions at low energies, which are sensitive probes for long-range interactions, is generally lacking. The angle of the intersecting beams cannot be varied to arbitrarily small values; and at low collision energies, the energy resolution, which is determined by the velocity spread of both beams, rapidly becomes comparable to the collision energy.

Low-energy collisions of atoms and molecules interrogate the part of the interaction potential energy surface that is relevant for the formation of long-lived complexes. From resonance phenomena in the scattering signal as a function of collision energy, accurate information on the interaction can be extracted [125, 126, 127]. Near the energetic thresholds for inelastic scattering, resonant states can be formed when the colliding complex begins to rotate, leaving the constituents with insufficient translational energy to overcome their van der Waals attraction. Methods to experimentally extract information on these resonances are extremely limited. Thus far, low-energy collisions have only been studied in cryogenic cell environments [128], or in supersonic gas expansions that are specifically designed to maintain a thermal equilibrium

at temperatures as low as 6 K [129]. Recently, reports have appeared on the study of cold inelastic collisions between alkali atoms and dimers in an optically trapped gas [130, 131].

An alternative experimental approach to studying collisions at a low and/or variable energy is to produce molecular beams with a low and/or variable velocity [45]. Mechanical velocity selectors can be used to select molecules with a narrow velocity distribution out of molecular beams [132], but the particle densities and velocities that can be reached are set by the original velocity distribution of the beam. Exquisite control over the velocity of polar molecules in a molecular beam has only been possible since the development of the Stark deceleration technique. In a crossed-beam configuration, Stark decelerators offer the revolutionary capability to study elastic or inelastic and reactive scattering as a function of the continuously variable collision energy, from low to high collision energies, and with a high intrinsic energy resolution. The computer-controlled velocity of the molecular beam allows scanning of the collision energy in an otherwise fixed experimental geometry. The deceleration process is highly quantum-state specific, and the state purity of the bunches of selected molecules that emerge from the decelerator can be close to 100 %. Moreover, the decelerated molecules are all naturally spatially oriented, and steric effects can therefore in principle be studied as well.

Here we report the first molecular beam scattering experiment using a Stark decelerated molecular beam. In a crossed beam set-up, rotationally inelastic scattering between state-selected OH molecules ($X\,^2\Pi_{3/2}, v = 0, J = 3/2, f$, referred to hereafter as $F_1(3/2f)$) and Xe atoms is studied throughout the 0.14 to 1.14 kcal/mol (50 to 400 cm^{-1}) region, with an overall energy resolution of ~ 0.03 kcal/mol (13 cm^{-1}). We chose the OH-rare gas system because, at higher collision energies, rotationally inelastic collisions have been studied for this system in great detail, both experimentally and theoretically; state-to-state cross-sections and the effects of molecular orientation have been determined [133, 134]. The energy range covered in the present study encompassed the energetic thresholds for inelastic scattering down to the lowest rotational levels of OH. The threshold behavior of the inelastic state-to-state cross-sections was accurately measured and was compared with the outcome of coupled-channels calculations on a computed OH-Xe potential energy surface.

4.2   Experiment

A molecular beam of OH molecules in the low-field seeking $F_1(3/2f)$ state was decelerated, guided, or accelerated using a Stark decelerator (figure 4.1). The time-of-flight profile of the molecules that exit the decelerator is shown for a typical setting of the decelerator. The densest part of the OH beam, with an original velocity of 450 m/s, was selected and slowed down to a final velocity of 281 m/s. The decelerated packet of molecules arrived temporally delayed
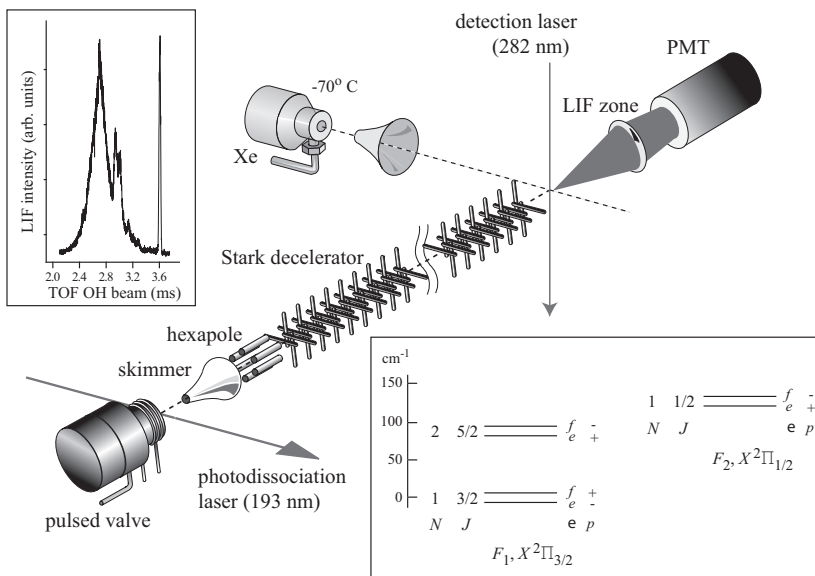
Figure 4.1: Schematic representation of the experimental setup and of the energy-level scheme of the OH molecule. In the present chapter, molecules are decelerated, guided or accelerated to a velocity in the 33 to 700 m/s range. A typical time-of-flight (TOF) profile is shown in the left inset. The selected packet of molecules arrives temporally separated in the scattering region and is scattered with a beam of pure Xe at an angle of 90°, under single-collision conditions. The collision-induced populations in the $F_2(1/2)$, $F_1(3/2)$, and $F_1(5/2)$ rotational levels are probed before and after the collisions in a saturated laser induced fluorescence (LIF) scheme. In the energy-level scheme shown in the right inset, the splitting between both parity components of each rotational level is largely exaggerated for reasons of clarity.

in the field-free interaction region and was scattered with a beam of pure Xe under an angle of 90°. In the experiments, the velocity of the OH molecules was varied from 33 to 700 m/s; the contribution of the OH molecules to the center-of-mass (CM) collision energy (E_{coll}) was thereby varied from less than 1 to $\sim$ 310 cm^{-1}. The contribution of the width of the OH velocity distribution to the overall energy resolution was very small. The maximum rotational state purity of the packet of OH $F_1(3/2f)$ molecules before the collision was measured to be $\geq$ 99.7 %. Contamination of the inelastic state-to-state scattering data by initial populations in different quantum states was negligible.

The xenon beam was produced by expansion of Xe at 2.5-atm backing pressure from a cooled pulsed valve ($-70°$C), resulting in a beam with a velocity of $\sim$ 300 m/s. The exact velocity of the Xe atoms depends on the detailed
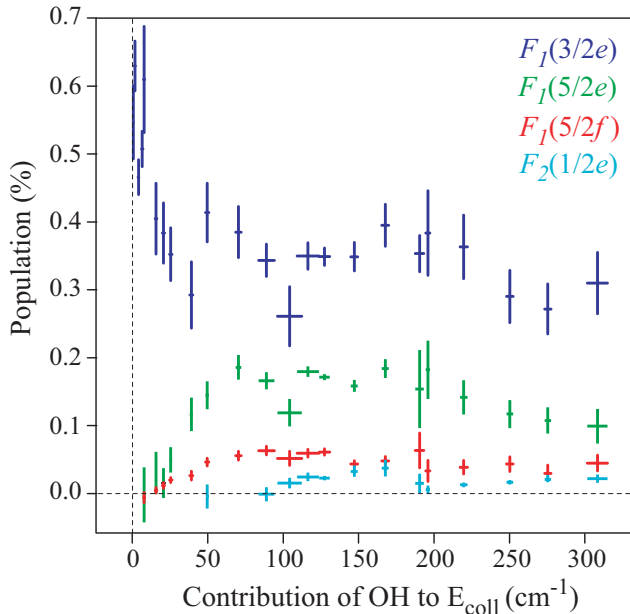
Figure 4.2: Probabilities for inelastic scattering of OH $F_1(3/2f)$ molecules in collisions with Xe atoms to the $F_1(3/2e)$, $F_1(5/2e)$, $F_1(5/2f)$, and the $F_2(1/2e)$ levels as a function of $\frac{1}{2}(\frac{m_{OH}m_{Xe}}{m_{OH}+m_{Xe}})v_{OH}^2$ - i.e., as a function of the contribution of OH to the CM collision energy (where m_{OH} and m_{Xe} are the mass of OH and Xe, respectively, and v_{OH} is the velocity of the OH molecules in the laboratory frame). The horizontal error bars represent the uncertainty in collision energy that results from the velocity spread of the OH beam, which is different for every setting of the decelerator. The vertical error bars represent the statistical spread of the data as obtained from repeated runs of the experiment.

settings of the pulsed valve as well as the timing of the collision event within the Xe gas pulse, and these settings were kept fixed during the measurements. Although the exact velocity of the Xe atoms was not measured, the constant contribution of the Xe atoms to the CM collision energy of ~ 60 cm^{-1} was sufficiently low that the total CM collision energy could be tuned over the energetic thresholds for scattering into both parity components of the $F_1(5/2)$ level (84 cm^{-1} excitation energy) and the $F_2(1/2)$ level (121 cm^{-1} excitation energy). The approximately 10 % velocity spread in the Xe beam was by far the dominant contribution to the overall energy resolution in this experiment.

Saturated laser induced fluorescence with tunable pulsed lasers, as discussed in section 2.3.4, was used to detect the OH molecules. For each setting of the

OH velocity, the populations in the $F_1(3/2e)$, $F_1(3/2f)$, $F_1(5/2e)$, $F_1(5/2f)$ and $F_2(1/2e)$ levels were measured, both with and without collision of the Xe beam with the OH beam. The decrease of population in the $F_1(3/2f)$ level due to scattering with the Xe atoms was about 1 %, indicating that single collision conditions were fulfilled in the experiment. The signals associated with the scattering products were normalized by the signal of the incoming OH $F_1(3/2f)$ molecular packet. Different excitation rates for the different branches of the optical transitions used to probe the different levels were taken into account to relate signal intensities to populations. Thus transition probabilities for inelastic scattering to the $F_1(3/2e)$, $F_1(5/2e)$, $F_1(5/2f)$, and $F_2(1/2e)$ levels were obtained as a function of the OH contribution to the CM collision energy (figure 4.2). Collisions populating the $F_1(3/2e)$ level were most likely. Within the $F_1(5/2)$ level, collisions populating the lower Λ-doublet component of e parity were favored, consistent with findings of other $^2\Pi$-rare gas systems [133, 134]. For the $F_1(3/2e)$ and the $F_1(5/2e/f)$ levels, the transition probabilities were almost constant at higher collision energies. Close to the $F_1(5/2)$ energetic threshold, collisions populating either one of the parity components of this level became less probable, and the transition probabilities for these levels dropped sharply. The only inelastic channel that was exo-energetic was scattering to the $F_1(3/2e)$ level, and its transition probability showed an increase at low collision energies. Excitation to the $F_2(1/2)$ level required a spin-orbit changing collision, for which the cross-sections are generally lower than for a spin-orbit-conserving collision. The transition probability for this channel also showed a clear threshold behavior.

4.3   Comparison to theory

The theoretical framework to compute cross-sections for inelastic collisions of $^2\Pi$-state molecules such as OH with ^1S-state atoms such as Xe is well established [135]. The electronic degeneracy of the Π state is lifted upon the approach of the atom, and two potential energy surfaces are required to describe the system. Contour plots of the potentials are shown in figure 4.3. All theoretical calculations on those potentials and the cross-sections were performed by Gerrit Groenenboom from the Radboud University in Nijmegen, The Netherlands. The details of those calculations, that go beyond the scope of this thesis, were published in a joint experimental and theoretical publication [10].

Relating the measured energy-dependent transition probabilities (figure 4.2) to the calculated inelastic cross-sections (figure 4.3) requires detailed information on the relative velocity of the scatterers, the actual time interval during which scattering events are probed, and the detection probability of the scattered products [122]. Systematic effects, such as the collision energy-dependent time interval for scattering and intensity and velocity of the incoming OH beam, cancel out when the relative inelastic transition probabilities are extracted from
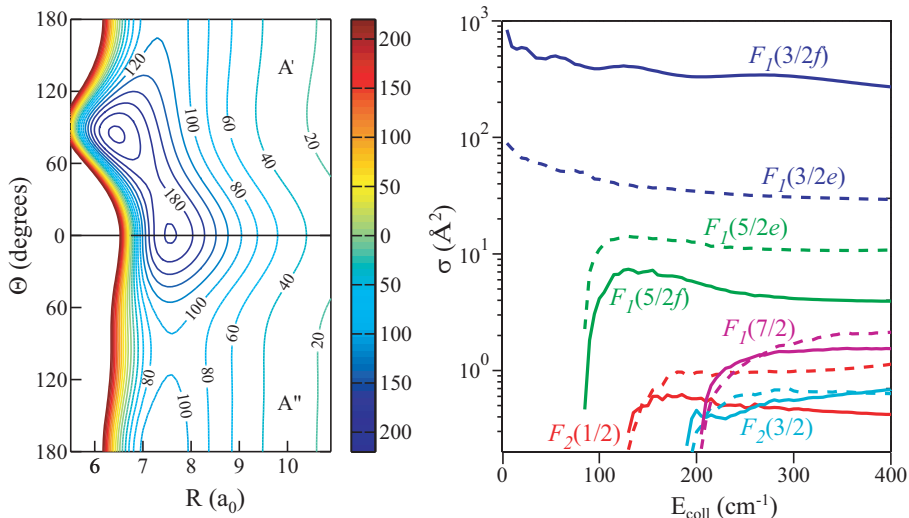
Figure 4.3: (A) Contour plots of the A' (upper) and A'' (lower) potential surfaces in cm^{-1}. (B) Computed cross sections for the first 10 channels. The solid and dashed lines correspond to channels of f and e spectroscopic labelling, respectively. The $F_1(3/2f)$ channel is the elastic channel.

the measured absolute transition probabilities given in figure 4.2. If we assume an identical detection probability of the scattered products for the different inelastic channels for a given collision energy*, the relative inelastic transition probabilities directly yield the relative cross-sections for inelastic scattering (figure 4.4). The horizontal axis is given an offset compared to the one in figure 4.2 to include the contribution of the Xe atoms to E_{coll}. The positions of the energetic thresholds are known with spectroscopic accuracy, and we obtained the best agreement when a velocity of the Xe atoms of 320 m/s was taken. The theoretical inelastic cross-sections (figure 4.3) were first convoluted with the experimental energy resolution, and we used the resultant values to calculate the relative cross-sections (solid curves in figure 4.4). Excellent agreement between theory and experiment was obtained throughout the range of collision energies probed. The ratio of scattering into the different channels, and, in par-

---

*The validity of this assumption is verified by analytically modelling the detection probability in the limiting cases of forward, backward and isotropic scattering. The difference is found to be within the error bars of our data.

ticular, the shape of the inelastic cross-sections around threshold is perfectly reproduced.
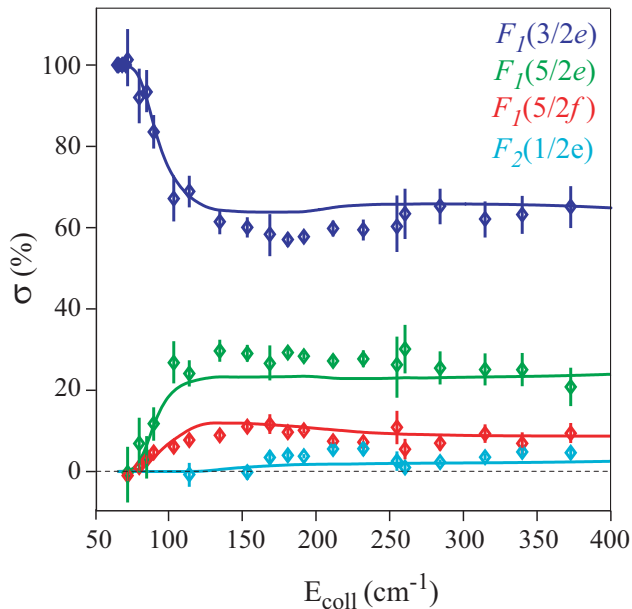
Figure 4.4: Comparison of the collision energy dependence of the measured (data points with error bars) and calculated (solid curves) relative cross-sections - i.e., the fractional scattering of OH molecules into one of the $F_1(3/2e)$, $F_1(5/2e)$, $F_1(5/2f)$, or $F_2(1/2e)$ channels.

4.4 Conclusions

Our measurements provide a very sensitive probe for the theoretical potential energy surfaces, from which a detailed understanding of the collision dynamics can be obtained. A next step will be to use two crossed velocity-tunable molecular beams or to collide the velocity-tunable beam with a stationary (i.e., trapped) sample of cold or ultracold atoms or molecules. In such systems, quantum state selected atom-molecule and molecule-molecule collisions can be studied, down to collision energies below 1 cm^{-1}, with a fraction of a wavenumber energy resolution. An experimental setup consisting of two Stark decelerators of 300 stages length each is currently under construction at the Fritz-Haber-Institute in Berlin [11].

Chapter 5

Optical pumping by blackbody radiation

Optical pumping by blackbody radiation is a feature shared by all polar molecules and fundamentally limits the time that these molecules can be kept in a single quantum state in a trap. To demonstrate and quantify this, we have monitored the optical pumping of electrostatically trapped OH and OD radicals by room-temperature blackbody radiation. Transfer of these molecules to rotationally excited states by blackbody radiation at 295 K limits the $1/e$ trapping time for OH and OD in the $X^2\Pi_{3/2}, v = 0, J = 3/2(f)$ state to 2.8 s and 7.1 s, respectively.

5.1 Blackbody radiation

In his 1917 paper Einstein showed [136] that even in the absence of collisions the velocity distribution of a molecular gas takes on a Maxwellian distribution due to the momentum transfer that takes place in the absorption and emission of blackbody radiation. The absorbed and emitted photons optically pump the rotational and vibrational transitions, resulting in thermal distributions over the available states. The rotational temperature of the CN molecule in interstellar space [137], for example, is the result of optical pumping by the cosmic microwave background-radiation [138].

The influence of blackbody radiation on atoms and molecules is in general small and it is rare that it can be observed directly in laboratory experiments. However, in a number of cases the interaction with blackbody radiation is experimentally observable and important. The first dynamical effects of blackbody radiation on the population of atomic levels were noticed when studying the lifetime of highly excited Rydberg states in atoms [139]. Atoms in these states can have dipole moments of thousands of Debye, and have sufficient spectral overlap with the spectrum of room-temperature blackbody radiation. The excitation (and ionization) rates can be on the order of 1000 s^{-1}, implying that the effect can already be observed on a μs timescale.

The excitation rates in ground state atoms and molecules are generally much lower, and therefore require a longer interaction time to be observed. Only with the development of ion traps, together with a sufficient reduction of collisional energy exchange (i.e. a good vacuum at room temperature), could the photodissociation of molecular ions and clusters by blackbody radiation be directly observed [140, 141]. Ions in storage rings are also trapped long enough for the interaction with blackbody radiation to be noticeable [142].

The effect of blackbody radiation on neutral molecules in a trap has until now been left experimentally unexplored, partly because the conditions to observe the effect were not met, and partly because the importance of this effect was not always realized. Polar molecules generally have strong vibrational and/or rotational transitions in the infrared region of the spectrum. As a result they can relatively easily be optically pumped by room-temperature blackbody radiation, and this fundamentally limits the time that these molecules can be kept in a single quantum state in room temperature traps. This has important implications for cooling schemes which aim at increasing the phase-space density of trapped neutral polar molecules.

This chapter describes the experimental quantification of trap loss due to blackbody radiation for neutral polar molecules stored in a room-temperature trap, using the OH radical as a model system. Cold packets of OH radicals are produced using the Stark deceleration and trapping technique as described in chapter 2.

5.2 Experiment

A natural approach to experimentally study the effect of blackbody radiation on the trapped molecules would be to vary the temperature of the trapping apparatus, thereby changing both the spectral distribution and the intensity of the blackbody radiation. A disadvantage of this is that normally a change of the temperature will also influence the vacuum conditions, changing the collision rate with the residual gas. The alternative approach we have taken is to compare the room-temperature trapping of two isotopic variants of the same molecule. Under the assumption that these isotopomers have the same collisional properties, the trap losses due to blackbody radiation and collisions with background gas can be disentangled.

The molecules we have compared are the OH and OD radical. There is sufficient intensity in the low-energy side of the blackbody radiation spectrum that these molecules can be rotationally excited; the vibrational energy splitting is so large that vibrational excitation is negligible. The energies of the relevant rotational states of OH and OD in the $X^2\Pi$-state are depicted in figure 5.1. Each rotational level is split into two Λ-doublet components with opposite parity, denoted by f and e. In an electric field these components are mixed. In the electric field, each J-state is split into $(2J+1)$ $M_J\Omega$ components. The f component in zero-field corresponds with $(2J+1)/2$ low-field seeking components in an electric field; the e component corresponds with $(2J+1)/2$ high-field seeking components.

Blackbody radiation can excite transitions with $\Delta M_J = \pm 1, 0$. Molecules trapped in low-field seeking states can be pumped to high-field seeking states, leading to trap loss. Because the rotational constant B is almost a factor of two larger for OH than for OD, the intensity of the room-temperature blackbody radiation is much higher at the excitation energy of the first rotational excitation for OH molecules than it is for OD molecules. The most important transition rates due to the blackbody radiation connecting the f-components of the lowest rotational levels are indicated next to the arrows in figure 5.1. The difference in the excitation rates leads us to expect significantly shorter trapping times for OH than for OD radicals.

The production, deceleration and trapping of OH has already been described in chapter 2. In these experiments the OD radical, which is predicted to have interesting collisional properties [143], has been trapped for the first time. Due to their similar mass and dipole moment OH and OD are equally well decelerated and trapped. The trapped molecules, probed by laser-induced-fluorescence directly after switching off the trapping voltages, are initially exclusively in the $M_J\,\Omega = -9/4$ component of the $3/2(f)$ state.

We have measured, for OH and OD, the population trapped in the $3/2(f)$ state, up to a trapping time of 15 seconds. The results are shown in the upper part of figure 5.2. The OD molecules remain, as expected, approximately a factor of two longer in the $3/2(f)$ state than the OH molecules (3.6 s vs.
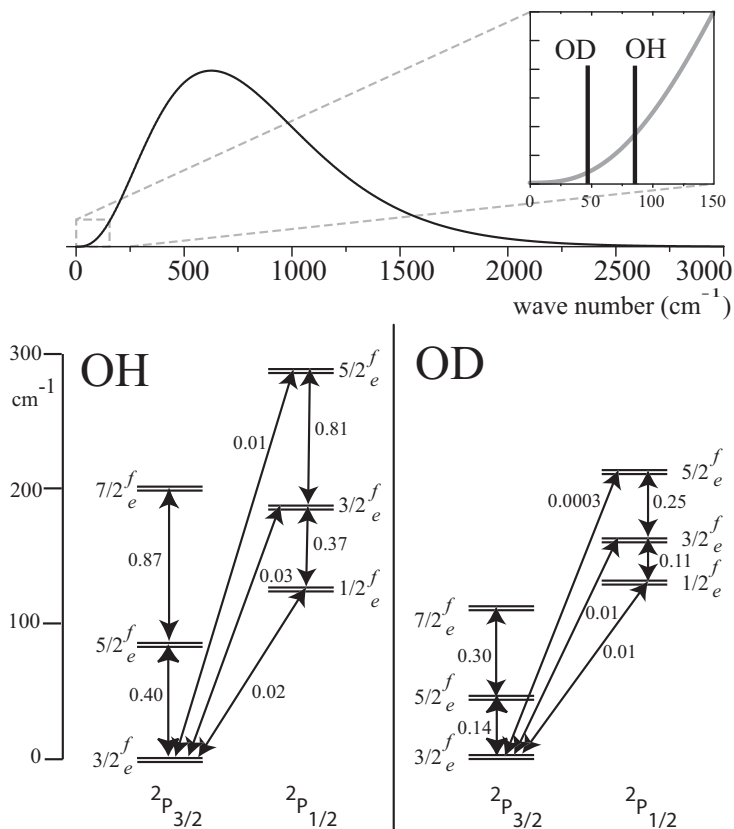
Figure 5.1: In the upper part, the room-temperature spectrum of blackbody radiation is shown. The relevant region for rotational excitation of OH and OD radicals is shown enlarged, with sticks indicating the lowest rotational excitation frequency. In the lower part the relevant rotational levels of OH and OD are depicted. Each rotational level is split into two Λ-doublet components with opposite parity, denoted by f and e. The size of the splitting is exaggerated for clarity. The most relevant transition rates (in s^{-1}) due to blackbody radiation connecting the f-components of rotational levels are indicated next to the arrows.

2.0 s, respectively). To interpret the data we have used a rate equation model, describing the time evolution of the population in the rotational states. The curves in figure 5.2 show the outcome of this model. Molecules can be pumped from the $3/2(f)$ state to the $5/2(f)$ state, in which they can remain trapped. The time-evolution of the $5/2(f)$ population follows from the rate-equation model. The results of the measurement of the population in this state are

shown in the lower part of figure 5.2. About 5 % of the original OD population accumulates in the $5/2(f)$ state after 3 seconds of trapping. For OH the maximum in the $5/2(f)$ population occurs after 1 second of trapping. From the $5/2(f)$ state the molecules can be pumped to other rotational states again, spontaneously decay back to the $3/2(f)$ state or be lost due to collisions with the background gas.
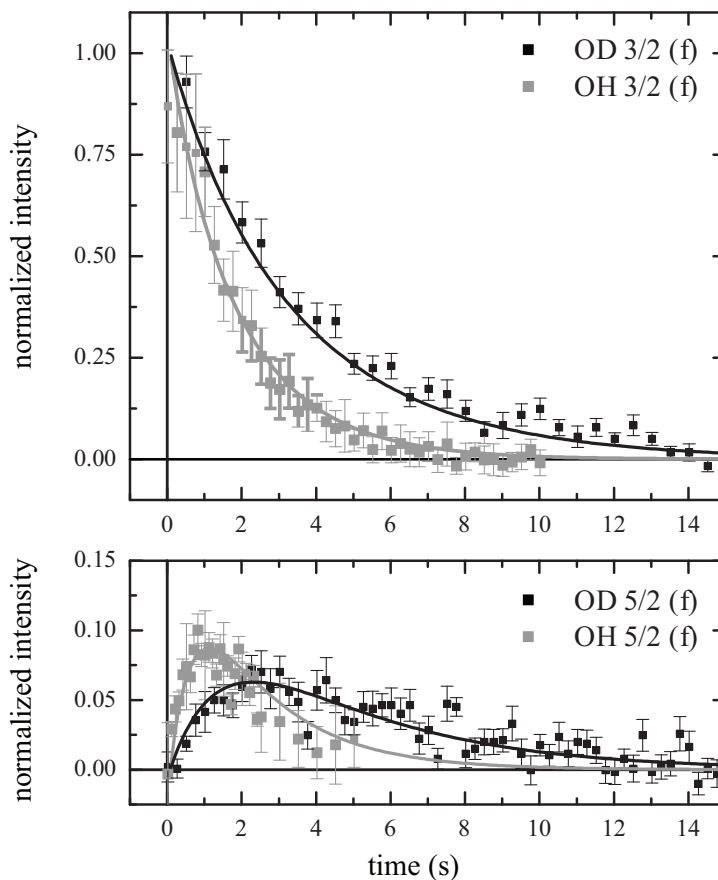
Figure 5.2: The population of electrostatically trapped OH and OD radicals in the $3/2(f)$ and $5/2(f)$ levels as a function of time. The squares are the measured data - grey for OH, black for OD. The curves are the outcome of the rate equation model using a constant background gas collision rate of $0.17\ \mathrm{s}^{-1}$.

For the model, the transition strengths of all allowed transitions between the M_J-components of the rotational states (for both Ω manifolds, up to $J = 7/2$) in OH and OD are calculated. The energy differences caused by hyperfine

effects, the Stark shift of the levels in the electric field of the trap and the Λ-doubling itself are so small compared to the rotational spacing that these are neglected in the calculation of the transition rates. Using the calculated transition strengths and the spectrum of the blackbody radiation at 295 K the transition rates due to the blackbody radiation are obtained, as shown in figure 5.1. Because not all M_J-components have an equal Stark shift the different trapping depths for these states were taken into account. Molecules excited to the $J \geq 7/2$ states are considered lost from the trap. Stimulated emission was also included. Loss due to collisions with residual background gas, assumed to be independent of the rotational level, is taken into account by a constant loss rate. We find best agreement[*] between the model and the data using a background-gas loss rate of 0.17 s^{-1}. To verify whether this loss rate can be explained by collisions with a xenon background gas we have used the recently calculated cross-section for Xe-OH collisions (chapter 4, [10]), taken to be identical for OH and OD. For a room temperature gas of xenon atoms colliding with trapped OH molecules the average collision energy is 30 cm^{-1}, leading to an elastic cross section of 500 ± 50 $\mathring{A}^2$; rotational excitation of trapped OH and OD by the xenon atoms can safely be neglected. Because the trap depth is only about 1 cm^{-1} almost every collision will lead to trap loss. Using a partial xenon pressure of $5 \cdot 10^{-9}$ mbar we find a collision rate of 0.14 s^{-1}, which is consistent with the rate found from the comparison of the model with the data.

Table 5.1: Pumping rates due to blackbody radiation at two different temperatures, out of the specified initial state, for a number of polar molecules.

System	Initial state	Pumping rate (s^{-1})	
		295 K	77 K
OH/OD	$X^2\Pi_{3/2}, J = \frac{3}{2}$	0.49/0.16	0.058/0.027
NH/ND	$a^1\Delta, J = 2$	0.36/0.12	0.042/0.021
NH/ND	$X^3\Sigma^-, N = 0, J = 1$	0.12/0.036	0.025/0.0083
NH$_3$/ND$_3$	$\tilde{X}^1A_1', J = 1, |K| = 1$	0.23/0.14	0.019/0.0063
SO	$X^3\Sigma^-, N = 0, J = 1$	0.01	$< 10^{-3}$
^{6}LiH/^{6}LiD	$X^1\Sigma^+, J = 1$	1.64/0.81	0.31/0.11
CaH/CaD	$X^2\Sigma^+, N = 0, J = \frac{1}{2}$	0.048/0.063	$0.0032/< 10^{-3}$
RbCs	$X^1\Sigma^+, J = 0$	$< 10^{-3}$	$< 10^{-3}$
KRb	$X^1\Sigma^+, J = 0$	$< 10^{-3}$	$< 10^{-3}$
CO	$a^3\Pi_{1,2}, J = 1, 2$	0.014/0.014	$< 10^{-3}/ < 10^{-3}$

We have calculated the blackbody pumping rates for a number of other

---

[*]A better fit can be obtained by using a time-dependent background gas loss rate $r(1 + ae^{-t/\tau})$, with $r = 0.13$ s^{-1}, $a = 1.0$ and $\tau = 1.0$ s, to account for the pressure decrease following the injection of gas at the beginning of the experimental cycle.

polar molecules as well[*]. These molecules are well suited for trapping, using the various currently available techniques [20]. For the selected molecules the blackbody pumping rate out of the specified initial quantum state is compared, for two different temperatures, in table 5.1. The initial state is in most cases the electronic, vibrational and rotational ground state. The rate for OH is slightly larger than the sum of the rates indicated in figure 5.1 due to the effect of hyperfine structure that was included in these calculations.

The room-temperature pumping rate for many of the listed molecules is comparable to that of OH and OD. LiH, with its favorable Stark-effect to mass ratio and the existence of 4 isotopomers often considered an ideal candidate molecule [144, 145], is especially sensitive to blackbody radiation: even at 77 K it can only be trapped for a few seconds. At 4 K the rates for all molecules are smaller than 10^{-3} s^{-1}. Depending on the molecule the pumping rate is either dominated by rotational transitions (OH/OD,NH/ND,LiH/LiD), by vibrational transitions (CO,RbCs,KRb) or by a combination of both. CO, RbCs and KRb have very small blackbody pumping rates.

5.3 Conclusions

In this chapter an experimental study of trap loss of neutral polar molecules due to room-temperature blackbody radiation, using the OH molecule as a model system was discussed. By comparing the trapping times of OH and OD molecules in an electrostatic quadrupole trap, the individual contribution of blackbody radiation and collisions with background gas could be quantified. Loss due to blackbody radiation is a major limitation for the room-temperature trapping of OH and OD radicals. If the vacuum conditions were improved such that losses due to collisions with background gas were completely removed, the $1/e$ trapping time would increase to 7.1 s for OD and 2.8 s for OH. The trapped molecules will have to be shielded from thermal radiation if longer trapping times are required. We have shown that these limitations are shared by a large class of polar molecules, which has profound consequences for the implementation of further cooling schemes.

---

[*]These calculations have been performed by Boris Sartakov

Chapter 6

The radiative lifetime of metastable CO ($a^3\Pi, v = 0$)

We present a combined experimental and theoretical study on the radiative lifetime of CO in the $a^3\Pi_{1,2}, v = 0$ state. CO molecules in a beam are prepared in selected rotational levels of this metastable state, Stark-decelerated and electrostatically trapped. From the phosphorescence decay in the trap, the radiative lifetime is measured to be 2.63 ± 0.03 ms for the $a^3\Pi_1, v = 0, J = 1$ level. From spin-orbit coupling between the $a^3\Pi$ and the $A^1\Pi$ state a 20% longer radiative lifetime of 3.16 ms is calculated for this level. It is concluded that coupling to other $^1\Pi$ states contributes to the observed phosphorescence rate of metastable CO.

6.1 The radiative lifetime of metastable CO

Triggered by the observation of CO in the upper atmosphere of Mars with a UV spectrometer on board the Mariner 6 spacecraft in 1969 [146], researchers started studying the UV bands of CO in increasing detail. In particular, the $a^3\Pi \leftarrow X^1\Sigma^+$ transition between the ground state and the lowest electronically excited state of CO, the so-called Cameron bands, became the subject of theoretical as well as experimental interest. From the appearance of the spectrum it was concluded that the intensity in this spin-forbidden transition mainly originates from spin-orbit mixing of the $a^3\Pi$ state with a $^1\Pi$ state; a detailed analysis revealed that mixing of $^1\Sigma$ states with the $a^3\Pi$ state contributes less than 1 % to the total intensity [147]. Using perturbation theory and taking only the interaction with the $A^1\Pi$ state into account, James calculated the radiative lifetimes for various ro-vibrational levels in the $a^3\Pi$ state [148]. These lifetimes are strongly J-dependent, but the ratio of the lifetimes of different J-levels is known with spectroscopic accuracy. The $J = 1$ level in the $a^3\Pi_1, v = 0$ manifold, from now on indicated as the $(\Omega,v,J)=(1,0,1)$ level, has the shortest lifetime, calculated by James as 2.93 ms; the (2,0,2) level, for instance, lives 54.66 times longer.

An accurate experimental value for the radiative lifetime of ro-vibrational levels of metastable CO is a benchmark for theoretical calculations on spin-orbit mixing of electronically excited states as well as on transition dipole moments. It has proved to be difficult, however, to experimentally determine the lifetime of any of the levels of the $a^3\Pi$ state of CO accurately [149, 150, 151, 152]. These lifetimes can either be extracted from absorption measurements on the Cameron bands or, more directly, from measurements of the phosphorescence decay. For absorption measurements, experimental parameters like the line-integrated number density of ground-state CO molecules in a certain ro-vibrational level, together with the absorption line-shape and the spectral profile of the light source have to be accurately known. More problematic is that the Franck-Condon factors for the vibrational bands of this transition also have to be known to be able to deduce a radiative lifetime. For phosphorescence decay measurements, on the other hand, the ro-vibrational state distribution of the metastable molecules needs to be known, and, on the timescale of the phosphorescence, collisions need to be avoided. To achieve this, laser excitation of CO to single ro-vibrational levels of the metastable state in the collision-free environment of a molecular beam has been used [32, 153, 154]. An intrinsic problem in these molecular beam experiments is, however, that the molecules move with a high speed, typically limiting the time during which the phosphorescence can be detected to a fraction of a millisecond.

Stark deceleration of a beam of polar molecules followed by electrostatic trapping enables the observation of state-selected molecules for several seconds. Recently, the radiative lifetime of vibrationally excited OH radicals was determined by recording the temporal decay of their population in the trap [33]. Here

we report on the Stark deceleration and electrostatic trapping of metastable CO molecules that are laser prepared in either the (1,0,1) or in the (2,0,2) level. The radiative lifetimes are measured by monitoring the phosphorescence decay of the trapped molecules. Calculations to rationalize the observed lifetimes are presented.

6.2 Experiment and results

Stark deceleration of metastable CO molecules has been described in detail before [44]. In the present experiment, we use the Stark decelerator as described in chapter 2 to load the metastable CO molecules in the electrostatic trap that is discussed in that chapter as well. The experimental setup is schematically shown in figure 6.1. A pulsed beam of CO molecules with a mean velocity of 320 m/s is produced by expanding a mixture of 20% CO in Xe from a cooled pulsed valve ($T = 203$ K). A packet of CO molecules in the upper (low-field seeking) Λ-doublet component of the (1,0,1) or (2,0,2) level in the metastable $a^3\Pi$ state is prepared by direct laser excitation from the $X^1\Sigma^+, v = 0$ ground state. After passing through a skimmer, the packet of molecules is slowed down in the Stark decelerator and subsequently loaded and confined in the electrostatic quadrupole trap. When in the (1,0,1) level, about 10^5 CO molecules are trapped at a density of 10^8 cm^{-3} and at a temperature of around 20 mK; in the (2,0,2) level an order of magnitude less molecules are trapped at a somewhat higher temperature.

The ultraviolet phosphorescence back to the electronic ground state that escapes through a hole in one of the trap electrodes is imaged with a lens onto a photomultiplier tube (PMT). In the upper part of figure 6.2 a semilogarithmic plot of the phosphorescence signal is shown as a function of time. The same plot was shown before on a linear scale in figure 2.12. The CO molecules are prepared in the (1,0,1) state at $t = 0$ ms, and the strong phosphorescence peak around 4-5 ms results from molecules that pass through the trap with (more or less) the initial beam velocity. At 9.3 ms, the decelerated packet of molecules arrives in the trap center and the trap is switched on. After some initial oscillations, caused by the collective motion of the molecules in the trap, an exponentially decaying phosphorescence signal is observed. This signal is shown on a linear scale in panel (b) of figure 6.2. A weighted least-squares single exponential fit to this data in the time-interval from 13 to 38 ms gives a decay time of 2.63 ± 0.03 ms, where the error is an estimate accounting for the systematic effect of the initial oscillations. The phosphorescence of the trapped molecules is measured in the presence of the trapping fields, i.e. in an electric field ranging from zero to 10 kV/cm. Under these conditions the opposite parity states of the Λ-doublet are mixed.

For the measurement of the phosphorescence decay of CO molecules in the (2,0,2) level, shown in panel (c) of figure 6.2, the repetition frequency of the
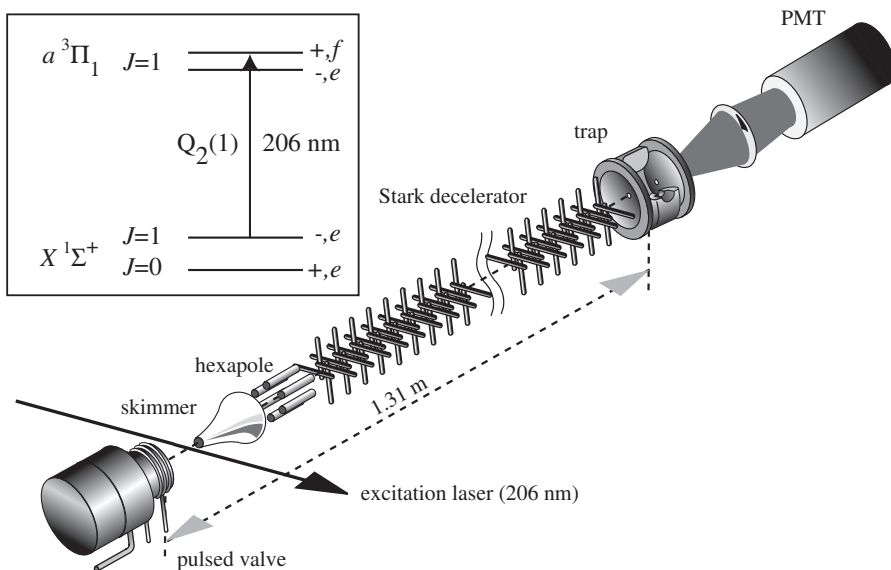
Figure 6.1: Scheme of the experimental setup. A pulsed beam of CO molecules, laser prepared in either the (1,0,1) level (excitation scheme given in the inset) or the (2,0,2) level, is slowed down in the Stark decelerator and stored in an electrostatic trap. The phosphorescence to the electronic ground state is measured by a photomultiplier tube (PMT).

molecular beam experiment is reduced from the normally used 10 Hz to 2 Hz to allow for a ~ 500 ms observation time. To avoid detection of stray-light from the excitation laser, that keeps on running at 10 Hz, no phosphorescence signal is recorded during a 6 ms interval around the times that this laser is fired. A single exponential fit to the data in the 50 to 450 ms interval yields a decay time of 140 ± 4 ms.

Apart from the phosphorescence to the ground state, optical pumping by blackbody radiation and collisions with background gas can lead to a decay of the signal of trapped molecules; at the present densities, collisions between trapped molecules do not play a role. Optical pumping due to room temperature blackbody radiation is calculated to proceed at a rate of around 0.014 s^{-1} for CO in the $a^3\Pi, v = 0$ state (chapter 5, [43]). The contribution of optical pumping to the overall trap loss rate can therefore safely be neglected. The loss rate due to background collisions was measured to be 0.17 s^{-1} for trapped ground-state OH and OD radicals in this apparatus. As these measurements were done under otherwise identical conditions, we assume the same collisional trap loss rate for metastable CO. For CO molecules in the (1,0,1) level the loss due to collisions can then also be neglected; for molecules in the (2,0,2) level
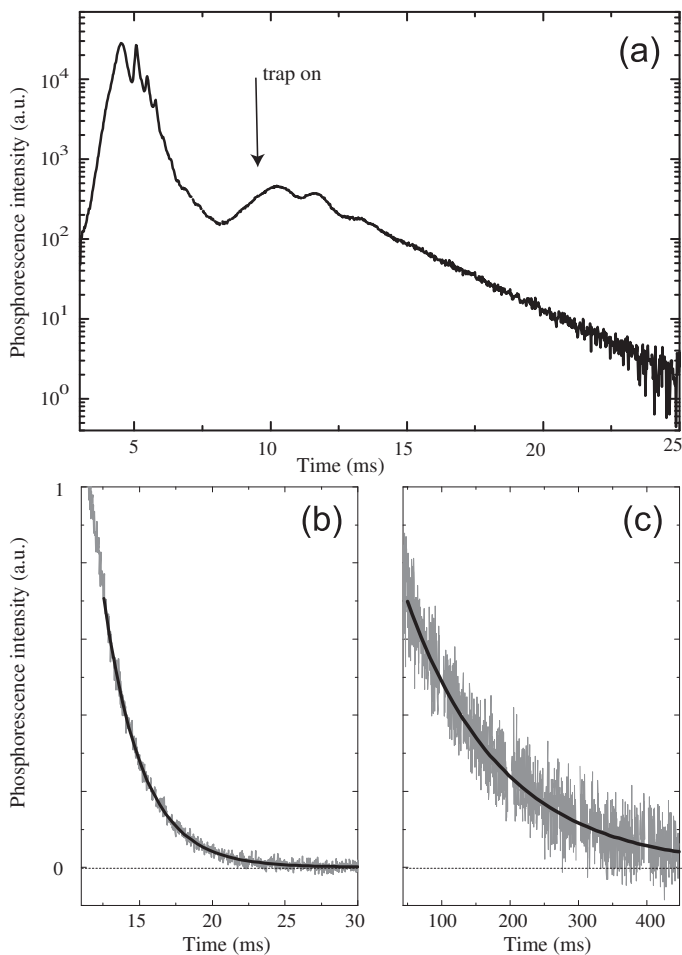
Figure 6.2: Semilogarithmic plot of the phosphorescence intensity from the trap region as a function of time after production of CO molecules in the (1,0,1) level in the source chamber (a). The time at which the trap is switched on is indicated by an arrow. Phosphorescence decay curves are shown on a linear scale for CO molecules in the (1,0,1) level (b) and in the (2,0,2) level (c). The solid lines are the results of a weighted least-square fit to a single exponentially decaying curve.

collisions slightly contribute to the observed trap loss rate. After correction for this, a radiative lifetime for CO molecules in the (1,0,1) level of 2.63 ± 0.03 ms is found, whereas the radiative lifetime for molecules in the (2,0,2) level is determined as 143 ± 4 ms. The ratio of these lifetimes is 54.4 ± 1.6, in good

agreement with the ratio of 54.66 ± 0.01 that is expected from the ratio of the $\Omega = 1$ character in the respective wavefunctions [155].

6.3 Theory

To calculate the radiative lifetime of the (1,0,1) level, the model as originally described by James [148] was used. Essential in this model are the matrix elements $\langle v_A | h_{A,a}(r) | v_a = 0 \rangle$ of the r-dependent spin-orbit coupling $h_{A,a}(r)$ and the matrix elements $\langle v_A | \mu_{A,X}(r) | v_X \rangle$ of the r-dependent electronic $A^1\Pi - X^1\Sigma^+$ transition dipole moment $\mu_{A,X}(r)$, together with the energy separation of the spin-orbit coupled states. The calculations were performed by Gerrit Groenenboom of the Radboud University of Nijmegen, The Netherlands. The results are presented in figure 6.3.

Using these results, a radiative lifetime for CO molecules in the (1,0,1) state of 3.16 ms was computed. In order to understand the 20 % discrepancy with the experimental value, we performed an extensive analysis on the quality of the potentials, and on that of the calculations of the spin-orbit coupling and transition dipole moment functions. James arrived at a calculated value of 2.93 ms for the (1,0,1) level [148]. We repeated the calculation of James by employing RKR potentials based on spectroscopic data available in 1971 and found a value of 2.94 ms. With our new RKR potentials and James' spin-orbit coupling and transition dipole function we obtain 2.93 ms. We therefore do not find the extreme sensitivity to the potential reported by Sykora and Vidal, and cannot reproduce their value of 3.41 ms [154].

From the results presented so far, we conclude that a model that takes into account only the $A^1\Pi$ intermediate state, cannot explain the observed lifetime of the $(1, 0, 1)$ level. The main sources of error are in the $A - a$ spin-orbit coupling and in the $A - X$ transition dipole moment. It seems unlikely, though, that the combined effect of these errors on the lifetime is more than 10 %. Only $^1\Pi$ states can have both a nonzero transition dipole moment to the ground state and a nonzero spin-orbit coupling to the $a^3\Pi_1$ state. Therefore, we made an estimate of the contributions of higher lying $^1\Pi$ states by calculating the effective $a - X$ transition dipole moment at $r = 2.3$ a_0 as a function of the number of intermediate states, using the result to scale the value of 3.16 ms obtained above. It was found that the higher states could account for the difference between theory and experiment. We suspect, however, that taking into account their r-dependence and obtaining convergence with respect to the number of $^1\Pi$ states will be difficult.

6.4 Pump-pump-dump scheme

Comparing the two measurements for the lifetime of the $a^3\Pi_1(v = 0, J = 1)$ and $a^3\Pi_2(v = 0, J = 2)$ state in figure 6.2, one notices that the signal-to-
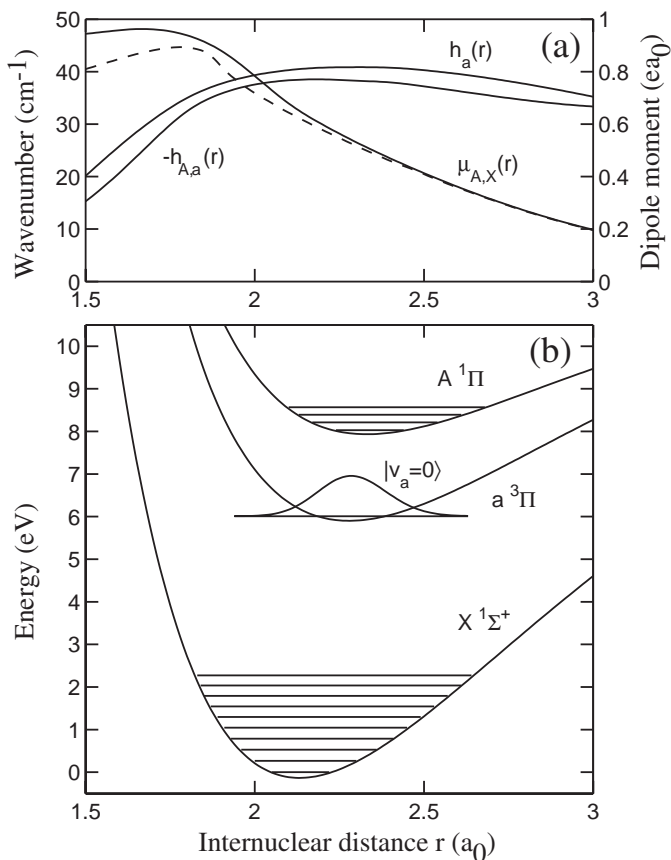
Figure 6.3: Panel (a) shows the $A - X$ electronic transition dipole moment $\mu_{A,X}(r)$ (in ea_0) of the present work (the solid line) and from reference [156] (the dashed line), together with the diagonal $[h_a(r)]$ and offdiagonal $[h_{A,a}(r)]$ spin-orbit coupling (in cm^{-1}). Panel (b) shows the RKR-potentials of the $X^1\Sigma^+$, the $a^3\Pi$, and the $A^1\Pi$ states of CO and the $|v_a = 0\rangle$ vibrational wavefunction.

noise ratio in the latter experiment is considerably lower. This is connected to the fact that the lifetime of the latter state is ~ 50 times longer and the $a^3\Pi_2(v = 0, J = 2) \leftarrow X^1\Sigma^+$ transition could not be saturated. An alternative way to populate the $a^3\Pi_2(v = 0, J = 2)$ level is a three laser pump-pump-dump excitation scheme (figure 6.4), which has the advantage of circumventing the weak $a^3\Pi_2(v = 0, J = 2) \leftarrow X^1\Sigma^+$ transition by combining three stronger transitions. The first laser in this scheme saturates the $a^3\Pi_1(v = 0, J = 1) \leftarrow X^1\Sigma^+(N = 0)$ transition at 619 nm, similar to the

lifetime-experiment shown above. The second pump laser (565 nm) pulse is fired a few hundred nanoseconds later and excites the molecules to the short-lived ($\sim$53.6 ns [157]) $b^3\Sigma^+$ state. After molecules in this state were pumped down by a third laser (566 nm) the $a^3\Pi_2(v = 0, J = 2)$ state was populated ten times more effectively compared to direct excitation. However, even if the majority of the trapped molecules reside in the $a^3\Pi_2(v = 0, J = 2)$ state, a pure state selective lifetime measurement is nonetheless disturbed by the spontaneous decay of molecules from the $b^3\Sigma^+$ state to other vibrational states in the $a^3\Pi$ state with different lifetimes, which can vary up to 30/40 % [153]. Samples of trapped cold molecules produced via the pump-pump-dump scheme are therefore less suited for state-selective lifetime measurements.
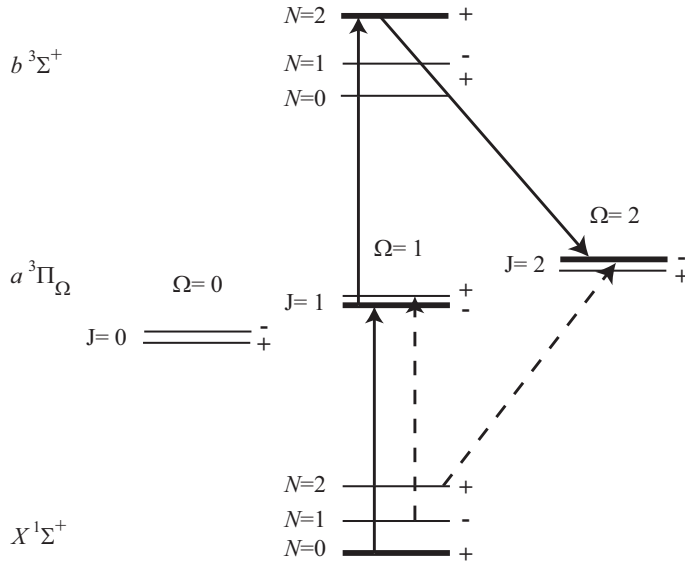
Figure 6.4: The dashed arrows denote the excitation scheme as used in the lifetime measurements. Alternatively, a three laser pump-pump-dump scheme is used to populate the $a^3\Pi_2(v = 0, J = 2)$ state ten times more effectively. The parities of the levels in lambda-doublets within the $\Omega = 2$ ($J = 2$) manifold were measured in a separate Laser Induced Fluorescence (LIF) experiment via the $b^3\Sigma^+$ state.

6.5 Conclusions

This chapter presents the electrostatic trapping of metastable CO molecules. We have exploited the long observation time allowed by the trap to measure the radiative lifetime of two different rotational levels in the $a^3\Pi, v = 0$ state.

These two measurements are mutually consistent and yield an accurate value of the radiative lifetime of the $a^3\Pi_1, v = 0, J = 1$ level of 2.63 ± 0.03 ms. Now that the radiative lifetime of this level is known with unprecedented precision, discrepancies with earlier calculated values have become apparent. This prompted us to perform more detailed calculations for this level. When only spin-orbit coupling of the $a^3\Pi$ state with the $A^1\Pi$ state is included, we compute a lifetime of 3.16 ms. We show that obtaining agreement between theory and experiment will require the calculation of the contribution of higher $^1\Pi$ states.

Furthermore, we describe the implementation of a three laser pump-pump-dump scheme which effectively populates the $a^3\Pi_2(v = 0, J = 2)$ state, yet in a less quantum state selective way. On the other hand, the factor ten gain in trapped number of molecules opens up the possibility of using metastable CO for a range of measurements on the manipulation of cold molecules, such as collision studies. Knowledge of the collisional properties at low temperatures is needed for the successful application of sympathetic cooling, which could be an essential tool to eventually bring cold molecule research into a new, unexplored regime.

Chapter 7

Trap loading of Stark-decelerated molecules

Neutral polar molecules in a low-field seeking state can be decelerated to standstill using a Stark decelerator, and can subsequently be loaded and confined in a trap. The efficiency of the trap loading process is determined by the degree in which the decelerated packet of molecules can be loaded into the trap without loss of molecules and without heating. In this chapter the loading of several types of electric and magnetic traps is discussed. A new electric quadrupole trap design is described and experimentally tested by comparing the trapping of OH radicals using this new and the conventional quadrupole trap designs. The loading of molecules into magnetic traps is discussed and designs for an electromagnet trap and a permanent magnet trap are presented.

7.1 Introduction

In the previous chapters the trapping of several polar molecules in an electrostatic trap has been presented. A general description of the principles of electrostatic trapping, using OD ($X\,^2\Pi$), NH ($a\,^1\Delta$), and CO ($a^3\Pi$) molecules as an example is given in chapter 2. The possibility to use trapped clouds of cold molecules in lifetime studies and other experiments has been discussed extensively. In chapter 5 a comparison of the 1/e trap lifetime of OH and OD has been presented to get insight in the trap loss processes that play a role when trapping cold polar molecules. The trapping of CO enabled an accurate study of the radiative lifetime of two electronically excited metastable states. Furthermore, as was mentioned in the introduction of this thesis, the trapping of molecules in magnetic traps allows for other, promising experiments. The accumulation of several packets of molecules, for instance, would become possible for NH molecules using a combination of a Stark decelerator and a magnetic trap. For all those studies it holds that the more molecules are trapped - or the higher the density of the trapped cloud - the higher the signal-to-noise ratio of those experiments will be. Moreover, new experiments will become possible when densities are higher; the probability for a collision event will increase and intriguing collisional properties of cold molecules, as were discussed in the introduction of this thesis, can be studied. If the density is increased even further and collision events become more frequent it could even become possible to exploit those collisions to further cool the trapped cloud via evaporative cooling.

Ultimately, the phase-space density, defined as the number of molecules in a quantum state per unit volume and unit momentum, that can be reached in the trap using a single loading cycle is limited by the phase-space density of the molecules in the molecular beam pulse. In principle, in state of the art molecular beams these are sufficient to reach high enough densities in the trap to allow for collisions. Obviously, it is imperative that the deceleration and trap-loading processes are performed with low losses. During the deceleration process in the Stark decelerator, low losses are assured by the concept of phase stability analogous to the phase-stable acceleration in charged particle accelerators [85]. Unfortunately, however, this is only true *inside* the Stark decelerator, even up to the very last deceleration stages, but it does not hold for the trapping region. The coupling of the decelerated packet into the trap is usually accompanied by substantial losses, that are essentially caused by the breakdown of phase stability for low velocities, in particular for velocities that the molecules need to have when they are loaded into the trap. The packet of slow molecules is not kept together sufficiently in the three orthogonal directions, and expands before entering the trap. This chapter summarizes knowledge on the optimal loading of traps, that was gathered over the years that the above mentioned trapping experiments were performed. General design criteria to accomplish ideal trap loading are given, and the practical limitations to realize

these are discussed.

7.1.1   Ideal trap loading

A trap can only confine molecules that have a position and velocity that are within the so-called acceptance of the trap. The position and velocity distribution of the beam that exits the decelerator is called the beam emittance of the Stark decelerator. In the ideal trap design, the (6D) beam emittance of the Stark decelerator is perfectly mapped onto the (6D) acceptance of the trap. This situation is graphically illustrated in figure 7.1 for the loading of OH molecules into an electrostatic trap. The left side of the figure shows the
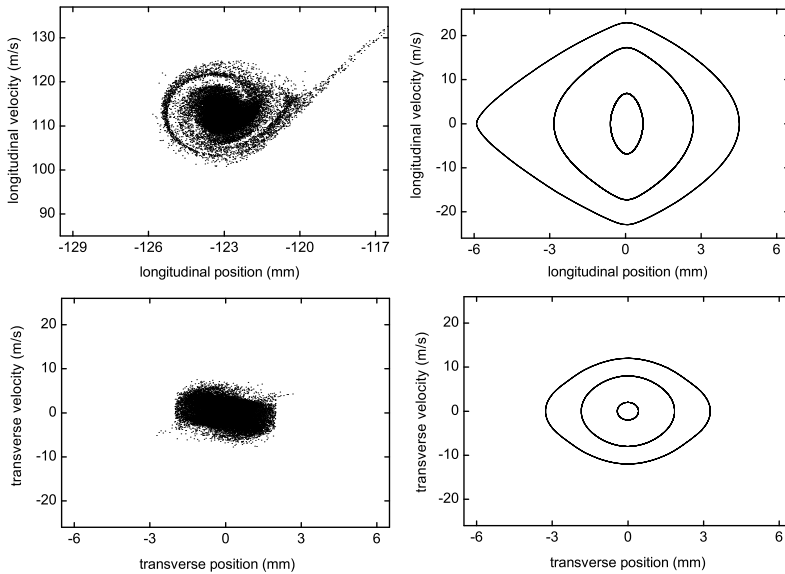
Figure 7.1: In an ideal trap loading procedure, the phase-space distribution of the molecules in the decelerator (left) is imaged onto the acceptance of the trap (right). This is illustrated both for the longitudinal (top) and transverse (bottom) direction.

calculated longitudinal and transversal phase-space distributions of a typical packet of molecules, 8 deceleration stages before it is trapped. The Stark decelerator is operated at $\phi = 60^o$, and the packet of molecules has a mean velocity of 112 m/s. The velocity distribution (FWHM) is 6 m/s in all directions, corresponding to a temperature of 18 mK. In an ideal trap loading

process, this packet is mapped without loss of molecules and without heating onto the acceptance of the trap, which is shown in the right side of the figure. In general, the acceptance of the trap can have a different size and shape than the beam emittance of the Stark decelerator. The shape of the longitudinal acceptance in, for instance, a quadrupole trap is identical to the shape of the transverse acceptance, apart from a small geometric factor relating the two. For the packet of slow molecules that exits the decelerator, however, the longitudinal and transverse motions are much less coupled, and in general the beam emittance can be different in each direction, as will be shown later in this chapter. In principle, a good 6D match can be achieved by installing appropriate focusing elements and free flight sections between the decelerator and trap that allow for independent control over the longitudinal and transverse motion of the molecules. A pulsed hexapole can be used to image the transverse phase-space distribution of the decelerated beam onto the transverse trap acceptance. In the longitudinal direction, this can be achieved by installing a buncher [112]. Although in theory these elements allow for an (almost) perfect phase-space matching, in practice there are also large disadvantages to this approach. Most importantly, these elements significantly increase the distance between the decelerator and trap. In view of the low longitudinal velocity that is required for trap loading (typically 20 m/s or less at the exit of the last deceleration stage, just before the loading), the packet of molecules will spatially expand significantly in the free flight sections between the elements. This will inevitably lead to a large loss of molecules as only a small part of the beam can be manipulated and loaded into the trap. This was indeed observed in the initial trapping experiments with ND_3 molecules where a short hexapole [38] or a bunching element [97] was installed between the decelerator and trap to allow for phase-space manipulation of the packet. In more recent trapping experiments with OH radicals, the more pragmatic approach to install the trap as close as possible to the exit of the decelerator was followed [47, 78]. Although the possibility to influence the phase-space distribution of the packet is compromised, this strategy reduced the losses during the trap loading significantly. However, a non-negligible distance between the decelerator and trap cannot be prevented. The limitations to obtain optimal trap loading efficiency have already been realized and discussed in the first trapping experiments of OH radicals in 2005 [47]. Referring to figure 3 of this publication, the signal of the trapped OH molecules was optimal by loading a packet of molecules with a velocity that is too high. The packet spreads out less, but comes to a standstill past the center of the trap. This leads to a donut-shape longitudinal phase-space distribution that basically fills the entire trap volume. The impossibility to optimize simultaneously the number and temperature of the trapped molecules in this trap design was confirmed in an experiment where the decelerator and trap were optimized using evolutionary strategies. These results were presented and discussed in section 2.4.2 of this thesis.

The trap loading experiments and calculations that are presented in this

chapter all fulfill the condition that the mean velocity of the molecular packet is zero at the moment the trap is switched on. This ensures the best possible overlap of the longitudinal phase-space distribution of the molecular cloud with the trapping potential, and is therefore a prerequisite to load molecules into a trap without loss and without heating.

7.2 Loading of electrostatic traps

To appreciate the difficulty of the efficient loading of Stark-decelerated molecules into an electrostatic trap, a detailed discussion of the trap loading procedure is required. In this section, a number of trajectory calculations is presented that show the problems that can occur during the trap loading process. The geometrical details of the quadrupole trap that has been used in our experiments (discussed in chapter 2) are depicted in figure 7.2. The figure shows a cut of the cylindrically symmetric trap, consisting of a ring electrode and two parabolic endcaps. The openings in the left and right endcap allow the entrance of the molecules and the exit of the fluorescence light for detection, respectively. The last three electrode pairs of the Stark decelerator are shown schematically; in practice they are placed alternating in the two transverse directions, as described in chapter 2.
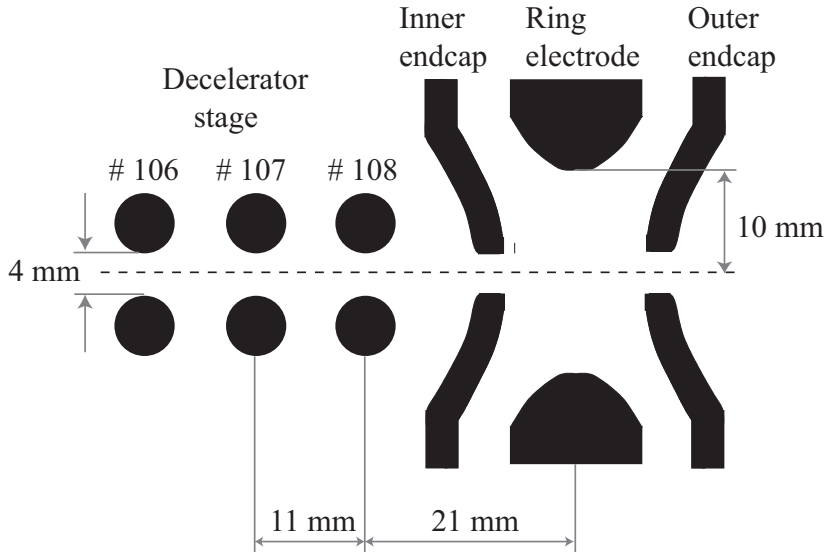

Figure 7.2: Schematic representation of the geometry of the last stages of the decelerator and the trap region. The trap consists of two hyperbolic endcaps and a ring electrode.

The trap loading procedure of this trap is discussed in section 7.2.1, after which a new trap design is presented in section 7.2.2. To exemplify the underlying ideas of the different trap loading strategies, the trap loading procedures are discussed first with an emphasis on the evolution of the longitudinal phase-space distribution of the packet of molecules during the trap loading process. An experimental comparison of the efficiency of the different trap loading strategies is presented in section 7.2.3. In section 7.2.4, a discussion of the evolution of the transverse phase-space distribution is given.

7.2.1 Conventional quadrupole trap

A pictorial presentation of the principles of the trap loading process, as it has been employed thus far in our OH trapping experiments, is shown in figure 7.3. The voltage configurations of the individual electrodes in the various stages of the loading sequence are shown in the top of this figure, and the corresponding potential energy curves for an OH molecule that travels along the beam axis are shown directly below. The part of the potential that the synchronous molecule experiences during the loading process is indicated by the thick lines. In the loading configuration a voltage of 10 kV, 15 kV and -15 kV is applied to the left endcap, ring electrode and right endcap, respectively. This creates a quadratic loading potential that allows a maximum velocity of 14.9 m/s for the OH radicals at the exit of the decelerator in order to come to a standstill at the trap center. This velocity is produced by switching the voltages of the Stark decelerator at $\phi = 56^o$. The last stage of the decelerator switches off when the synchronous molecule has reached position A. At this time, the electrodes are switched into the in the so-called *loading* configuration. Molecules experience the potential corresponding to this configuration from position A, via position B, to position C. When the synchronous molecule has finally come to a standstill at position C, the trap center, the voltages on the electrodes are switched to the *trapping* configuration. In the lower panel of figure 7.3, the evolution of the longitudinal phase-space distribution of the decelerated packet is shown, as it results from numerical simulations of the trap loading procedure. The parameters that were used in these simulations apply to the experiments that are presented in chapter 2. The distributions are shown at the times at which the synchronous molecule has reached the positions A, B and C. These times are also referred to as times A, B and C. The right-most panel shows the phase-space distribution of the cloud after 20 ms of trapping.

At time A the packet occupies a region in longitudinal phase-space with a velocity spread of 7 m/s (FWHM), centered around a velocity of 15 m/s. After the switching on of the loading potential, this packet first has to overcome a small potential hill in the region in between position A and position B. Since the velocity spread is relatively large, a sizeable part of the molecules at time A does not possess enough kinetic energy to overcome this barrier and is reflected, as can be seen from the molecules with negative velocity in the phase-space

Figure 7.3: Voltage configurations (top), corresponding potential energy curves for OH molecules along the beam axis (middle), and simulated longitudinal phase-space distributions (bottom) at various stages of the trap loading procedure.

distribution at time B (second graph of the lowest panel in figure 7.3). From time B on, molecules are decelerated on the harmonic loading potential and rotate in phase-space around the synchronous molecule. This results in a rather poor overlap of the molecules with the trap acceptance -that is shown as an overlay- at time C. A large part of the packet is not contained within the trap acceptance, and will not be confined when the trapping potential is switched on.

Inserting a free flight section

In the loading process as sketched above, a substantial fraction of the molecules is reflected by the small potential hill in front of the actual loading potential, i.e., the potential in the region between points B and C. In order to suppress these losses this potential hill can be lowered by reducing the voltage on the first end-cap electrode in the loading configuration. This approach has also been taken in the past [47, 78] and has been demonstrated to improve the efficiency of the loading process. A disadvantage of this approach, however, is that the reduced voltage lowers the total height of the potential, and a slower packet of molecules is required to load the trap. In addition, reduction of the voltage on the left endcap distorts the harmonicity of the loading potential.

An alternative approach to prevent losses due to reflection on the "pre-bump" in front of the real loading potential, is to switch the trap into the loading configuration only when the synchronous molecule has reached position B. In this case, there is no "prebump", and the molecular packet can progress in free flight to the trap region. This procedure is sketched in figure 7.4. After molecules are decelerated to 15 m/s by the decelerator and exit the decelerator at time A, all voltages are switched off, leaving the packet in a field-free region. At time B the mean velocity of the packet is still 15 m/s, but the distribution is stretched in position due to the absence of a potential. At time B, the loading configuration of the trap is switched on and the molecules are decelerated to a mean velocity of zero at time C, where the molecules are subsequently trapped.

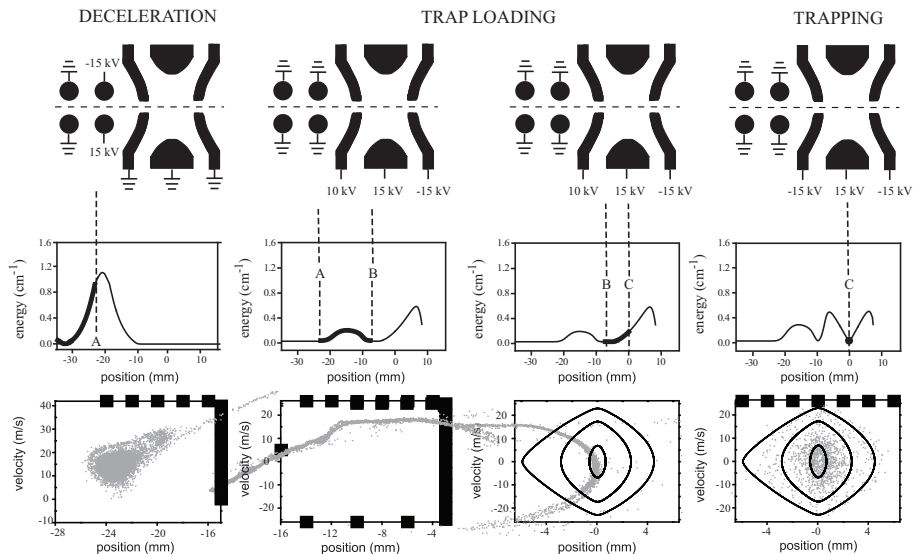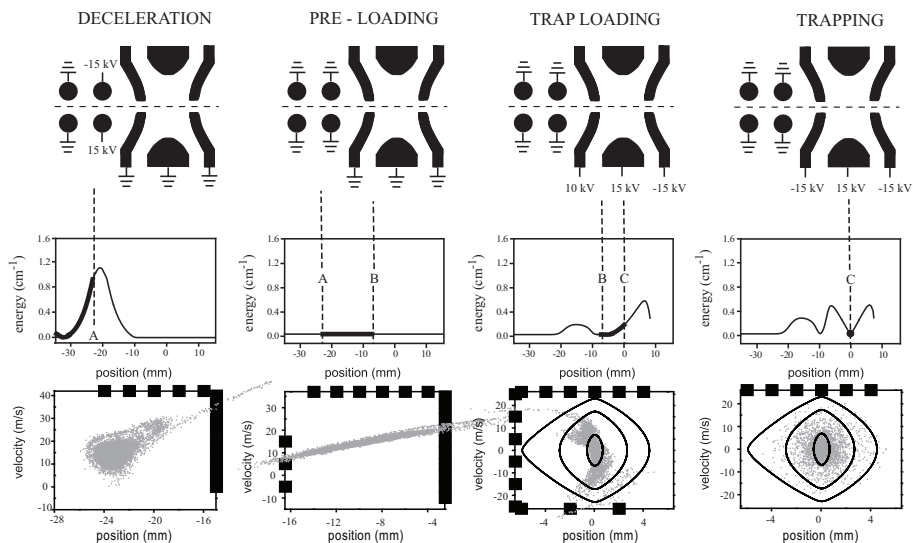Figure 7.4: Voltage configurations as applied in the loading sequence including a free flight section (top). Corresponding potential energy curves for OH molecules along the beam axis (middle). Simulated longitudinal and transverse phase-space distributions at various stages of the experiment (bottom).

As is evident from figure 7.4, the loss of molecules due to reflection on the "prebump" is eliminated, and more molecules can enter the trap. A disadvantage, however, is that no transverse focussing forces act on the molecules between position A and B, and the packet of molecules will transversely spread out more than in the conventional trap loading scheme. The spreading out can lead to additional losses as molecules may not be able to pass the entrance hole in the left endcap, and may crash onto the trap electrodes. The simulations indicate that the improvements by eliminating the "prebump" outweigh the

additional losses due to inferior transverse focusing, and a larger number of molecules can be confined in the trap in this way.

7.2.2   Split-endcap quadrupole trap

In the above described trap design the trap is positioned as close as possible to the exit of the Stark decelerator. This is probably always preferred over designs that include additional manipulation elements, but nevertheless the trap loading is unsatisfactory. The molecular packet spreads out significantly before entering the trap, resulting in a poor overlap of the molecular phase-space distribution with the trap acceptance. It appears that an improvement can be obtained if the sequence of potentials that keeps the packet together inside the decelerator can be extended into the trap region. Referring back to figures 7.3 and 7.4, the breakdown of this loading procedures is located between the positions A and B. The basic concept of the modified quadrupole trap design is to create a high potential hill in the region AB that can be used as an additional electric field stage of the decelerator, effectively merging the Stark decelerator with the electrostatic trap. It is noted that this idea has also been implemented in trapping experiments using Stark-decelerated ND_3 molecules [158], where the trap design that was used allowed for a straightforward implementation of an additional electric field stage. For our cylindrically symmetric quadrupole trap, this merging is achieved by breaking the symmetry of the left endcap. In the new trap design this electrode is replaced by two half endcaps with a small vacuum slit between the two halves. The schematic side and front views of the new electrodes, referred to from now on as the split-endcap electrodes, are shown in figure 7.5. The relevant technical details on the dimensions of the trap region are given in figure 7.2. The new trap consists of a ring electrode, centered 21 mm downstream from the last electrodes of the decelerator, and two hyperbolic endcaps. The ring electrode has an inner radius R of 10 mm and the two endcaps have a half-spacing of $R/\sqrt{2}$. The schematic view in figure 7.5 shows a small curvature along the vacuum slit between the two halves of the endcap, that is introduced to improve the transverse focusing properties of the trap (see section 7.2.4).

Analogous to figure 7.4, the voltages that are applied to the electrodes, the on-axis potential energy curves that the synchronous molecule experiences during the trap loading process, and the evolution of the longitudinal phase-space distribution of the packet of molecules, are shown in figure 7.6. For clarity, the sequence of high voltage pulses that is applied to the last two decelerator stages and to each of the four trap electrodes, are indicated in figure 7.5. As before, the last pair of electrodes of the decelerator is switched to ground when the synchronous molecules has reached position A. At this time, both halves of the split end-cap are switched to high voltage (10 kV) of opposite parity, creating a high electric field in between both split endcap electrodes. Simultaneously, the fore-last set of electrodes of the decelerator are switched

Side view   Front view

3 mm
4 mm

	Deceleration	Pre-loading	Loading	Trapping	Detection

Decelerator stage # 107 — ±15 kV (Pre-loading) — 0 kV

Decelerator stage # 108 — ±15 kV (Deceleration) — 0 kV

Split endcap electrode 1 — +10 kV — -15 kV — 0 kV

Split endcap electrode 2 — -10 kV — +10 kV — -15 kV — 0 kV

Ring electrode — +15 kV — 0 kV

Outer endcap electrode — -15 kV — 0 kV
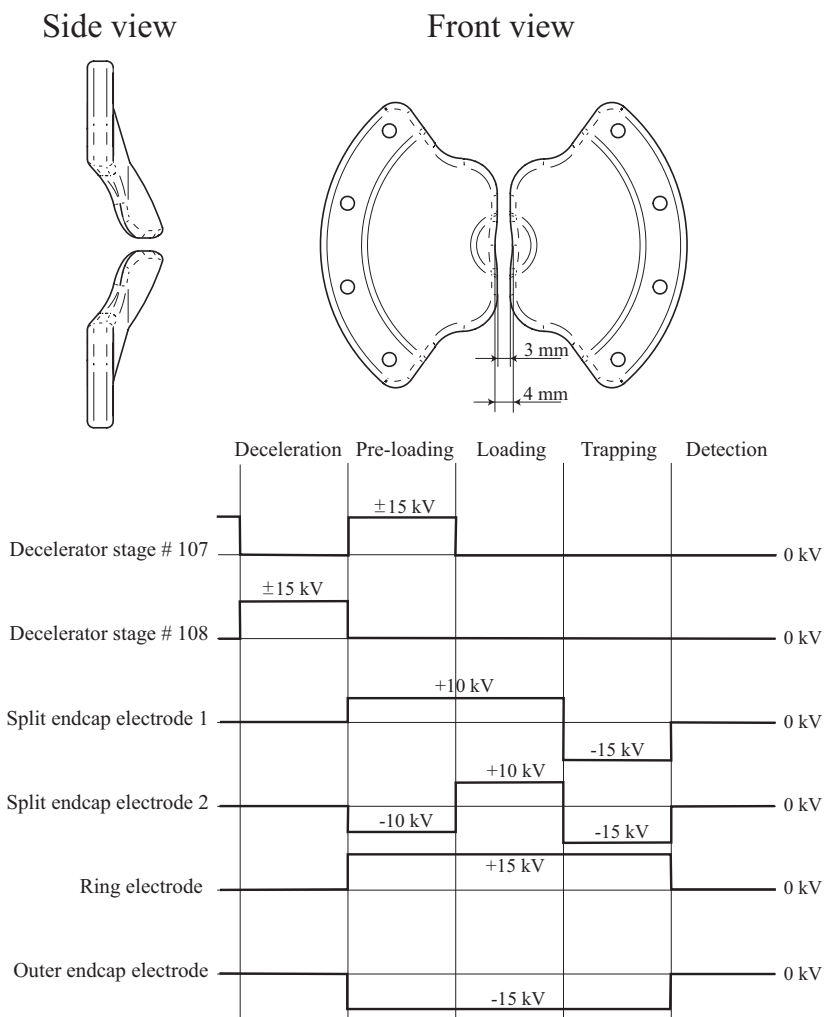
Figure 7.5: Side and front views of the split-endcap electrodes. The sequences of high voltage pulses that are applied to all four trap electrodes, as well as to the last two electrode pairs of the decelerator, are graphically shown.

to ±15 kV. In this so-called *pre-loading* configuration, a potential hill in the region AB is created that has a similar shape to the series of potentials that are present inside the Stark decelerator, and that can be used as an additional deceleration stage. As a result, the forward velocity of the packet of OH radicals at time A is higher (32 m/s, FWHM 6 m/s) than in the previously discussed trap loading schemes. During this pre-loading configuration, the mean velocity
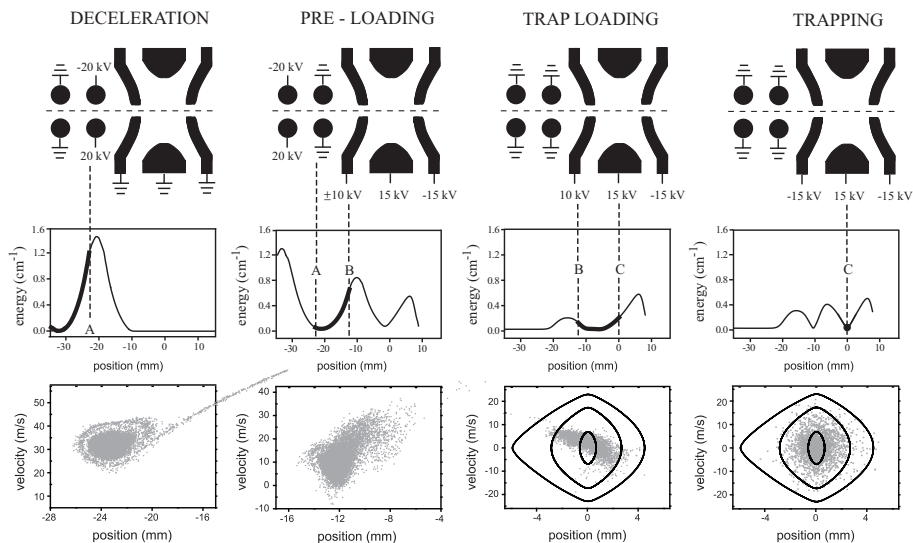
Figure 7.6: The Stark decelerator and electrostatic trap are merged in a new electrode geometry. The potential hill in the region AB is used as an additional deceleration stage.

of the packet is reduced to 10 m/s (FWHM 12 m/s). It is evident from the phase-space distribution, that the packet of molecules is kept together much better during this period. When the synchronous molecule has reached position B, the trap loading procedure proceeds in the usual way. The trap can be used in the loading and trapping configuration by switching both halves of the split endcap to the same polarity, first to +10 kV and then to −15 kV, respectively. The distance of the two electrodes is small enough that the electric field distribution in the trap is not significantly different from the original situation without a gap, if both halves are switched to high voltage of equal polarity. During the loading configuration, the remaining kinetic energy is taken out on the loading slope such that the packet arrives with an average velocity of zero in the center of the trap. At this moment, the trap is switched to the trapping configuration, and the part of the molecular packet that is within the acceptance of the trap is confined.

It is seen that, compared to the trap loading strategies using the cylindrically symmetric endcap, the longitudinal space-space distribution is spread out less at the moment the trap is switched on. Although the phase-space distribution is not perfectly matched to the trap acceptance, almost all molecules are confined within the innermost trap contours.

7.2.3 Experiments

To experimentally study the difference in trap loading efficiency between the conventional and the split-endcap quadrupole trap, a direct comparison between the old and new trap loading approaches is required in the same experimental setup. For this, the original cylindrically symmetric left endcap is replaced by two split endcap electrodes. Both split-endcap electrodes, the ring electrode and the outer endcap electrode are individually suspended and connected to an own set of high voltage switches. To enable the switching between voltages of different amplitude and/or polarity, as required for both split-endcap electrodes, a number of high voltage switches are configured in series, i.e., the output of one switch is connected to one of the input ports of the next switch. With the split-endcap quadrupole trap in place, trap loading measurements that resemble the old trap loading approach are still possible. For this, identical high voltage pulses are applied to both halves of the split endcap, creating a trap that is conceptually identical to the original cylindrically symmetric quadrupole trap.

For the three trap loading strategies, the loading of the molecules into the trap is experimentally studied by terminating the trap loading sequence at different stages of the trap loading procedure, and by recording the time-of-flight profiles of the slow packet of OH radicals at the center of the trap. In agreement with earlier findings, the first strategy mentioned in section 7.2.1 was found to be very inefficient and resulted in a poor signal-to-noise ratio in the experiments. These measurements are not shown here. The experimental results that are obtained when the second loading strategy is followed, in which the small potential barrier in the region AB is eliminated by inserting a free-flight section (figure 7.4), are presented in figure 7.7. The Stark decelerator is programmed to produce a packet of OH radicals with an average forward velocity of 15 m/s. In curve (a) the time-of-flight profile is shown of the packet that exits the decelerator, i.e., the trap loading procedure is stopped after the last stage of the decelerator is switched off. In this curve, the signature of the slow packet of molecules is hardly visible. This is due to the low forward velocity of 15 m/s (FWHM 6 m/s) of the packet, and the spreading out of this packet while flying to the trap center. In curve (b) the time-of-flight profile is shown that is observed when the "loading" part of the trap loading procedure is included. The packet comes to a standstill in the center of the trap 8.0 ms after production. The higher signal intensity compared to curve (a) is due to the improved focusing properties when the loading potential is present. Finally, in curve (c), the full trap loading sequence is used. After switching on of the trapping potential, a large increase of signal followed by a damped oscillation is observed. The time-of-flight profiles that result from three dimensional trajectory simulations are shown underneath the experimental profiles. Satisfactory agreement is obtained for all curves, and the relative signal intensities of the different profiles are reproduced rather well. The difference between the simu-
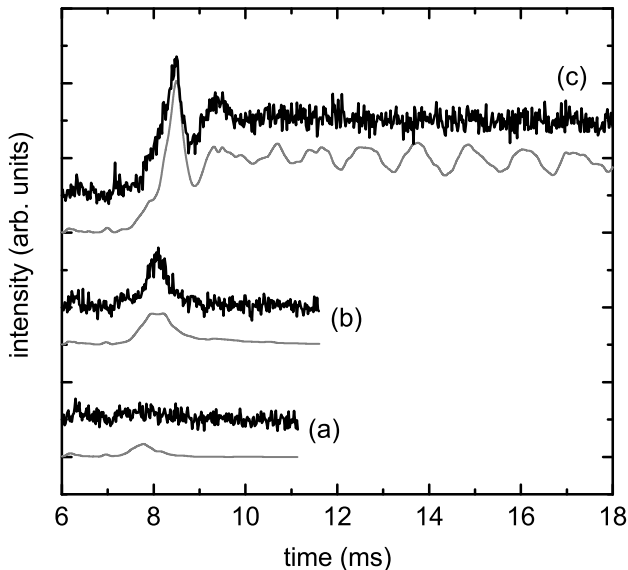
Figure 7.7: Time-of-flight profiles, obtained following the trap loading strategy as described in figure 7.4. The profiles that are obtained from three dimensional trajectory simulations of the experiment are shown underneath the experimental profiles. The experimental and simulated profiles are given a vertical offset for reasons of clarity.

lated and measured curves regarding the damping of the oscillation is discussed later, in section 7.2.4.

In figure 7.8 the measured time-of-flight profiles are shown that correspond to the loading strategy when the split-endcap electrodes are used as an additional deceleration stage. Similar to the time-of-flight profiles that are presented in figure 7.7, the "deceleration", "loading", and "trapping" profiles are shown in curves (a), (c), and (d), respectively. The additional profile that corresponds to the "pre-loading" configuration, is shown in curve (b). The packet of molecules that exits the decelerator has a forward velocity of 32 m/s with a velocity spread of 7 m/s, and arrives at the trap center 6.8 ms after its production. Due to the higher forward velocity, the packet spreads out less, and the signature of the slow packet is clearly visible in the time-of-flight profile. When the "pre-loading" configuration is added to the trap loading sequence, curve (b) is obtained. The packet arrives later at the trap center, and the arrival time distribution is broader. This reflects the lower forward velocity of
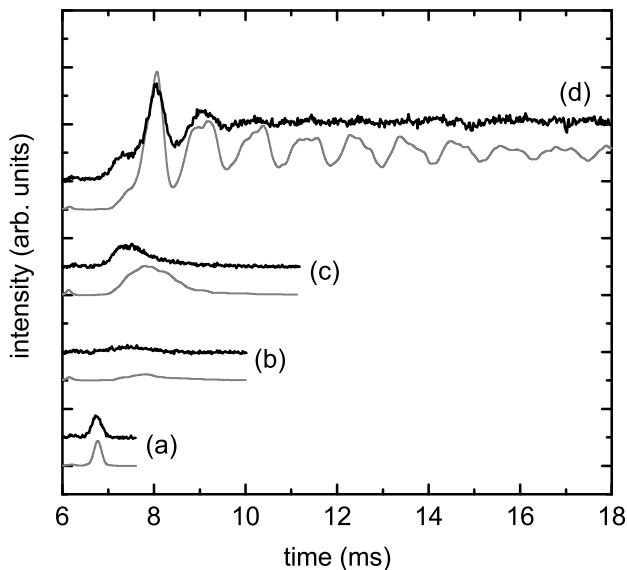
Figure 7.8: Time-of-flight profiles of OH radicals at different stages of the trap loading procedure that is depicted in figure 7.6. Underneath the experimental profiles, the profiles that are obtained from three dimensional trajectory simulations of the experiment are shown.

10 m/s. This very low forward velocity also explains the reduced signal intensity that is observed; the packet of molecules expands significantly when the voltages on the trap electrodes are switched off in this time-of-flight measurement. The packet is brought to a standstill at the center of the trap when the "loading" part is added (curve (c)). The loading potential prevents the packet from spreading out, and the signal intensity of the stopped molecules is higher again. Curve (d) corresponds to the full trap loading sequence. Again, a large increase of signal followed by a damped oscillation is observed when the trap is switched on. The time-of-flight profiles that result from three dimensional trajectory simulations are shown underneath the experimental profiles. Again, satisfactory agreement is obtained for all curves, although the slow packet in curves (b) and (c) arrives earlier in the experiment than in the simulation. This is indicative of an over-estimate of the pre-loading potential in the simulations. Deviations originate from misalignments of the trap electrodes in the experiment, and from small differences between the actual and simulated shapes of the electrodes.

Experimental comparison of the trap loading strategies

The intensity of the fluorescence signal from the trapped sample of molecules that is obtained when the three different trap loading strategies are used can be directly compared. The experimental results are summarized in table 7.1. In this table, the three loading strategies are referred to as "conventional loading", "free flight loading", and "split-endcap loading", and the figures in which these loading strategies were explained are given as a reference. The fluorescence intensities are normalized to the fluorescence intensity that is obtained using the conventional trap loading strategy. It is seen that the trap loading strategy

Table 7.1: Results of experiments using different trap loading strategies.

Trap loading	Described in	Signal intensity
Conventional	figure 7.3	1.0
Free flight	figure 7.4	4.0
Split-endcap	figure 7.6	8.9

using the "split-endcap" electrodes results in a factor 8.9 higher signal intensity than the conventional loading strategy. It is noted that this value represents a lower limit of the gain, as the present experiments are all performed with the split-endcap electrodes. Compared to the original spherically symmetric endcap, that has a 4 mm diameter opening, the slit offers a higher probability for the molecules to enter the trap.

From table 7.1 it also follows that the split-endcap strategy results in a factor 2.2 higher signal intensity than the (experimentally much less elaborate) strategy in which a free flight section is included using the conventional electrodes. In view of the longitudinal phase-space distributions that correspond to these strategies (see figures 7.4 and 7.6), this modest gain is somewhat disappointing. Obviously, the split-endcap electrodes are successful in keeping the packet of molecules together during the "pre-loading" part of the trap loading sequence (compare the second panel of figures 7.4 and 7.6). However, apparently this gain is partially undone during the "loading" part of the sequence, resulting in a gain of only a factor 2.2. Indeed, three dimensional trajectory simulations reveal that with the current implementation of the split-endcap loading strategy, the molecules are focused too strong in one of the transverse directions before entering the trap. This will be discussed in the next section.

7.2.4   Transverse phase-space evolution

Analogous to the evolution of the longitudinal phase-space distribution during the trap loading process of the split-endcap quadrupole trap, the phase-space distribution in both transverse directions is shown in figure 7.9.

The transverse coordinate y (top panels) is defined along the long axis of the last electrode pair. Coordinate z (lower panels) is defined perpendicular to
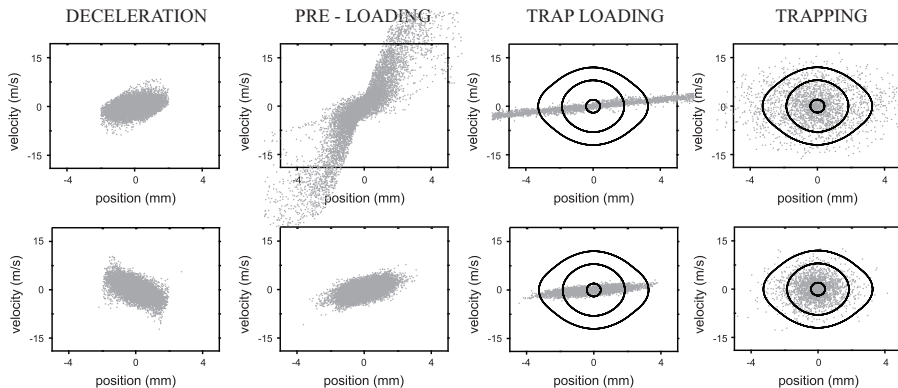
Figure 7.9: Transverse (y (top) and z (bottom)) phase-space distributions at various stages of the experiment. These transverse phase-space snapshots belong to the longitudinal distributions as presented in figure 7.6.

that axis. As can be seen on the left side of figure 7.9, the molecular packet has transverse dimensions of 4x4 mm at the exit of the decelerator, given by the distance between the electrodes in each electrode pair. The split-endcap electrodes face each other in the y direction and create a pre-loading field that is perpendicular to the field of the last deceleration stage. Therefore, as the packet travels in the pre-loading field it is not only decelerated in the longitudinal (x) direction, but also gets strongly focused in the y direction. The exact strength of this focusing force depends on the longitudinal position of the molecules, resulting in a non-uniform rotation of the phase-space distribution. During the "pre-loading" configuration, the molecules hardly experience focusing forces in the z direction (the direction along the slit of the split-endcap electrodes), and in this direction the phase-space distribution evolves more-or-less like in free flight. When the packet progresses on the subsequent (cylindrically symmetric) loading potential, the molecules get focused in the y and z direction equally strong. These focusing forces, however, are limited, and in addition to a rotation in phase-space, the packet also elongates spatially. The resulting phase-space distributions at the moment the trap is switched into the "trapping" configuration are shown in the third panel of figure 7.9.

It is clear from these distributions that, in contrast to the longitudinal phase-space overlap, the phase-space overlap with the transverse trap acceptance is rather poor. In the y-direction, the focusing force during the "pre-loading" configuration has been too strong. A significant part of the molecules pass through a focus, resulting in a large velocity spread when the packet enters the "loading" potential. This large velocity spread is transferred into a large position spread during the "loading" part of the sequence. In the z-direction, however, the focusing forces are too weak. The packet spreads out significantly,

also resulting in a large position spread at the time the trap is switched on.

The (transverse) mismatch between the phase-space distribution of the molecular packet and the trap acceptance at the moment the trapped is switched on can also be inferred from the time-of-flight profile in figure 7.8(c), that is shown again in the upper curve of figure 7.10. Pronounced oscillations in the signal intensity of the trapped molecules are observed in the first milliseconds after the trap has been switched on. These oscillations correspond to fluctuations in the density of molecules within the detection volume, that can be observed if the detection volume is considerably smaller than the total volume of the trap. The detection volume is given by the 4 mm diameter of the detection laser, that crosses both transverse coordinates y and z under an angle of 45°, and the opening angle of the detection zone, given by the 6 mm diameter opening in the right endcap. In figure 7.10 it is shown that the fluctuations in density are mainly caused by the rotation of the phase-space distribution of the packet in the transverse directions. At time I, the time that the molecular packet arrives in the trap center and the trap is switched on, the packet is longitudinally and transversely (almost) velocity-focused; the packet is spatially large (3x10x4 mm) and has a relative small velocity spread (FWHM) of about 7, 5, and 2 m/s in the x, y, and z direction, respectively. As can be seen from the top of the figure this situation corresponds with a relative low LIF signal in the time-of-flight profile, since a large fraction of the molecules is located in the region of the trap that is not overlapped with the detection laser. At time II, the situation is exactly opposite. The phase-space distributions have rotated and most molecules are located in the center of the trap. The packet has a size of 1x2x2 mm and a relatively high velocity spread of 21, 18, and 8 m/s in the x, y, and z direction, respectively. This situation corresponds with an intense LIF signal. The phase-space distributions after 20 ms of trapping, shown in figure 7.10 (time IV), show that the packet has lost his "structure" in phase-space and the trap acceptance is homogeneously filled around the center in all three directions. The size of the molecular packet and the ratio between the velocity distributions in the three directions are now given by the shape of the phase-space acceptance of the trap. The spatial distribution at this moment is 2x2x2 mm, the velocity distribution 10, 8, and 7 m/s in the x, y, and z direction, respectively. The damping of the oscillations towards this "steady-state" situation is caused by the coupling of the motion in all coordinates. The exact number of oscillations that is actually seen in the simulated time-of-flight profile strongly depends on the implementation of the detection zone in the simulation and therefore differs from the number of oscillations that is seen in the experiment.

Comparison of the trap loading strategies

The three-dimensional trajectory simulations presented above can be used to calculate the expected efficiency of the trap loading process, and the temper-
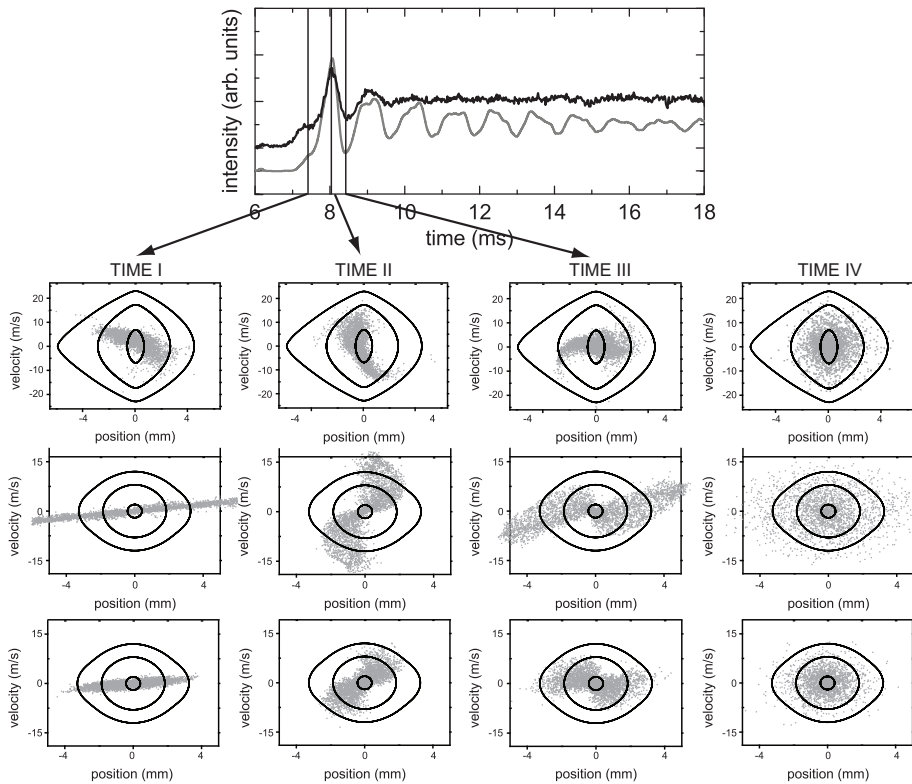
Figure 7.10: Phase-space distributions in the longitudinal (x, top panel) and in both transversal (y, middle panel; z, lower panel) directions at different points in time, indicated with vertical lines in the time-of-flight profile shown on the top. Time I is the time of switching from the loading to the trapping potential. Time II and III correspond to the first maximum and minimum of the oscillations as observed in the time-of-flight profile of the trapping experiment, respectively. Time IV is 20 ms after the trap has been switched on.

ature of the trapped sample of molecules. This efficiency is defined as the fraction of the molecules that exit the decelerator and that are still confined in the trap, 20 ms after the trap has been switched on. These simulations were performed for all three trap loading strategies that were experimentally studied, and are given in table 7.2. It is interesting to compare these simulated efficiencies with the experimental results that are summarized in table 7.1. For the latter, the ratio between the absolute number of molecules that are confined in the trap is of relevance. This ratio can differ from the ratio of the efficiencies, as the molecular packet has a different velocity in the last stage of the decel-

erator for the different loading strategies. The resulting number of molecules, normalized to the number that is obtained using the "conventional" loading strategy, is given in the third column of table 7.2. Finally, the temperature T of the trapped sample of molecules that follow from these simulations is given in the last column of table 7.2. This temperature is defined using the average kinetic energy of the molecules $E_{kin} = 3/2k_BT$, where k_B is the Boltzmann constant.

Table 7.2: Results of the three dimensional trajectory simulations using different trap loading strategies.

Trap loading	Described in	Efficiency	$N_{molecules}$	Temperature
Conventional	figure 7.3	15 %	1.0	59 mK
Free flight	figure 7.4	27 %	1.8	51 mK
Split-endcap	figure 7.6	27 %	1.9	48 mK

It is seen that in the simulations, the trap loading efficiency, as well as the number of trapped molecules and temperature of the trapped ensemble, are very similar for the "free flight" and "split-endcap" trap loading strategies. In addition, it is found that the efficiency of both trap loading strategies is about a factor 2 higher than the "conventional" trap loading strategy. These results are not in agreement with the experimental findings that are given in table 7.1. The gain of "free flight loading" compared to "conventional loading", as well as the gain of "split-endcap loading" compared to "free flight loading" are underestimated in the simulations. It is noted that in view of the low velocity of the molecules during the trap loading process, and hence their sensitivity in both the experiment and the simulations to the details of the potentials involved, a much better agreement is difficult to obtain.

Although the simulations do not quantitatively reproduce the observations, they can be used to qualitatively understand the trap loading process. In fact, according to the simulations, no gain is expected for the "split-endcap loading" compared to the "free flight loading". This surprising result indicates that the poor transverse focusing properties of the split-endcap electrodes diminish the gain that is accomplished in the longitudinal direction. This is the main lesson that can be learnt from these simulations: the shape of the split-endcap electrodes in the region of the slit is very critical to the success of the "split-endcap" trap loading strategy, and these should be carefully designed. In its current implementation, the advantages that the "split-endcap" loading strategy can offer are not fully exploited.

7.2.5   Conclusions

In this chapter, the efficiency of the loading of Stark decelerated molecules into an electrostatic quadrupole trap has been studied, both experimentally and

using extensive three dimensional trajectory calculations. These studies have been triggered by high losses that have been observed during the trap loading process in previous Stark deceleration and trapping experiments. These losses originate because it is difficult to keep the molecular packet together in the region between the end of the Stark decelerator and the first electrode of the quadrupole trap. Experimentally, a new trap design that allows for a continuation of the Stark decelerator into the trap region was found to result in a factor 8.9 more trapped molecules than when the conventional trap loading scheme is used. With this trap, the highest trap loading efficiency that has been reported to date for an electrostatic quadrupole trap has been obtained. For this, however, a complicated electrode design for the first endcap of the trap, and elaborate high voltage electronics, are required. An improvement of about a factor 4 can also be obtained using the original cylindrically symmetric trap electrodes, by inserting a free flight section in the trap loading sequence. In all experiments as well as in the calculations, the condition to bring the packet of molecules to a standstill in the center of the trap was fulfilled. The experimental results are qualitatively reproduced by three dimensional trajectory simulations, from which a detailed understanding of the trap loading process can be obtained.

The ability of trap loading schemes to keep the packet of molecules together in the longitudinal direction, is an important prerequisite for the efficient loading of Stark decelerated molecules into a quadrupole trap. Although this is achieved, for the first time, with the "split-endcap" quadrupole trap, the current implementation of the trap obviously also suffers from major shortcomings. It was shown in figure 7.9 that in this particular design the transverse focusing in one direction is much larger than desired. The molecular packet is overfocused, causing a transversal mismatch that cancels the gain that is accomplished in the longitudinal direction.

A solution for this problem would be the reduction of the transversal focusing force, together with a conservation of the longitudinal deceleration forces. In the current design, however, those two forces are linearly related. The height of the pre-loading potential, as shown in figure 7.6, is reduced if the 20 kV voltage difference between the two halves of the split endcap electrode is lowered. In trajectory calculations, using a 4, 8, 12, and 16 kV voltage difference between those electrodes, this reduced height was compensated by producing slightly slower molecular packets with the decelerator. This, however, has again consequences for the time that the molecules spend in the pre-loading field. The calculations show that these effects cancel each other, and no relevant improvement in terms of transverse phase-space matching can be achieved with the existing design. In the future, the idea to merge the decelerator and trap can be implemented in a better way using differently designed split endcap electrodes. In order to reduce the transverse focusing forces and at the same time maintain the longitudinal loading potential, the split endcap electrodes could, for instance, be shaped such that the entrance opening for the molecules has

a more conical shape. In general, any alternative design will have to be tested in three dimensional trajectory calculations to test for its ability to accomplish 6D phase-space matching.

7.3   Loading of magnetic traps

It was mentioned several times in this thesis already, that a route towards higher number densities in the trap, apart from efficient trap loading, is the accumulation of several packets of molecules that are produced in distinct cycles of the experiment. Although an increase of the phase-space density in its most direct way is forbidden by Liouville's theorem, a reloading scheme has been proposed for the NH radical that circumvents this fundamental obstacle [74]. In this scheme, NH radicals that are produced in the long-lived metastable $a\,^1\Delta$ state are Stark decelerated to a standstill and subsequently optically excited to the $A\,^3\Pi$ state. Spontaneous fluorescence from the $A\,^3\Pi$ state to the $X\,^3\Sigma^-$ ground state provides the required uni-directional pathway. A magnetic trap can be placed at the end of the Stark decelerator, such that the created ground state molecules are magnetically trapped. The Stark interaction in the ground state is rather weak, therefore the Stark decelerator can be used to decelerate the next pulse of metastable NH radicals without affecting the trapping potential for ground state NH molecules. A number of prerequisites for the successful implementation of this accumulation scheme have already been experimentally demonstrated. The hitherto unobserved $A\,^3\Pi \;\leftarrow\; a\,^1\Delta$ transition was found and characterized [90], and in a preliminary deceleration experiment, a beam of metastable NH radicals was Stark decelerated from 550 m/s to 330 m/s [42]. It has been shown in chapter 2 of this thesis that it is experimentally possible to produce intense packets of NH radicals, and that these molecules can be decelerated and trapped electrostatically.

For the implementation of the reloading scheme and for the loading of molecules in a magnetic trap in general, the electrostatic trapping of NH is not required. To be able to trap the molecules in a magnetic trap, it is sufficient to bring the molecules to a standstill on a loading slope, just before they are optically pumped to the magnetically trapped $X\,^3\Sigma^-$ ground state. In the previous section it has been shown that the condition to design electrodes that can create both a trapping potential and an optimal loading potential can pose difficulties. The combination of electric and magnetic fields can be used to uncouple the loading of a trap and the trapping itself. In this section, two designs that combine an electric loading potential with a magnetic trapping potential are briefly discussed. In the second part of the section, trajectory calculations are presented on the loading of a magnetic trap that illustrate the possibilities to achieve phase-space matching between the decelerator and trap if the loading and trapping fields are uncoupled. As an outlook, experiments are shown that demonstrate the trapping of metastable NH molecules at a temperature

of 2 mK.

7.3.1 Magnetic trap designs

To achieve the deceleration of NH to a standstill, we replaced the last 7 stages of the decelerator by 9 individually designed and shaped electrode pairs of non-magnetic steel (1.4404). The shapes of these pairs and the distances be-
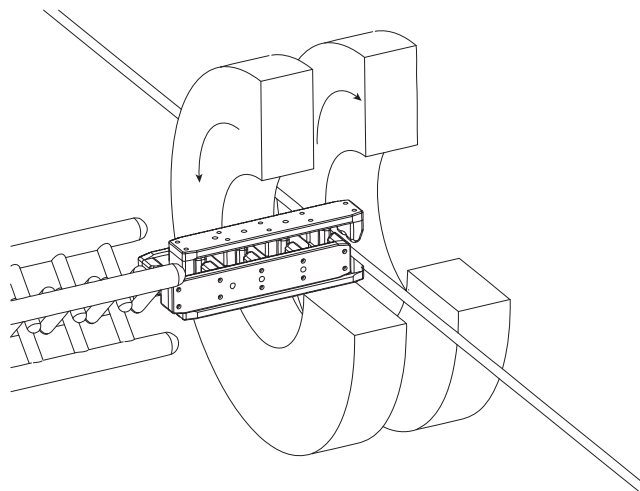

Figure 7.11: Schematic representation of 9 individually designed last 9 stages of the decelerator and two copper coils in anti-Helmholtz configuration that create a magnetic trapping potential. The arrows indicate the direction of the current through the coils.

tween each adjacent pair are chosen such that transversal overfocusing of the molecular packet is avoided. The last electrode pair is placed behind the point where the molecules can be optically excited and detected, as can be seen in figure 7.11. This allows to not only decelerate the molecules, but also bring them to a complete standstill at the detection point. Two copper coils of 16 turns each and with an inner diameter of 38 mm (outer diameter 85 mm) are placed 25 mm apart, centered around the detection point. The large inner diameter of the two coils of the electromagnet trap leaves enough space for the compact extension of the Stark decelerator inside the coils. A magnetic trapping potential is created by a 800 A current through the coils. The gradient of the magnetic field is measured to be ∼520 and ∼290 Gauss/cm in the longitudinal and transversal direction, respectively, as is shown in figure 7.12.

An interesting alternative to the magnetic trapping using large copper coils is the use of permanent magnets to construct a more compact, deeper magnetic trap. As was discussed in chapter 3, such permanent magnets can produce
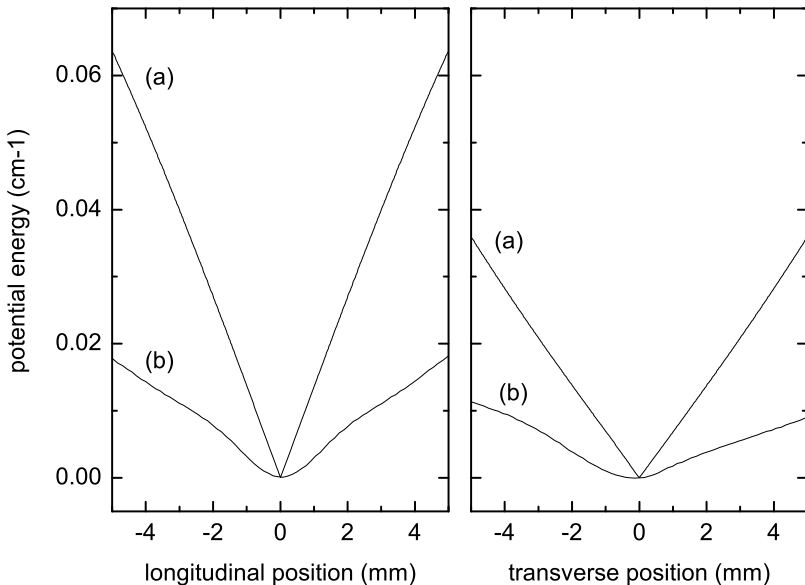
Figure 7.12: Longitudinal (left panel) and transverse (right panel) trap potential for NH ($a\,^1\Delta$) of the permanent magnet trap (a) and the electromagnet trap (b).

magnetic fields on the order of a Tesla. In that chapter, it was shown that a cylindrical permanent magnetic disc or small magnetic cubes placed in checkerboard fashion, can be used to create a strong reflection potential for molecules. Here, a trap design consisting of two permanent ring magnets, that creates a 3-dimensional trapping potential, is presented. The loading of slow molecules into the trap is achieved by applying an additional electric potential. The basics of this idea were also implemented in experiments by Ye and co-workers at JILA [75].

Figure 7.13 shows a design of two permanent magnets embedded in two non-magnetic steel (1.4404) electrodes. The two NdFeB (N50) ring magnets have an inner diameter of 40 mm, an outer diameter of 80 mm, and are placed 16 mm apart. The magnets (IBS Magnet, Berlin) have a remanence of 1.44 T, and create a magnetic potential well in the center with a field gradient of 1000 Gauss/cm and 1800 Gausss/cm in the radial direction and on the axis of the molecular beam, respectively. These magnetic fields correspond to a potential depth of $\sim$0.1 cm^{-1} for NH ($a\,^1\Delta$) molecules on the axis of the molecular beam. Figure 7.12 shows that the gradients of the potential of the permanent
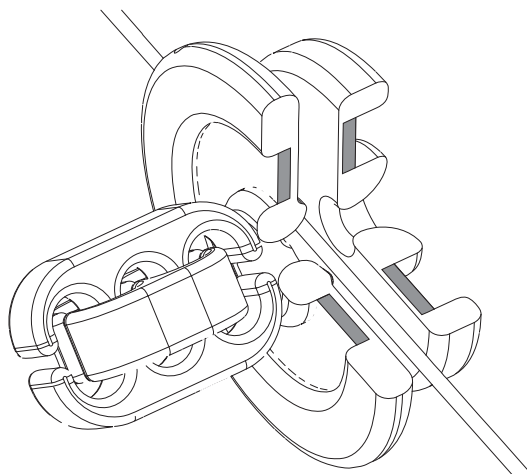
Figure 7.13: Schematic drawing of the permanent magnet trap design. Shown are the last 7 stages of the decelerator (left) and two permanent ring magnets (grey), that are embedded in non-magnetic steel electrodes. The electrodes have different outer diameters for technical reasons.

magnet trap are a factor of $\sim$3.5 higher than the gradient of the potential created by the electromagnetic coils. The electric loading potential in this coordinate for the molecules has to be considerably stronger than the continuously present magnetic trapping potential to be able to bring the molecules to a standstill. When a voltage of +20 kV and -20 kV is applied to the electrodes that are 10 mm apart, a loading potential for the molecules with a height of $\sim$0.5 cm^{-1} is created with a maximum in the center between the electrodes. At the maximum, the slope of the potential - that determines the force on the molecules - is zero and molecules can not be decelerated. To create a loading potential that allows for deceleration of the molecules to a velocity of zero in the center of the trap, the center between the electrodes is placed 2 mm behind the center of the magnetic trapping potential and the detection laser, as shown in figure 7.13.

The longitudinal and transverse trap acceptances of both trap designs are sketched in figure 7.14. The difference in magnetic field gradient as illustrated in figure 7.12 is also reflected here. The acceptance of the permanent magnet trap ((c),(d)) for NH ($a^1\Delta$) is compressed in space with respect to the acceptance of the electromagnet trap. As a reference, the phase-space acceptance of the electrostatic trap from section 7.2 is also shown ((e),(f)). The electrostatic trap has an even larger gradient and can confine molecules up to an energy of 0.3 cm^{-1}. The presence of different electrodes, indicated by the dashed lines, limits the trap depth of both magnetic traps even further to 0.035
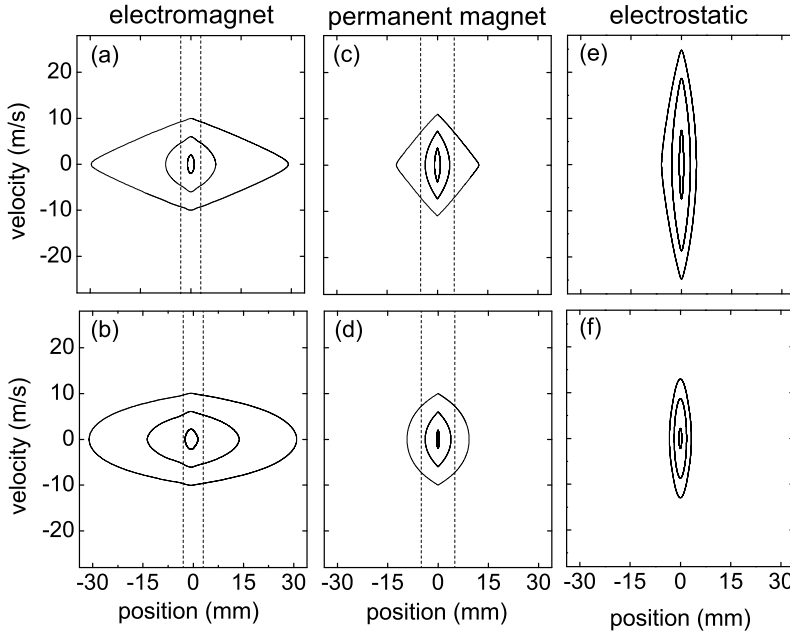
Figure 7.14: Longitudinal/transverse trap acceptance of the electromagnet trap(a)/(b) and the permanent magnet trap (c)/(d) for NH ($a\,^1\Delta$). As a comparison, the trap acceptance of the electrostatic trap as presented in section 7.2 is plotted on the same scale (e)/(f).

and 0.007 cm^{-1} for the permanent magnet trap and the electromagnet trap, respectively.

7.3.2 Permanent magnet trap

To directly compare the loading of a magnetic trap with the loading of an electrostatic trap as described extensively in section 7.2, trajectory calculations on the loading sequence of the permanent magnet trap are presented. The combined electric and magnetic potential energy of the NH molecules is plotted in the upper panel of figure 7.15. For the calculation of the used potentials the interaction of the molecules with the electric and magnetic field was treated independently. In this figure, the calculated phase-space distributions for the loading of NH ($a\,^1\Delta$) molecules into the designed magnetic trap are shown. Molecules exit the last stage of the decelerator with a mean velocity of 18 m/s

Figure 7.15: Potential energy for NH ($a\,^1\Delta$) molecules during the trap loading of the permanent magnet trap and the corresponding simulated longitudinal (middle) and transversal (bottom) phase-space distributions at various stages of the trap loading process.
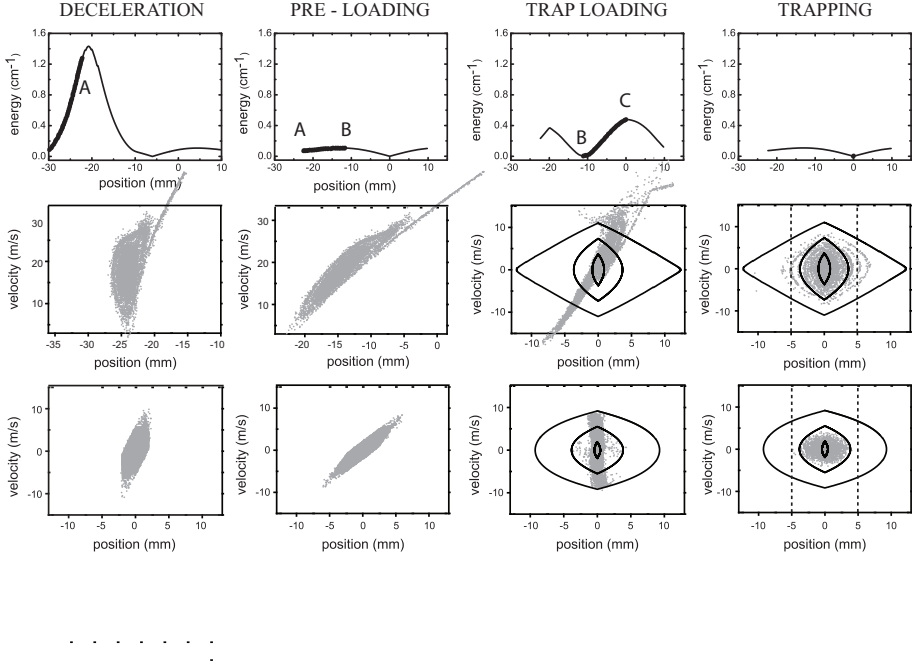
and a velocity spread of 7 m/s at time A. Similar to the loading sequence presented in figure 7.4, the electric fields are switched off for 500 μs from this moment on and the molecules enter a free flight section from time A to B. The permanent magnet trap can obviously not be switched off and molecules still experience the relatively weak potential from the magnetic rings during these 500 μs. At time B, the molecules enter the electric loading field. During this loading, molecules also experience a magnetic potential from the permanent magnets. This combined electric and magnetic loading potential has a maximum only 1 mm behind the trap center, causing molecules that are too far ahead to accelerate again. As discussed earlier in section 7.2, the included free flight section before the loading allows the packet to spread out in all directions. It is shown in the figure that this causes a suboptimal phase-space overlap between the molecular packet and the trap acceptance. In the transversal directions however, the spreading out can be compensated by the transversely symmetric loading potential. The dimensions of the two electrodes are chosen such that satisfactory phase-space matching with the transversal trap accep-

tance is obtained. The presence of one of the electrodes at about 5 mm from the trap center limits the trap acceptance as plotted in figures 7.14 and 7.15 to the size as shown by the trajectory calculations and the dashed lines. In the trap, 20 % of the molecules that exit the decelerator can be confined at a temperature of 6 mK.

In experiments, however, the assumption that molecules can be transferred from an electric field to a magnetic field without any losses, fails. It was already discussed in section 2.1 that NH molecules that exit the Stark decelerator all populate the electrically low-field seeking state $|M|=2$. If these molecules enter an additional magnetic field, this level is split once more and 50 % of the molecules will actually be expelled from the trap. These losses are an intrinsic limitation for the loading of Stark-decelerated molecules into magnetic traps. As a consequence, the efficiency of 20 % for the loading of the permanent magnet trap as given above has to be reduced by a factor of two.

7.3.3 Conclusion and outlook

The combination of electric trap loading of Stark-decelerated molecules and magnetic trapping potentials has the advantage over the pure electric case that both can to a certain extent be approached independently. Trajectory calculations show that this can result in better transversal phase-space matching of the molecular packet with the trap acceptance. Due to the inclusion of a free flight section in the loading process, however, proper matching can not be achieved in the longitudinal direction. Another difficulty in the design of magnetic traps is that it is problematic to achieve strong trapping potentials. The acceptance of these traps is therefore lower than the acceptance of the electric quadrupole trap presented in section 7.2.

The prospect of accumulating multiple packets of ground state NH molecules into a trap has triggered us to design and build the electromagnet trap as shown above. Figure 7.16 shows a time-of-flight profile of NH $(a\,^1\Delta)$ molecules, measured in the center of the electromagnet trap. The NH $(a\,^1\Delta)$ molecules were detected background free via the spin-forbidden $A\,^3\Pi \leftarrow a\,^1\Delta$ transition as described in section 2.3.4. The time-of-flight curve shows that molecules are decelerated effectively to 0 m/s by the individually designed deceleration electrodes, sketched in figure 7.11. At the moment that the packet of molecules arrives with a mean velocity of zero in the trap center, 6.4 ms after its production, all electric fields are switched off and molecules in the appropriate quantum state are confined in the magnetic trap with a depth of ~ 2 mK. It can be seen from figure 7.16 that the magnetic trapping potential is too shallow to confine all the molecules that arrive in the trap center. The $A\,^3\Pi \leftarrow a\,^1\Delta$ transition that was used for the (background free) detection, optically transfers molecules to the $X\,^3\Sigma^-$ ground state. We could experimentally show that of the molecules excited from the $a\,^1\Delta$(v=0,J=2) level to the $A\,^3\Pi$(v=0,N=1,J=1) level about 65 % decay to the $X\,^3\Sigma^-$(v=0,N=0,J=1) level, which is the lowest
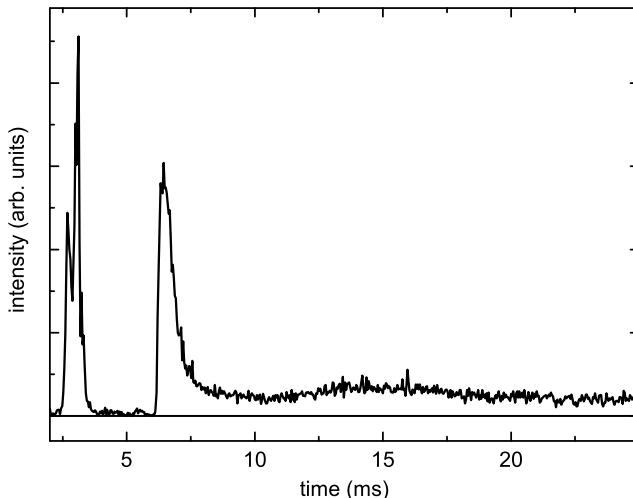
Figure 7.16: Time-of-flight profile measured inside the magnetic trap. Molecules are decelerated to zero velocity on an electric potential and confined in the magnetic trap.

rotational level of the electronic groundstate of NH. In principle, those ground state molecules are also trapped by the same magnetic fields. The detection of those ground state molecules, however, has been proven to be more challenging, mainly because LIF detection via the electronically excited $A\,^3\Pi$ state is not background free. Current research is focused on a sensitive detection of the trapped ground state molecules. Alternatively, the implementation of the permanent magnet trap in the experiment might be a suitable way to improve the trap acceptance and to increase the number of molecules that can be trapped.

7.4 Conclusions

In this chapter, the loading of electrostatic and magnetic traps was discussed. Phase-space distributions following from trajectory calculations are presented to differentiate between the trap loading sequences and to illustrate the problems that can occur during the loading. A new electric quadrupole trap design was tested experimentally and this design resulted in 2.2 times more trapped molecules compared to the best possible loading in the old trap design. In simulations this increase was not quantatively reproduced. The outcome of those simulations could, on the other hand, accurately explain many observed

effects. The oscillations, for instance, that occur in the time-of-flight profile of almost any of our trap experiments, can be explained by overfocusing, mainly in the transverse directions. This overfocusing in one or more directions, and missing radial symmetry of the trapping potential in general has hindered the achievement of an ideal loading efficiency of 100 % until now. In order to reach this limit, new (symmetric) electrode designs are needed that can create both a trapping and a loading potential and ensure phase-space matching of the molecular packet as it exits the Stark decelerator onto the trap.

Summarizing, there are several issues to resolve before optimal trap loading can be achieved in the laboratory. On the other hand, the efficiency reached in the current experiments is already in the 25-30 % range. That implies that the maximal gain of any improved design is a factor of 3 to 4 in the absolute number of trapped molecules. Depending on the planned experiments with the trapped cloud of cold molecules, practical choices have to be made. If the experiment is steered to explore (ultra)cold phenomena, cold molecules are required; the experimentalist will have to focus to load molecules within the most inner contours of the acceptance of a trap and might have to compromise in the absolute number of molecules, due to losses during the loading process. In other studies, like in the lifetime experiments presented in this thesis, the temperature is a less important parameter, and a large absolute number of molecules is desired. In this case there is no longer a need to bring molecules to a standstill exactly in the center of the trap, and also faster molecules can be loaded in. For this type of experiments the best practical choice might be to design a compact conventional quadrupole trap and to give priority to the implementation of a steep loading potential. In that case, molecules can bridge the free flight section still relatively fast and transverse losses can be minimized.

An important alternative to electrostatic trapping is the confinement of molecules with magnetic fields. In this chapter, two designs were presented that combine an electric loading potential and a magnetic trapping potential. This combination allows for more freedom in the design in order to achieve good 6-dimensional phase-space matching. It was experimentally shown that this already resulted in the confinement of $\sim$2 mK cold packets of NH molecules. If current experimental challenges can be met, this combination of electric loading and magnetic trapping even allows for the confinement of an order of magnitude more NH molecules, via a promising accumulation scheme.

Bibliography

[1] G. Scoles, Editor, *Atomic and molecular beam methods*, Volume 1 & 2 (New York, NY, USA, 1988).

[2] W. Gerlach and O. Stern, *Der experimentelle Nachweis der Richtungsquantelung im Magnetfeld*, Zeitschrift für Physik **9**, 349 (1922).

[3] H. Friedburg and W. Paul, *Optische Abbildung mit neutralen Atomen*, Die Naturwissenschaften **38**, 159 (1951).

[4] H. G. Bennewitz and W. Paul, *Eine Methode zur Bestimmung von Kernmomenten mit fokussiertem Atomstrahl*, Zeitschrift für Physik **139**, 489 (1954).

[5] H. G. Bennewitz, W. Paul and C. Schlier, *Fokussierung polarer Moleküle*, Zeitschrift für Physik **141**, 6 (1955).

[6] Y. T. Lee, *Nobel Lecture: Molecular beam studies of elementary chemical processes*, Angew. Chem. **26**, 939 (1987).

[7] S. Stolte, *Reactive scattering studies on oriented molecules*, Berichte der Bunsen Gesellschaft-Phys. Chem. Chem. Phys. **86**, 413 (1982).

[8] R. T. Skodje, D. Skouteris, D. E. Manolopoulos, S. H. Lee, F. Dong and K. Liu, *Observation of a transition state resonance in the integral cross section of the F+HD reaction*, J. Chem. Phys. **112**, 4536 (2000).

[9] M. H. Qiu, Z. F. Ren, L. Che, D. X. Dai, S. A. Harich, X. Y. Wang, X. M. Yang, C. X. Xu, D. Q. Xie, M. Gustafsson, R. T. Skodje, Z. G. Sun and D. H. Zhang, *Observation of Feshbach resonances in the F+H$_2$ →HF+H reaction*, Science **311**, 1440 (2006).

[10] J. J. Gilijamse, S. Hoekstra, S. Y. T. van de Meerakker, G. C. Groenenboom and G. Meijer, *Near-threshold inelastic collisions using molecular beams with a tunable velocity*, Science **313**, 1617 (2006).

[11] S. Y. T. van de Meerakker and G. Meijer, *Collision experiments with Stark-decelerated beams*, Faraday Discuss. **142** (to be published).

[12] J. van Veldhoven, J. Küpper, H. L. Bethlem, B. Sartakov, A. J. A. van Roij and G. Meijer, *Decelerated molecular beams for high-resolution spectroscopy*, Eur. Phys. J. D **31**, 337 (2004).

[13] E. R. Hudson, H. J. Lewandowski, B. C. Sawyer and J. Ye, *Cold molecule spectroscopy for constraining the evolution of the fine structure constant*, Phys. Rev. Lett. **96**, 143004 (2006).

[14] H. L. Bethlem, M. Kajita, B. Sartakov, G. Meijer and W. Ubachs, *Prospects for precision measurements on ammonia molecules in a fountain*, Eur. J. Phys. ST **163**, 55 (2008).

[15] J. J. Hudson, B. E. Sauer, M. R. Tarbutt and E. A. Hinds, *Measurement of the electron electric dipole moment using YbF molecules*, Phys. Rev. Lett. **89**, 023003 (2002).

[16] R. V. Krems, *Molecules near absolute zero and external field control of atomic and molecular dynamics*, Int. Rev. Phys. Chem. **24**, 99 (2005).

[17] J. D. Weinstein, R. deCarvalho, T. Guillet, B. Friedrich and J. M. Doyle, *Magnetic trapping of calcium monohydride molecules at millikelvin temperatures*, Nature **395**, 148 (1998).

[18] T. Takekoshi, B. M. Patterson and R. J. Knize, *Observation of optically trapped cold cesium molecules*, Phys. Rev. Lett. **81**, 5105 (1998).

[19] M. Greiner, C. A. Regal and D. S. Jin, *Emergence of a molecular Bose-Einstein condensate from a Fermi gas*, Nature **426**, 537 (2003).

[20] J. Doyle, B. Friedrich, R. V. Krems and F. Masnou-Seeuws, *Quo vadis, cold molecules?*, Eur. Phys. J. D **31**, 149 (2004).

[21] W. Ketterle and N. J. V. Druten, *Evaporative cooling of trapped atoms*, Adv. Atom. Mol. Opt. Phys. **37**, 181 (1996).

[22] G. Modugno, G. Ferrari, G. Roati, R. J. Brecha, A. Simoni and M. Inguscio, *Bose-einstein condensation of potassium atoms by sympathetic cooling*, Science **294**, 1320 (2001).

[23] M. A. Baranov, M. S. Mar'enko, V. S. Rychkov and G. V. Shlyapnikov, *Superfluid pairing in a polarized dipolar Fermi gas*, Phys. Rev. A **66**, 013606 (2002).

[24] J. Stuhler, A. Griesmaier, T. Koch, M. Fattori, T. Pfau, S. Giovanazzi, P. Pedri and L. Santos, *Observation of dipole-dipole interaction in a degenerate quantum gas*, Phys. Rev. Lett. **95**, 150406 (2005).

[25] M. Baranov, L. Dobrek, K. Góral, L. Santos and M. Lewenstein, *Ultracold dipolar gases - a challenge for experiments and theory*, Phys. Scr. **T102**, 74 (2002).

[26] A. André, D. DeMille, J. M. Doyle, M. D. Lukin, S. E. Maxwell, P. Rabl, R. J. Schoelkopf and P. Zoller, *A coherent all-electrical interface between polar molecules and mesoscopic superconducting resonators*, Nat. Phys. **2**, 636 (2006).

[27] W. D. Phillips, *Nobel Lecture: Laser cooling and trapping of neutral atoms*, Rev. Mod. Phys. **70**, 721 (1998).

[28] T. Köhler, K. Goral and P. S. Julienne, *Production of cold molecules via magnetically tunable Feshbach resonances*, Rev. Mod. Phys. **78**, 1311 (2006).

[29] K. Ni, S. Ospelkaus, M. H. G. de Miranda, A. Peer, B. Neyenhuis, J. J. Zirbel, S. Kotochigova, P. S. Julienne, D. S. Jin and J. Ye, *A high phase-space-density gas of polar molecules*, Science **322**, 231 (2008).

[30] M. Drabbels and A. M. Wodtke, *The determination of the infrared radiative lifetimes of a vibrationally excited neutral molecule using stimulated-emission-pumping, molecular-beam time-of-flight*, J. Chem. Phys. **106**, 3024 (1997).

[31] R. T. Jongma, G. Berden, T. Rasing, H. Zacharias and G. Meijer, *Scattering of vibrationally and electronically excited CO molecules from a LiF(100) surface*, Chem. Phys. Lett. **273**, 147 (1997).

[32] R. T. Jongma, G. Berden and G. Meijer, *State-specific lifetime determination of the $a^3\Pi$ state in CO*, J. Chem. Phys. **107**, 7034 (1997).

[33] S. Y. T. van de Meerakker, N. Vanhaecke, M. P. J. van der Loo, G. C. Groenenboom and G. Meijer, *Direct measurement of the radiative lifetime of vibrationally excited OH radicals*, Phys. Rev. Lett. **95**, 013003 (2005).

[34] W. C. Campbell, G. C. Groenenboom, H. I. Lu, E. Tsikata and J. M. Doyle, *Time-domain measurement of spontaneous vibrational decay of magnetically trapped NH*, Phys. Rev. Lett. **100**, 083003 (2008).

[35] R. Golub, *On decelerating molecules*, PhD Thesis, M.I.T. (1967).

[36] E. E. A. Bromberg, *Acceleration and alternate-gradient focussing of neutral polar diatomic molecules*, PhD Thesis, University of Chicago (1968).

[37] H. L. Bethlem, G. Berden and G. Meijer, *Decelerating neutral dipolar molecules*, Phys. Rev. Lett. **83**, 1558 (1999).

[38] H. L. Bethlem, G. Berden, F. M. H. Crompvoets, R. T. Jongma, A. J. A. van Roij and G. Meijer, *Electrostatic trapping of ammonia molecules*, Nature **406**, 491 (2000).

[39] J. R. Bochinski, E. R. Hudson, H. J. Lewandowski, G. Meijer and J. Ye, *Phase space manipulation of cold free radical OH molecules*, Phys. Rev. Lett. **91**, 243001 (2003).

[40] E. R. Hudson, C. Ticknor, B. C. Sawyer, C. A. Taatjes, H. J. Lewandowski, J. R. Bochinski, J. L. Bohn and J. Ye, *Production of cold formaldehyde molecules for study and control of chemical reaction dynamics with hydroxyl radicals*, Phys. Rev. A **73**, 063404 (2006).

[41] T. E. Jung, S. and C. Lisdat, *Cold atoms and molecules from fragmentation of decelerated SO_2*, Phys. Rev. A **74**, 040701 (2006).

[42] S. Y. T. van de Meerakker, I. Labazan, S. Hoekstra, J. Küpper and G. Meijer, *Production and deceleration of a pulsed beam of metastable $NH(a^1\Delta)$ radicals*, J. Phys. B **39**, 1077 (2006).

[43] S. Hoekstra, J. J. Gilijamse, B. Sartakov, N. Vanhaecke, L. Scharfenberg, S. Y. T. van de Meerakker and G. Meijer, *Optical pumping of trapped neutral molecules by blackbody radiation*, Phys. Rev. Lett. **98**, 133001 (2007).

[44] H. L. Bethlem and G. Meijer, *Production and application of translationally cold molecules*, Int. Rev. Phys. Chem. **22**, 73 (2003).

[45] C. E. Heiner, H. L. Bethlem and G. Meijer, *Molecular beams with a tunable velocity*, Phys. Chem. Chem. Phys. **8**, 2666 (2006).

[46] S. Y. T. van de Meerakker, H. L. Bethlem and G. Meijer, *Taming molecular beams*, Nat. Phys. **4**, 595 (2008).

[47] S. Y. T. van de Meerakker, P. H. M. Smeets, N. Vanhaecke, R. T. Jongma and G. Meijer, *Deceleration and electrostatic trapping of OH radicals*, Phys. Rev. Lett. **94**, 023004 (2005).

[48] B. C. Sawyer, B. L. Lev, E. R. Hudson, B. K. Stuhl, M. Lara, J. L. Bohn and J. Ye, *Magnetoelectrostatic trapping of ground state OH molecules*, Phys. Rev. Lett. **98**, 253002 (2007).

[49] D. Auerbach, E. E. A. Bromberg and L. Wharton, *Alternate-gradient focusing of molecular beams*, J. Chem. Phys. **45**, 2160 (1966).

[50] M. R. Tarbutt, H. L. Bethlem, J. J. Hudson, V. L. Ryabov, V. A. Ryzhov, B. E. Sauer, G. Meijer and E. A. Hinds, *Slowing heavy, ground-state molecules using an alternating gradient decelerator*, Phys. Rev. Lett. **92**, 173002 (2004).

[51] H. L. Bethlem, A. J. A. van Roij, R. T. Jongma and G. Meijer, *Alternate gradient focusing and deceleration of a molecular beam*, Phys. Rev. Lett. **88**, 133003 (2002).

[52] K. Wohlfart, F. Grätz, F. Filsinger, H. Haak, G. Meijer and J. Küpper, *Alternating-gradient focusing and deceleration of large molecules*, Phys. Rev. A **77**, 031404 (2008).

[53] J. van Veldhoven, H. L. Bethlem and G. Meijer, *AC electric trap for ground-state molecules*, Phys. Rev. Lett. **94**, 083001 (2005).

[54] S. A. Schulz, H. L. Bethlem, J. van Veldhoven, J. Küpper, H. Conrad and G. Meijer, *Microstructured switchable mirror for polar molecules*, Phys. Rev. Lett. **93**, 020406 (2004).

[55] S. A. Meek, H. L. Bethlem, H. Conrad, and G. Meijer, *Trapping molecules on a chip in traveling potential wells*, Phys. Rev. Lett. **100**, 153003 (2008).

[56] N. Vanhaecke, U. Meier, M. Andrist, B. H. Meier and F. Merkt, *Multistage Zeeman deceleration of hydrogen atoms*, Phys. Rev. A **75**, 031402 (2007).

[57] S. D. Hogan, D. Sprecher, M. Andrist, N. Vanhaecke and F. Merkt, *Zeeman deceleration of H and D*, Phys. Rev. A **76**, 023412 (2007).

[58] E. Narevicius, C. G. Parthey, A. Libson, J. Narevicius, I. Chavez, U. Even and M. G. Raizen, *An atomic coilgun: using pulsed magnetic fields to slow a supersonic beam*, New J. Phys. **9**, 358 (2007).

[59] E. Narevicius, A. Libson, C. G. Parthey, I. Chavez, J. Narevicius, U. Even and M. G. Raizen, *Stopping supersonic oxygen with a series of pulsed electromagnetic coils: A molecular coilgun*, Phys. Rev. A **77**, 051401 (2008).

[60] S. D. Hogan, A. W. Wiederkehr, H. Schmut and F. Merkt, *Magnetic trapping of hydrogen after multistage Zeeman deceleration*, Phys. Rev. Lett. **101** (2008).

[61] Y. Yamakita, S. R. Procter, A. L. Goodgame, T. P. Softley and F. Merkt, *Deflection and deceleration of hydrogen Rydberg molecules in inhomogeneous electric fields*, J. Chem. Phys. **121**, 1419 (2004).

[62] S. D. Hogan and F. Merkt, *Demonstration of three-dimensional electrostatic trapping of state-selected Rydberg atoms*, Phys. Rev. Lett. **100**, 043001 (2008).

[63] R. Fulton, A. I. Bishop, M. N. Shneider and P. F. Barker, *Controlling the motion of cold molecules with deep periodic optical potentials*, Nat. Phys. **2**, 465 (2006).

[64] P. F. Barker and M. N. Shneider, *Slowing molecules by optical microlinear deceleration*, Phys. Rev. A **66**, 065402 (2002).

[65] R. Fulton, A. I. Bishop and P. F. Barker, *Optical Stark decelerator for molecules*, Phys. Rev. Lett. **93**, 243004 (2004).

[66] M. Gupta and D. Herschbach, *A mechanical means to produce intense beams of slow molecules*, J. Phys. Chem. A **103**, 10670 (1999).

[67] H. J. Loesch and N. Liu, *Kinematic slowing of molecules formed by reactive collisions*, Phys. Rev. Lett. **98**, 103002 (2007).

[68] M. S. Elioff, J. J. Valentini and D. W. Chandler, *Subkelvin cooling NO molecules via "billiard-like" collisions with argon*, Science **302**, 1940 (2003).

[69] S. A. Rangwala, T. Junglen, T. Rieger, P. W. H. Pinkse and G. Rempe, *Continuous source of translationally cold dipolar molecules*, Phys. Rev. A **67**, 043406 (2003).

[70] L. D. van Buuren, C. Sommer, M. Motsch, S. Pohle, M. Schenk, J. Bayerl, P. W. H. Pinkse and G. Rempe, *Electrostatic extraction of cold molecules from a cryogenic reservoir*, Phys. Rev. Lett. **102**, 033001 (2009).

[71] A. V. Avdeenkov and J. L. Bohn, *Collisional dynamics of ultracold OH molecules in an electrostatic field*, Phys. Rev. A **66**, 052718 (2002).

[72] M. Lara, J. L. Bohn, D. Potter, P. Soldanand and J. M. Hutson, *Ultracold Rb-OH collisions and prospects for sympathetic cooling*, Phys. Rev. Lett. **97**, 183201 (2006).

[73] M. Kajita, *Infrared frequency standard based on magnetically trapped NH molecules*, Phys. Rev. A **74**, 035403 (2006).

[74] S. Y. T. van de Meerakker, R. T. Jongma, H. L. Bethlem and G. Meijer, *Accumulating NH radicals in a magnetic trap*, Phys. Rev. A **64**, 041401 (2001).

[75] B. C. Sawyer, B. K. Stuhl, D. Wang, M. Yeo and J. Ye, *Molecular beam collisions with a magnetically trapped target*, Phys. Rev. Lett. **101**, 203203 (2008).

[76] G. Herzberg, *Molecular spectra and molecular structure. Volume I: Spectra of diatomic molecules. Second edition* (Van Nostrand Reinhold, 1950).

[77] K. Gubbels, *Dynamics of stark acceleration/deceleration: Molecules riding waves*, Master's Thesis, Radboud Universiteit Nijmegen (2006) .

[78] S. Y. T. van de Meerakker, *Deceleration and electrostatic trapping of OH radicals*, PhD Thesis, Radboud Universiteit Nijmegen (2006).

[79] R. T. Jongma, *Molecular beam experiments and scattering studies with state-selected metastable CO*, Ph.D. thesis, Katholieke Universiteit Nijmegen (1997).

[80] H. L. Bethlem, *Deceleration and trapping of polar molecules using time-varying electric fields*, Ph.D. thesis, Katholieke Universiteit Nijmegen (2002).

[81] W. Hack and A. Wilms, *Elementary reactions of imidogen($a^1\Delta$) with atoms and diatomic molecules*, J. Chem. Phys. **93**, 3540 (1989).

[82] R. D. Kenner, F. Rohrer and F. Stuhl, *Generation of NH($a^1\Delta$) in the 193 nm photolysis of ammonia*, J. Chem. Phys. **86**, 2036 (1986).

[83] F. Rohrer and F. Stuhl, *The 193 (and 248) nm photolysis of HN$_3$: Formation and internal energy distributions of the NH ($a^1\Delta, b^1\Sigma^+, A^3\Pi, and\ c^1\Pi$) states*, J. Chem. Phys. **88**, 4788 (1988).

[84] P. C. Zieger, *Produktion und Fokussierung eines metastabilen NH-Molekülarstrahls*, Master's Thesis, FU Berlin (2007) .

[85] S. Y. T. van de Meerakker, N. Vanhaecke, H. L. Bethlem and G. Meijer, *Transverse stability in a Stark decelerator*, Phys. Rev. A **73**, 023401 (2006).

[86] L. Scharfenberg, H. Haak, G. Meijer and S. Y. T. van de Meerakker, *Operation of a Stark decelerator with optimum acceptance*, Phys. Rev. A **79**, 023410 (2009).

[87] S. Y. T. van de Meerakker, N. Vanhaecke, H. L. Bethlem and G. Meijer, *Higher-order resonances in a Stark decelerator*, Phys. Rev. A **71** (2005).

[88] S. Y. T. van de Meerakker, N. Vanhaecke and G. Meijer, *Stark deceleration and trapping of OH radicals*, Ann. Rev. Phys. Chem. **57**, 159 (2006).

[89] J. Küpper, H. Junkes and U. Hoppe, *KouDA: A general purpose data acquistion system* (2003–2008), http://kouda.cold-molecules.info.

[90] S. Y. T. van de Meerakker, B. G. Sartakov, A. P. Mosk, R. T. Jongma and G. Meijer, *Optical pumping of metastable NH radicals into the paramagnetic ground state*, Phys. Rev. A **68**, 032508 (2003).

[91] I. Rechenberg, *Kybernetische Lösungsansteuerung einer experimentellen Forschungsaufgabe*, in *Annual Conference of the WGLR* (Berlin, 1964), english translation: B. F. Toms: *Cybernetic solution path of an experimental problem*, Royal Aircraft Establishment, Farnborough p. Library Translation 1122 (1965). Reprinted in D. B. Fogel: *Evolutionary Computing: The Fossil Records*, IEEE Press, 1998.

[92] H.-P. Schwefel, *Evolution and optimum seeking*, The Sixth Generation Computer Technology Series (New York, NY, USA, 1993).

[93] L. J. Fogel, A. J. Owens and M. J. Walsh, in *Artificial intelligence through a simulation of evolution*, A. Callahan, M. Maxfield and L. J. Fogel *Biophysics and cybernetic systems*, 131 (Spartan, Washington, DC, USA, 1965).

[94] J. H. Holland, *Adaption in natural and artificial systems* (University of Michigan Press, Ann Arbor, MI, USA, 1975).

[95] A. E. Eiben and J. E. Smith, *Introduction to evolutionary computing*, Natural Computing Series (Berlin, 2003).

[96] M. Keijzer, J. J. Merelo, G. Romero and M. Schoenauer, *Evolving objects: A general purpose evolutionary computation library*, Art. Evol. **2310**, 231 (2002).

[97] H. L. Bethlem, F. M. H. Crompvoets, R. T. Jongma, S. Y. T. van de Meerakker and G. Meijer, *Deceleration and trapping of ammonia using time-varying electric fields*, Phys. Rev. A **65**, 053416 (2002).

[98] J. Reuss, *State selection by nonoptical methods*, Chapter 11 from [1], 276.

[99] H. J. Metcalf and P. van der Straten, *Laser cooling and trapping* (New York, NY, USA, 1999).

[100] G. Berden, R. Peeters and G. Meijer, *Cavity ring-down spectroscopy: Experimental schems and applications*, Int. Rev. Phys. Chem. **19**, 565 (2000).

[101] G. H. Dieke and H. M. Crosswhite, *The ultraviolet bands of OH - fundamental data*, J. Quant. Spectr. Rad. Tr. **2**, 97 (1962).

[102] H. Naus, I. H. M. van Stokkum, W. Hogervorst and W. Ubachs, *Quantitative analysis of decay transients applied to a multimode pulsed cavity ringdown experiment*, Appl. Opt. **40**, 4416 (2001).

[103] P. Zalicki and N. R. Zare, *Cavity Ringdown Spectroscopy for quantitative absorption measurements*, J. Chem. Phys. **102**, 2708 (1995).

[104] The value for σ of the $Q_1(1)$ transition in OH was taken from calculations by Boris Sartakov. Using a lifetime of 690 ns, σ was found to be $1.02 \cdot 10^{-13}$ cm^2. This is in agreement with the value from page 197 of reference [159], after correction of their value of A_{ji} by a factor of $1/10$.

[105] W. Gordy and R. L. Cook, *Microwave molecular spectra, page 445*, 3 Edition (Wiley-Interscience, 1984).

[106] J. D. Weinstein, R. deCarvalho, T. Guillet, B. Friedrich and J. M. Doyle, *Magnetic trapping of calcium monohydride molecules at millikelvin temperatures*, Nature **395**, 148 (1998).

[107] E. A. Hinds and I. G. Hughes, *Magnetic atom optics: mirrors, guides, traps, and chips for atoms*, J. Phys. D **32**, 119 (1999).

[108] G. I. Opat, S. J. Wark and A. Cimmino, *Electric and magnetic mirrors and gratings for slowly moving neutral atoms and molecules*, Appl. Phys. B **54**, 396 (1992).

[109] A. I. Sidorov, R. J. McLean, W. J. Rowlands, W. J. Lau, J. E. Murphy, M. Walkiewicz, G. I. Opat and P. Hannaford, *Specular reflection of cold caesium atoms from a magnetostatic mirror*, Quantum Semiclass. Opt. **8**, 713 (1996).

[110] C. D. J. Sinclair, J. A. Retter, E. A. Curtis, B. V. Hall, G. I. Llorent, S. Eriksson, B. E. Sauer and E. A. Hinds, *Cold atoms in videotape microtraps*, Eur. Phys. J. D **35**, 105 (2005).

[111] R. Gerritsma, S. Whitlock, T. Fernholz, H. Schlatter, J. A. Luigjes, J.-U. Thiele, J. B. Goedkoop and R. J. C. Spreeuw, *Lattice of microtraps for ultracold atoms based on patterned magnetic films*, Phys. Rev. A **76**, 033408 (2007).

[112] F. M. H. Crompvoets, R. T. Jongma, H. L. Bethlem, A. J. A. van Roij and G. Meijer, *Longitudinal focusing and cooling of a molecular beam*, Phys. Rev. Lett. **89**, 093004 (2002).

[113] R. D. Levine and R. B. Bernstein, Editor, *Molecular reaction dynamics and chemical reactivity* (Oxford Univ. Press, New York, NY, USA, 1987).

[114] T. P. Rakitzis, A. J. van den Brom and M. H. M. Janssen, *Directional dynamics in the photodissociation of oriented molecules*, Science **303**, 1852 (2004).

[115] X. Liu, J. J. Lin, S. Harich, G. C. Schatz and X. Yang, *A quantum state-resolved insertion reaction: $O(^1D) + H_2(J=0) \rightarrow OH(^2\Pi,v,N) + H(^2S)$*, Science **289**, 1536 (2000).

[116] S. A. Harich, D. X. Dai, C. C. Wang, X. M. Yang, S. D. Chao and R. T. Skodje, *Forward scattering due to slow-down of the intermediate in the $H+HD \to D+H_2$ reaction*, Nature **419**, 281 (2002).

[117] J. J. Lin, J. Zhou, W. Shiu and K. Liu, *State-specific correlation of coincident product pairs in the $F+CD_4$ reaction*, Science **300**, 966 (2003).

[118] J. J. van Leuken, J. Bulthuis, S. Stolte and J. G. Snijders, *Steric asymmetry in rotationally inelastic state-resolved NO-Ar collisions*, Chem. Rev. Lett. **260**, 595 (1996).

[119] R. N. Zare, *Laser control of chemical reactions*, Science **279**, 1875 (1998).

[120] M. C. van Beek, G. Berden, H. L. Bethlem and J. J. ter Meulen, *Molecular reorientation in collisions of OH plus Ar*, Phys. Rev. Lett. **86**, 4001 (2001).

[121] G. Hall, K. Liu, M. J. McAuliffe, C. F. Giese and W. R. Gentrey, *Pulsed molecular-beam study of state-to-state vibrational-excitation in $He+I_2$ collisions - energy-dependence of the $v=0 \to 1$ cross-section*, J. Chem. Phys. **78**, 5260 (1983).

[122] R. G. Macdonald and K. Liu, *State-to-state integral cross-sections for the inelastic-scattering of $CH(X^2\Pi)$ + He - rotational rainbow and orbital alignment*, J. Chem. Phys. **91**, 821 (1989).

[123] D. M. Sonnenfroh, R. G. Macdonald and K. Liu, *A crossed-beam study of the state-resolved integral cross-sections for the inelastic-scattering of $OH(X^2\Pi)$ with CO and N_2*, J. Chem. Phys. **94**, 5608 (1991).

[124] D. Skouteris, D. E. Manolopoulos, W. Bian, H. J. Werner, L. H. Lai and K. Liu, *van der Waals interactions in the Cl+HD reaction*, Science **286**, 1713 (1999).

[125] W. Shiu, J. J. Lin and K. Liu, *Reactive resonance in a polyatomic reaction*, Phys. Rev. Lett. **92**, 103201 (2004).

[126] R. C. Forrey, N. Balakrishnan, V. Kharchenko and A. Dalgarno, *Feshbach resonances in ultracold atom-diatom scattering*, Phys. Rev. A **58**, R2645 (1998).

[127] N. Balakrishnan, A. Dalgarno and R. C. Forrey, *Vibrational relaxation of CO by collisions with ^4He at ultracold temperatures*, J. Chem. Phys. **113**, 621 (2000).

[128] C. D. Ball and F. C. D. Lucia, *Direct measurement of rotationally inelastic cross sections at astrophysical and quantum collisional temperatures*, Phys. Rev. Lett. **81**, 305 (1998).

[129] I. R. Sims, J. L. Queffelec, A. Defrance, C. Rebrionrowe, D. Travers, B. R. Rowe and I. W. M. Smith, *Ultra-low temperature kinetics of neutral-neutral reactions - the reaction $CN+O_2$ down to 26 K*, J. Chem. Phys. **97**, 8798 (1992).

[130] P. Staanum, S. D. Kraft, J. Lange, R. Wester and M. Weidemüller, *Experimental investigation of ultracold atom-molecule collisions*, Phys. Rev. Lett. **96**, 023201 (2006).

[131] N. Zahzam, T. Vogt, M. Mudrich, D. Comparat and P. Pillet, *Atom-molecule collisions in an optically trapped gas*, Phys. Rev. Lett. **96**, 023202 (2006).

[132] L. T. Cowley, M. A. D. Fluendy and K. P. Lawley, *A radial disk velocity selector for molecular beams*, Rev. Sci. Instrum. **41**, 666 (1970).

[133] M. C. van Beek, J. J. ter Meulen and M. H. Alexander, *Rotationally inelastic collisions of $OH(X^2\Pi)+Ar$. I. State-to-state cross sections*, J. Chem. Phys. **113**, 628 (2000).

[134] M. C. van Beek, J. J. ter Meulen and M. H. Alexander, *Rotationally inelastic collisions of $OH(X^2\Pi)+Ar$. II. The effect of molecular orientation*, J. Chem. Phys. **113**, 637 (2000).

[135] M. H. Alexander, *Rotationally inelastic-collisions between a diatomic molecule in a $^2\Pi$ electronic state and a structureless target*, J. Chem. Phys. **76**, 5974 (1982).

[136] A. Einstein, *Quantum theory of radiation*, Physikalische Zeitschrift **18**, 121 (1917).

[137] A. McKellar, *Molecular lines from the lowest states of diatomic molecules composed of atoms probably present in interstellar space*, Publ. Dominion Astrophys. Observatory **7**, 251 (1941).

[138] A. A. Penzias and R. W. Wilson, *A measurement of excess antenna temperature at 4080mc/s*, Astrophys. J. **142**, 419 (1965).

[139] T. F. Gallagher and W. E. Cooke, *Interactions of blackbody radiation with atoms*, Phys. Rev. Lett. **42**, 835 (1979).

[140] R. C. Dunbar, *Kinetics of low-intensity infrared-laser photodissociation - the thermal-model and application of the Tolman theorem*, J. Chem. Phys. **95**, 2537 (1991).

[141] D. Tholmann, D. S. Tonner and T. B. McMahon, *Spontaneous unimolecular dissociation of small cluster ions, $(H_3O^+)L_n$ and $Cl^-(H_2O)_n(n = 2-4)$, under Fourier-transform ion-cyclotron resonance conditions*, J. Phys. Chem. **98**, 2002 (1994).

[142] U. Hechtfischer, Z. Amitay, P. Forck, M. Lange, J. Linkemann, M. Schmitt, U. Schramm, D. Schwalm, R. Wester, D. Zajfman and A. Wolf, *Near-threshold photodissociation of cold CH^+ in a storage ring*, Phys. Rev. Lett. **80**, 2809 (1998).

[143] A. V. Avdeenkov and J. L. Bohn, *Ultracold collisions of fermionic OD radicals*, Phys. Rev. A **71**, 022706 (2005).

[144] S. K. Tokunaga, J. O. Stack, J. J. Hudson, B. E. Sauer, E. A. Hinds and M. R. Tarbutt, *A supersonic beam of cold lithium hydride molecules*, J. Chem. Phys. **126**, 124314 (2007).

[145] S. K. Tokunaga, J. M. Dyne, E. A. Hinds and M. R. Tarbutt, *Stark deceleration of lithium hydride molecules*, arXiv:0812.4188v1 (2008).

[146] C. A. Barth, W. G. Fastie, C. W. Hord, J. B. Pearce, K. K. Kelly, A. I. Steward, G. E. Thomas, G. P. Anderson and O. F. Raper, *Marine 6: Ultraviolet spectrum of Mars upper atmosphere*, Science **165**, 1004 (1969).

[147] T. C. James, *Intensity measurements of the 0,0 band of the $A^3\Pi \to X^1\Sigma^+$ Cameron system of CO*, J. Mol. Spec. **40**, 545 (1971).

[148] T. C. James, *Transition moments, Franck-Condon factors, and lifetimes of forbidden transitions. Calculation of the intensity of the Cameron system of CO*, J. Chem. Phys. **55**, 4118 (1971).

[149] C. E. Johnson and R. S. van Dyck, *Lifetime of the $a^3\Pi$ metastable state of carbon-monoxide*, J. Chem. Phys. **56**, 1506 (1972).

[150] G. M. Lawrence, *Quenching and radiation rates of $CO(a^3\Pi)$*, Chem. Phys. Lett. **9**, 575 (1971).

[151] T. G. Slanger and G. Black, *$CO(a^3\Pi)$, its production, detection, deactivation, and radiative lifetime*, J. Chem. Phys. **55**, 2164 (1971).

[152] W. L. Borst and E. C. Zipf, *Lifetimes of metastable CO and N_2 molecules*, Phys. Rev. A **3**, 979 (1971).

[153] T. Sykora and C. R. Vidal, *Lifetimes of the CO metastable $a^3\Pi(v<=3,\Omega,J)$ levels*, J. Chem. Phys. **110**, 6319 (1999).

[154] T. Sykora and C. R. Vidal, *Measurement of 10^{-1} s state-specific lifetimes in the neutral CO molecule*, J. Chem. Phys. **112**, 5320 (2000).

[155] A. Wada and H. Kanamori, *Submillimeter-wave spectroscopy of CO in the $a^3\Pi$ state*, J. Mol. Spec. **200**, 196 (2000).

[156] A. Spielfiedel, W.-U. Tchang-Brillet, F. Dayou and N. Feautrier, *Ab initio calculation of the dipole transition momoment and band oscillator strengths of the CO (A-X) transition*, Astron. Astrophys. **346**, 699 (1999).

[157] A. J. Smith, R. E. Imhof and F. H. Read, *Measured lifetimes of the two vibrational levels of the $b^3\Sigma^+$ state of CO*, J. Phys. B **6**, 1333 (1973).

[158] M. Schnell, P. Lützow, J. van Veldhoven, H. L. Bethlem, J. Küpper, B. Friedrich, M. Schleier-Smith, H. Haak and G. Meijer, *A linear AC trap for polar molecules in their ground state*, J. Phys. Chem. A **111**, 7411 (2007).

[159] H. P. Dorn, R. Neuroth and A. Hofzumahaus, *Investigation of OH absorption cross-sections of rotational transitions in the $A^2\Sigma^+, v' = 0 \leftarrow X^2\Pi, v'' = 0$ band under atmospheric conditions - implications for tropospheric long-path absorption measurements*, J. Geophys. Res. - Atmos. **100**, 7397 (1995).

[160] H. L. Bethlem and R. T. Jongma, *Koude moleculen*, Nederlands Tijdschrift voor Natuurkunde **66/9**, 278 (2000).

Hoofdstuk 8

Samenvatting

Dit proefschrift over experimenten met afgeremde en in een val gevangen koude moleculen bestaat uit meerdere delen. Na de algemene introductie in Hoofdstuk 1 volgt een uitgebreide omschrijving van de gebruikte technieken in Hoofdstuk 2. Centraal in dat hoofdstuk staan de molecuul afremmer en de elektrische val waarin die afgeremde moleculen kunnen worden geladen. Dat de door deze technieken geproduceerde langzame en opgesloten moleculen zeer geschikt zijn om fundamentele, tot nu toe onbekende, eigenschappen van moleculen te bestuderen blijkt uit de daarop volgende hoofdstukken 3, 4, 5 en 6. De in deze hoofdstukken omschreven experimenten zijn te classificeren in twee verschillende types. Ten eerste zijn er de experimenten waarbij de afremmer inderdaad "slechts" wordt gebruikt om moleculen zo langzaam te maken dat ze in een elektrische val geladen kunnen worden. Het eigenlijke experiment wordt dan in de val zelf uitgevoerd. Omdat de moleculen in de val bijna stilstaan en dus heel lang op één en dezelfde plaats blijven, kunnen langzaam verlopende processen in de moleculen worden bestudeerd. In het tweede type experimenten wordt de afremmer gebruikt om pakketjes van moleculen met allerlei verschillende snelheden te produceren. Dat je met zulke pakketjes van moleculen op een nieuwe manier naar onderlinge botsingen kan kijken, leg ik verderop in deze samenvatting nog uitgebreid uit. In deze samenvatting wil ik echter de opbouw van het proefschrift volgen en eerst de gebruikte technieken bespreken. Daarna volgt een korte beschrijving van de experimenten die een molecuulval mogelijk zijn en tot slot, zoals beloofd, een uitgebreidere uitleg van het botsingsexperiment van Hoofdstuk 4.

8.1   De molecuulafremmer

Figuur 8.1 is een schematische weergave van het afremproces in een Stark-afremmer. Boven in de figuur is een rij hoogspanningselektroden te zien die

paarsgewijs afwisselend op een spanningsverschil van 40 kV en op aarde gezet zijn. Deze configuratie van spanningen creëert een sterk inhomogeen elektrisch veld van maximaal ongeveer 100 kV/cm. Dit elektrische veld kan een kracht uitoefenen op neutrale moleculen die de afremmer in vliegen. Deze kracht is het gevolg van de ladingsverdeling binnen neutrale moleculen. Dit effect wordt ook wel het *Stark-effect* genoemd, waarnaar de molecuulafremmer dan ook genoemd is. In de onderste helft van de figuur is de potentiële energie voor de
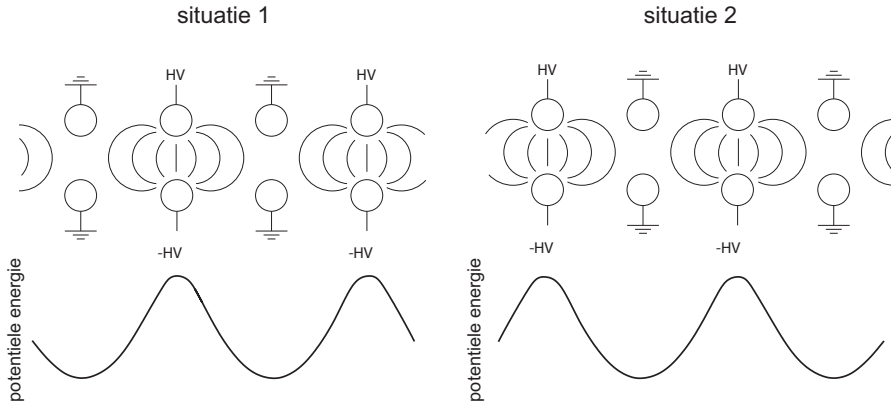
Figuur 8.1: De molecuulafremmer

moleculen weergegeven, afhankelijk van de positie op de as van de afremmer. Als de moleculen de positieve flank van deze potentiaal beklimmen, winnen ze aan potentiële energie en verliezen ze dus kinetische energie. Door op het juiste moment de elektrische velden om te schakelen (dus van situatie 1 naar situatie 2) wordt voorkomen dat de moleculen de verloren kinetische energie op de andere flank meteen weer terugwinnen. Omdat de kracht op de neutrale moleculen beperkt is en de energie die per elektrodepaar uit het molecuul genomen kan worden maar ongeveer 1 % van de totale kinetische energie bedraagt, moet dit proces herhaald worden om een significant effect te bereiken. De afremmer bestaat daarom uit 108 elektrodeparen. Hoe ver een molecuul elke keer de potentiaal opklimt, oftewel op welke tijden de elektrische velden precies geschakeld worden, bepaalt de precieze eindsnelheid van dat molecuul.

8.2 Moleculen in een val

Als de mogelijkheden van de molecuul afremmer maximaal benut worden is het mogelijk pakketjes moleculen met een snelheid van 450 m/s (1600 km/uur) binnen 10 milliseconden tot een paar meter per seconde of zelfs tot stilstand af te remmen. Dat het mogelijk is zulke langzame pakketjes molekulen in een

elektrostatische val te laden is al aangetoond en uitgebreid beschreven door mijn voorgangers Rick Bethlem en Bas van de Meerakker [160, 78]. Dat dat laden van de val met verliezen gepaard gaat en dat lang niet alle moleculen die langzaam uit de afremmer komen ook daadwerkelijk gevangen worden realiseerden ook zij zich al. In Hoofdstuk 7 van dit proefschrift is in detail beschreven wat voor problemen er kunnen optreden tijdens het laden van moleculen in een val in het algemeen. Een van die problemen is dat, als gevolg van de snelheidsspreiding en de relatief lage absolute snelheid, het pakket moleculen tijdens het overbruggen van de afstand van de afremmer tot de val enorm uitspreidt in alle richtingen. Op het moment dat de moleculen dan in de val zijn aangekomen en de val aangezet kan worden is het pakket al zo groot dat een belangrijk deel van de moleculen zich buiten het bereik van de val bevindt en daardoor niet ingevangen kan worden. In Hoofdstuk 7 is een nieuw type val besproken waarin het laatste electrodepaar van de afremmer en de val geïntegreerd zijn in één enkele set electroden. Het bovengenoemde probleem is door het ontwerp van deze val opgelost en we konden dan ook experimenteel aantonen dat de verliezen tijdens het laadproces kleiner zijn en ruim twee keer zo veel moleculen invangen. Uit berekeningen blijkt echter dat zelfs in dit ontwerp er nog steeds geen optimale overlap tussen het stilgezette pakket en de acceptantie van de val bereikt wordt. Hoofdprobleem bleek te zijn dat de laadvelden niet symmetrisch zijn en grote verschillen optreden in de snelheidscomponenten voor verschillende richtingen. Van deze oorzaken, die ook uitgebreid beschreven zijn in Hoofdstuk 7, is veel te leren voor de toekomstige generaties molecuulvallen. Tot slot wordt in dat hoofdstuk ook nog de mogelijkheid een magnetische val in plaats van een elektrische val te gebruiken besproken. Experimenten met zo'n magneetval worden op het moment van de afronding van dit proefschrift uitgevoerd in het laboratorium.

8.3 Experimenten in de molecuulval

In dit proefschrift is beschreven hoe de hierboven genoemde methode voor het invangen van neutrale moleculen voor het eerst is toegepast op OD moleculen en op metastabiele NH en CO moleculen. Het invangen van deze moleculen maakte het mogelijk verschillende nieuwe experimenten uit te voeren. Door de vergelijking van de tijd dat OD en OH moleculen in de val opgesloten blijven bijvoorbeeld, kunnen verliesprocessen die een rol spelen in de val nadat moleculen ingevangen zijn in kaart gebracht worden. In Hoofdstuk 5 is beschreven hoe precies de verhouding is tussen het verlies ten gevolge van botsingen met deeltjes uit de (vacuüm) omgeving en het verlies ten gevolge van warmtestraling. Op de metingen aan de verliesprocessen van OH en OD zijn vervolgens berekeningen gebaseerd die ook uitspraken doen over verliesprocessen in experimenten met andere moleculen. Kennis over die verliesprocessen is niet alleen relevant om toekomstige molecuulvallen te kunnen ontwerpen waar de molecu-

len langer opgesloten blijven, maar ook voor andere experimenten waarbij de tijd dat moleculen in de val blijven een rol speelt. Een dergelijk experiment is beschreven in Hoofdstuk 6. Doel van dat experiment is het bepalen van de levensduur van de elektronisch aangeslagen metastabiele toestand van CO, één van de parameters die gebruikt wordt om quantum mechanische theoretische modellen te testen. Omdat die levensduur relatief lang is (enkele milliseconden), is het lastig met klassieke methoden uit de gasfase spectroscopie een precieze meting te doen. Door metastabiel CO af te remmen en in een val op te sluiten met onze apparatuur kon een lange observatietijd bereikt worden. Hoe lang die observatietijd precies was en in welke mate verliesprocessen de meting van de levensduur beïnvloedden was bekend uit de berekeningen van Hoofdstuk 5. Door de combinatie van die kennis over verliesprocessen en de lange observatietijd was de bepaling van de levensduur tot op een procent nauwkeurig.

## 8.4 Moleculaire botsingen in *slow motion**

Naast het invangen van moleculen en de experimenten die met zulke opgesloten pakketjes moleculen mogelijk zijn, gaat dit proefschrift over experimenten die mogelijk zijn geworden dankzij de ontwikkeling van de Stark-afremmer. Zoals eerder genoemd, is een botsingsexperiment één van die mogelijkheden. Het gedrag van botsende moleculen laat zich over het algemeen lastig bestuderen. De Stark afremmer is een nieuw gereedschap om botsingen tussen neutrale moleculen en atomen bij lage snelheden te onderzoeken. Het voordeel dat de Stark-afremmer daarbij biedt is dat de snelheid tussen ongeladen moleculen over een groot bereik kan worden gevarieerd, terwijl bij een gekozen snelheid de spreiding extreem klein is.

Botsingen

Een botsingsexperiment, waarbij onder gecontroleerde omstandigheden twee deeltjes op elkaar geschoten worden, is één van de meest fundamentele manieren om iets over atomen, moleculen en hun interactie te leren. De energie die beschikbaar is bij zo'n botsing is een bepalende factor voor wat er gebeurt. In grote versnellers voor geladen deeltjes, zoals de nieuwe Large Hadron Collider (LHC) van CERN in Genève, is zoveel energie beschikbaar dat de botsende deeltjes uit elkaar kunnen vallen tot elementaire deeltjes. Door een geraffineerde analyse van de botsingsproducten valt op deze manier veel te leren over de interne structuur van geladen deeltjes en hun onderlinge interacties.

Het is ook mogelijk de structuur van neutrale deeltjes te onderzoeken door middel van botsingsexperimenten. Het is echter experimenteel veel lastiger om de snelheid van ongeladen deeltjes te variëren. Voor neutrale moleculen geldt bovendien dat juist botsingen bij geringe energie veel informatie opleveren. Moleculen vallen dan niet uiteen maar naderen elkaar uiterst behoedzaam. De veranderingen die dan in het molecuul plaatsvinden, zijn een uitgelezen test voor de theorie die de kwantumstructuur van en de interactie tussen moleculen beschrijft. Het is belangrijk om in zo'n experiment de botsing onder goed gecontroleerde omstandigheden te laten plaatsvinden. Om de onderlinge energie te variëren zijn in het verleden vindingrijke experimenten opgebouwd waarbij twee pakketjes moleculen elkaar onder een te variëren hoek treffen [121]. Deze hoek bepaalt dan de relatieve snelheid tussen de botsingspartners en dus de botsingsenergie. Deze methode heeft echter het probleem dat bij heel lage energie, als de hoek tussen beide gekruiste pakketjes erg klein is, de energieresolutie niet voldoet om alle details in de energieafhankelijkheid op te lossen.
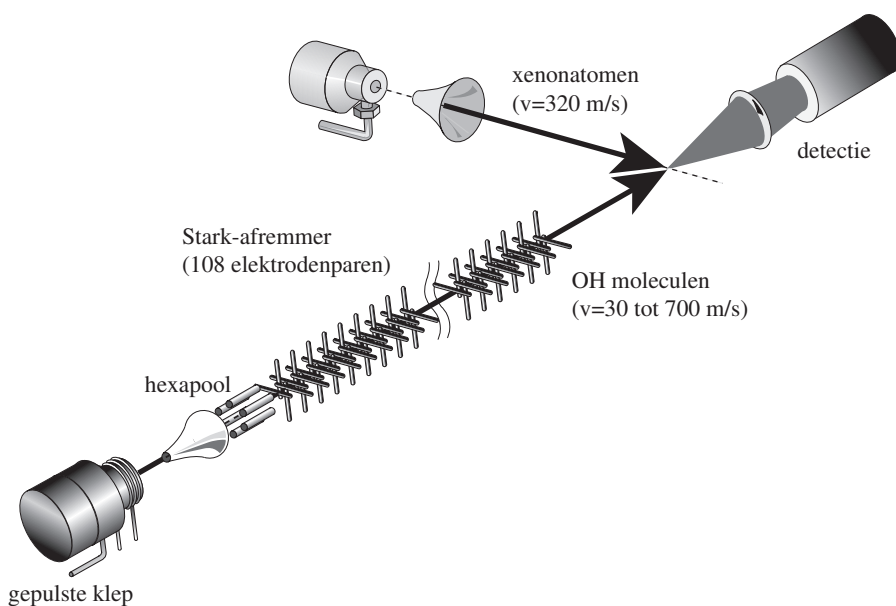
Figuur 8.2: De experimentele opstelling voor het botsingsexperiment. Twee bundels kruisen elkaar onder een hoek van negentig graden. De botsingsenergie kan gevarieerd worden door de snelheid van een van de botsingspartners te variëren.

De Stark-afremmer

In het hier beschreven onderzoek zijn we erin geslaagd de energie van polaire neutrale moleculen te variëren door, met behulp van de Stark-afremmer, de snelheid van één van de botsingspartners te controleren. Deze methode biedt het voordeel van een hogere energieresolutie, die bovendien behouden blijft wanneer het bereik van lage energie wordt opgezocht. Zoals hierboven beschreven kunnen met de afremmer pakketjes moleculen met grote nauwkeurigheid tot een gewenste snelheid afgeremd of versneld worden. In het hier gepresenteerde botsingsexperiment werd de snelheid van pakketjes moleculen gevarieerd tussen 700 en 33 meter per seconde. De snelheidsspreiding in zo'n pakket moleculen is erg klein, van de orde van enkele meter per seconde. Dankzij deze kleine snelheidsspreiding is de energieresolutie veel hoger dan in andere, eerder ook al genoemde, botsingsexperimenten met molekuulbundels. Naast de hoge snelheidsresolutie heeft het afremproces nog het voordeel dat het toestandselectief is. Terwijl aan de ingang van de afremmer de moleculen nog verdeeld zijn over meerdere kwantumtoestanden, is, door verschillen in het Stark-effect, aan het eind de puurheid van de bundel zo goed als 100 procent. Deze goed gedefinieerde beginvoorwaarden vormen een ideale start voor een botsingsexperiment.

Om de nieuwe methode te demonstreren, hebben we inelastische botsingen tussen neutrale OH-radicalen en xenonatomen onderzocht. In figuur 8.2 is te zien hoe de twee bundels in het experiment elkaar kruisen. De pijl geeft de richting van de OH-moleculen aan. Het OH wordt in pakketjes gevormd via fotodissociatie van salpeterzuur (HNO$_3$), en vliegt dan via een focusserende hexapool de afremmer in. Daar wordt het pakket vervolgens op de gewenste snelheid gebracht. De botsingspartner, in dit geval een pakket van xenonatomen met grote dichtheid, nadert het OH-pakket onder een hoek van negentig graden. De tijden waarop de beide gepulste kleppen in het experiment geopend worden zijn zo op elkaar afgestemd, dat de pakketjes elkaar precies treffen in het detectiesysteem. De moleculen worden geëxciteerd met gepulst laserlicht met een golflengte van 282 nanometer, zodat ze kunnen worden gedetecteerd door het licht dat ze vervolgens uitzenden te meten met een fotoversterkerbuis.


Het OH-xenon-systeem

Het OH-radicaal is een veelbestudeerd molecuul, mede omdat het een grote rol speelt in veel chemische reacties, bijvoorbeeld in de aardse atmosfeer. Ook experimenten aan botsingen van het OH-radicaal met een edelgas zijn niet nieuw. In een artikel uit 2000 [134] is bijvoorbeeld te lezen welk effect de oriëntatie van de moleculen heeft op de botsingsdoorsnede. Omdat het OH-molecuul uit slechts twee atomen bestaat, zijn de (gekwantiseerde) interne rotaties en trillingen goed bekend en relatief eenvoudig te beschrijven. Voor meer detail zie figuur 8.3.
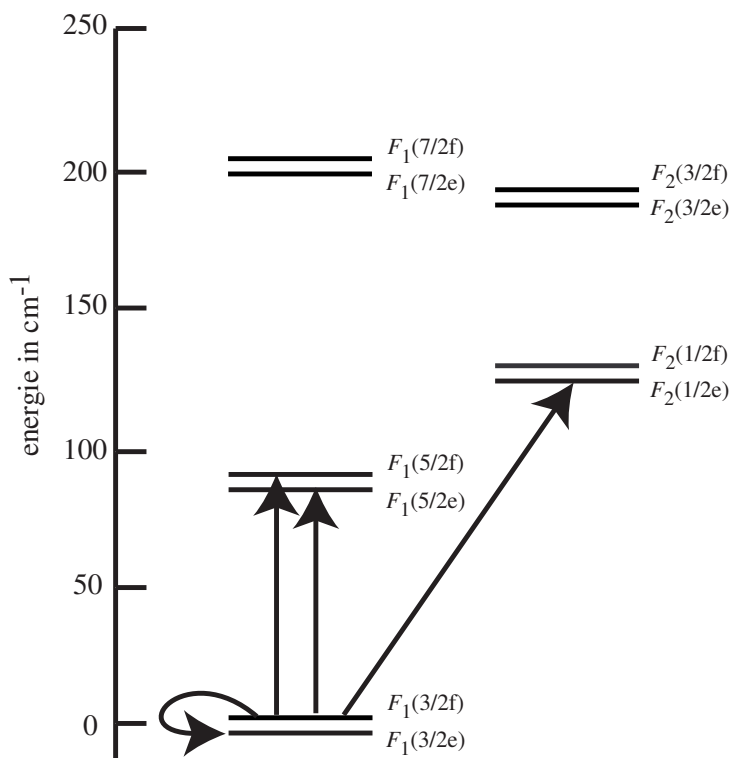
Figuur 8.3: In dit energieschema zijn de laagste rotatietoestanden van het OH-molecuul weergegeven in twee ladders. Het verschil tussen de twee ladders zit in de koppeling tussen spin en baan van het elektron. In de linker ladder zijn de richting van de spin en de baan parallel, rechts antiparallel. Dit wordt respectievelijk gelabeld als F_1 en F_2. Elke rotatietoestand $(1/2, 3/2, 5/2,$ enzovoort) is opgesplitst in twee toestanden e en f met tegengestelde pariteit, deze splitsing wordt de Lambda-splitsing genoemd. Vergeleken met het energieverschil tussen de verschillende rotatietoestanden is deze splitsing klein en daarom in de figuur ter verduidelijking sterk uitvergroot. De vier pijlen die verschillende kwantumniveaus verbinden geven aan welke door botsingen geïnduceerde overgangen onderzocht zijn in ons experiment.

Startpunt van het botsingsexperiment is een pakket OH-moleculen in de $F_1(3/2f)$-toestand (met een dikke zwarte lijn weergegeven in het energieschema). Eén op de tien moleculen botst met een xenonatoom, en ongeveer één op de tien van deze botsingen is inelastisch en kan leiden tot een overgang van een of meer rotatiekwanta en/of het omdraaien van de pariteit in het OH-molecuul.

De precieze verdeling van het OH over de verschillende toestanden vóór en na de botsing werd in het experiment gemeten met behulp van een gepulste laser, die de moleculen toestandsselectief kan exciteren. Dat is een lastige meting omdat na de botsing per kwantumtoestand maar minder dan één procent van het oorspronkelijke pakket terug te vinden is.
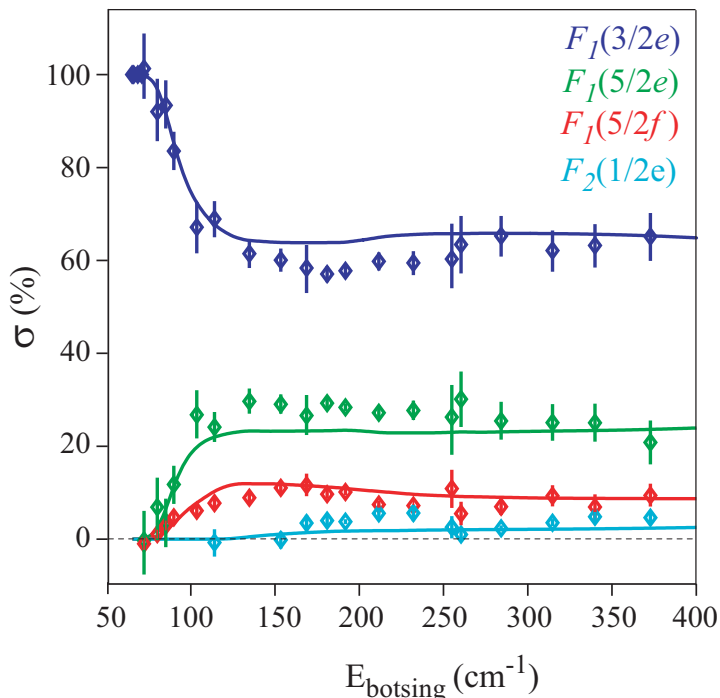
Figuur 8.4: De gemeten energieafhankelijkheid van de relatieve botsingsdoorsnede. De doorgetrokken lijnen geven het theoretisch voorspelde gedrag weer.

Welke overgangen mogelijk zijn en met welke waarschijnlijkheid, hangt af van de beschikbare hoeveelheid energie. In figuur 8.4 zijn de resultaten van onze metingen voor vier bestudeerde overgangen samengevat. In de rechterzijde van de figuur is te zien dat botsingen die een overgang induceren naar de $F_1(3/2e)$-toestand (blauw) het meest waarschijnlijk zijn. Voor overgangen naar de toestanden $F_1(5/2e)$ en $F_1(5/2f)$ geldt dat de waarschijnlijkheid sterk afneemt als de beschikbare energie lager is dan de energetische drempelwaarden zoals weergegeven in figuur 8.3. Het enige elastische exo-energetische kanaal is de overgang naar de $F_1(3/2e)$-toestand. Ook de veel minder waarschijnlijke overgang naar de $F_2(1/2e)$-toestand, waarbij de koppeling tussen de spin en de baan van het elektron verandert, vertoont een duidelijk drempelgedrag.

De veranderingen in de waarschijnlijkheden voor de verschillende overgangen rond deze drempelwaarden gelden als een belangrijke test voor de theorie van de interactie tussen moleculen. Bij de behaalde energieresolutie is het experiment ook gevoelig voor slechts kleine afwijkingen van de theorie. De doorgetrokken lijnen in figuur 8.4 geven de theoretische voorspellingen weer, zoals Gerrit Groenenboom van de Radboud Universiteit Nijmegen die onafhankelijk van het experiment berekende.

Vooruitblik

Er is een scala aan experimenten denkbaar dat met deze nieuwe techniek mogelijk geworden is. Dankzij de kleine snelheidsspreiding van de door een Stark-afremmer afgeremde OH-pakketjes, kan een hoge energieresolutie behaald worden. De snelheidsspreiding van het niet-afgeremde xenon pakketje beperkte echter die resolutie in het beschreven experiment. Een mogelijke uitbreiding is dan ook een botsingsexperiment waarbij de snelheid van beide partners wordt gevarieerd. Hiervoor is het nodig twee afremmers voor neutrale deeltjes te bouwen, waarbij de beide bundels elkaar kruisen. Daardoor zou de nauwkeurigheid waarmee de botsingsenergie gevarieerd kan worden met nog eens een ordegrootte verbeteren, waardoor nog meer details van de interactie tussen moleculen, zoals voorspelde resonanties in botsingsdoorsnede [16] aan het licht kunnen komen.

Een andere belangrijke toepassing voor de molekuulafremmer vinden we in de chemie. Ook voor chemische reacties geldt namelijk dat als maar weinig energie beschikbaar is voor de reactie ze helemaal niet verlopen of dat kwantummechanische effecten het gedrag van de reactie gaan domineren. Om reacties bij dit soort omstandigheden te onderzoeken kan de afremmer een ideaal middel zijn.

Dankwoord

To celebrate the 100th anniversary of three of Einstein's great theories, 2005 was declared to be the *Einstein year* by the German Physical Society (DPG). In February of that year, I moved from Amsterdam to Berlin and started my research work at the Fritz-Haber-Institut. I remember all of Berlin was full of snow and scattered with big billboards with famous Einstein quotes, like "I am convinced that He (God) does not play dice." While in Berlin, Albert Einstein worked at the Kaiser-Wilhelm-Institut, the predecessor of the Fritz-Haber-Institut. He developed his important theories mostly alone. Luckily, I did not have to do my research alone. During my stay at the Fritz-Haber-Institut, I have always been surrounded and supported by motivated and helpful colleagues.

The words "motivating" and "helpful" most certainly apply to my promotor Gerard Meijer. Gerard gave me the opportunity to work in his luxury Molecular Physics laboratory of the Fritz-Haber-Institut, where ample research funding and Gerard's inexhaustible motivation and energy are the Keys to successful scientific research. Gerard, I thank you for taking excellent care of this research environment and for your personal style of supervision. The latter was proved once again when you helped me find my new job at the Dutch embassy!

My copromotor Bas van de Meerakker also never lacks the motivation for science and even likes to compare working as a scientist to competing in professional sports. Bas! If I am the sportsman in your comparison, you have been the devoted coach. In your role as a technical coach, you taught me a lot about the Stark effect and how to plan a difficult laboratory experiment. You also coached me in making the framework for good scientific papers and for this thesis. This thesis has literally become also your thesis, because you even helped me write large parts of it when I got pressed for time towards the end. As a mental coach, you had the difficult task to keep me constantly motivated. Moreover, you tried to advise me (usually unasked for) on almost every aspect of living in Berlin. I am glad I occasionally listened to your advice. Bas, thanks for being such an excellent coach!

The successes that I accomplished in the laboratory I owe in large part to

the people that I worked with on a daily basis. Steven, your drive, enthusiasm, impatience and competence have always helped us go in fast forward. We alternated exciting new experiments in our decelerator and traps with nice papers. To celebrate every new step, we treated our colleagues to many kilo's of cake and to even more liters of beer on the sunny Molecular Physics roof terrace. Apart from our successes, it has also been a pleasure to work with you as a team on our *Big Machine*. In the last months, you have formed a new team to work on trapped molecules. I wish you, Jens and Fabian good luck in all future experiments!

In addition to Bas and Steven, with whom I worked for almost my full 4 years at the Fritz-Haber-Institut, there have been several other people with whom I worked in the laboratory for shorter or longer periods of time. At the beginning of my time on the experiment there was Nicolas, who helped me to get to know the machine and all its secrets and trigger schemes. At that time we were still steering the decelerator by an old, home made computer program. Nico was the one who taught me how to stop a scan, "just press CTRL + BREAK, ENTER, F9, CTRL + F, ENTER (mouse-click stopscan), ENTER, 1, ENTER, Return! (mouse-click), F4." I was happy that not long after that, we got a new program from Jochen and Uwe, in which a scan can be stopped by just two mouse-clicks and that is even capable of optimizing the experiment by itself! Many thanks also to Markus, who worked in our team for one full year. In that year, he not only tried to break my legs many times on the football field, but also taught me the secrets of ontelovaimenemisspektroskopian. And believe me, even in Finland not many people have a clue what this means. I refer interested readers to chapter 2 of this thesis. Sam, thanks for working with me on the ontelovaimenemisspektroskopian and the CO lifetime experiment, for your laser and your indestructible camera, and for your great sense of humor. Three of the seven chapters in this thesis are partly based on theoretical work of Gerrit Groenenboom (Nijmegen) and Boris Sartakov (Moscow). I thank both of them for their valuable contribution and their patience in explaining it. For the indispensable technical support in the laboratory I thank Jürgen, Uwe, Manfred, Sandy, Rolf, Georg, and the people from Feinwerktechnik, PP&B, GNZ, and the E-Labor. Also, thanks to Henrik for his help with all design issues.

Apart from an excellent research laboratory, the MP department has been a pleasant environment where I really felt at home. Working there was not only "highly motivating and effective", but quite often also relaxing and just fun. For that, I thank Inga, Ludwig, all Peters, Moritz, Fabian, Sophie, Michael, Joost, Bea, Jacqueline, Stephan, Cyndi, Frank, Uwe, Jochen, Wolfgang, Horst, Irena, Rick, Jens, Bretislav, Gert, André, Jonathan, Werner, Dagmar, Philipp, Katrin, Amudha, Kirstin, Undine, Max, Simon, Evelyn, Knut, Markus, Thalia, Carsten, Christa, Risshu, Daniel, Andreas, Adela, Melanie, Frauke, Hugo,

Karsten, Marko, Koos, Mikhail, Marcin, Alexander, Bum Suk, Wieland, Christian, Torsten, Dave, Phil, and all others that spent time in the department. I have become friends with many of you and I will miss working with all of you.

I thank the manuscript committee Hans ter Meulen, Peter Barker, and Nicolas Vanhaecke for carefully reading my manuscript and for their useful comments. Thanks also to Adela and Steven for proof reading parts of my manuscript, and to Cyndi for her help with the hassle of layout, print shop and templates.

Finally I thank all my friends in Berlin, Amsterdam, and all over the world for their support and distractions. Mijn familie. Und Diana.

Joop Gilijamse,

Berlin, April 2009

Curriculum Vitae

Joop J. Gilijamse
Born April 16, 1980 in Amsterdam, The Netherlands

1998	High School Diploma, Barlaeus Gymanasium, Amsterdam.
1998 - 2004	Physics studies, University of Amsterdam.
2002 - 2003	Master's project "Hydrogen-Bond Dynamics of Water in Molecular Confinement" in the researchgroup of prof. Huib J. Bakker at the FOM instituut voor Atoom- en Molekuul- Fysica (AMOLF) in Amsterdam.
2004 - 2005	Junior researcher in the researchgroup of prof. Huib J. Bakker at the FOM instituut voor Atoom- en Molekuul- Fysica (AMOLF) in Amsterdam.
2005 - 2009	PhD student in the group of Prof. dr. Gerard J. M. Meijer. Experiments conducted at the Fritz-Haber-Institut der Max-Planck-Gesellschaft, Berlin, Germany.
2009 - present	Officer for Science and Technology at the dutch embassy, Berlin, Germany.

List of publications

Optimizing the Stark-decelerator beamline for the trapping of cold molecules using evolutionary strategies
Joop J. Gilijamse, Jochen Küpper, Steven Hoekstra, Nicolas Vanhaecke, Sebastiaan Y. T. van de Meerakker, Gerard Meijer
Physical Review A **73**, 063410 (2006).

Near-threshold inelastic collisions using molecular beams with a tunable velocity
Joop J. Gilijamse, Steven Hoekstra, Sebastiaan Y. T. van de Meerakker, Gerrit C. Groenenboom, and Gerard Meijer
Science **113**, 1617 (2006).

Optical pumping of trapped neutral molecules by blackbody radiation
Steven Hoekstra, Joop J. Gilijamse, Boris Sartakov, Nicolas Vanhaecke, Ludwig Scharfenberg, Sebastiaan Y. T. van de Meerakker, and Gerard Meijer
Physical Review Letters **98**, 133001 (2007).

The radiative lifetime of metastable CO ($a^3\Pi, v = 0$)
Joop J. Gilijamse, Steven Hoekstra, Samuel A. Meek, Markus Metsälä, Sebastiaan Y. T. van de Meerakker, Gerard Meijer, and Gerrit C. Groenenboom
Journal of Chemical Physics **127**, 221102 (2007).

Electrostatic trapping of NH radicals
Steven Hoekstra, Markus Metsälä, Peter C. Zieger, Ludwig Scharfenberg, Joop J. Gilijamse, Gerard Meijer and Sebastiaan Y.T. van de Meerakker
Physical Review A **76**, 063408 (2007).

Reflection of OH molecules from magnetic mirrors
Markus Metsälä, Joop J. Gilijamse, Steven Hoekstra, Sebastiaan Y. T. van de Meerakker, and Gerard Meijer
New Journal of Physics **10**, 053018 (2008).